



**UNIVERSITÀ
DEGLI STUDI
DI TRIESTE**

UNIVERSITY OF TRIESTE

PHYSICS DEPARTMENT

Master's Degree in Nuclear and Subnuclear Physics

**Study of the $B^0 \rightarrow D^{*-} l^+ \nu_l$ decay at Belle II for a
new measurement of the decay dynamics and $|V_{cb}|$**

Student:

Matteo Filipig

Supervisor:

Dr. Mirco Dorigo

Co-supervisor:

Michele Mantovano

ACADEMIC YEAR 2023–2024



**UNIVERSITÀ
DEGLI STUDI
DI TRIESTE**

UNIVERSITÀ DI TRIESTE

DIPARTIMENTO DI FISICA

Laurea Magistrale in Fisica Nucleare e Subnucleare

**Studio del decadimento $B^0 \rightarrow D^{*-} l^+ \nu_l$ a Belle II per
una nuova misura della dinamica di decadimento e
di $|V_{cb}|$**

Studente:

Matteo Filipig

Relatore:

Dr. Mirco Dorigo

Correlatore:

Michele Mantovano

ANNO ACCADEMICO 2023–2024

Abstract

This is an experimental particle physics thesis that aims to study the exclusive semileptonic decay $B^0 \rightarrow D^{*-}l^+\nu_l$ at Belle II for a new measurement of its decay dynamics and $|V_{cb}|$. Belle II is a particle physics experiment that focuses on weak-interaction processes of heavy quarks to search for indirect indications of non-standard-model physics. The $B^0 \rightarrow D^{*-}l^+\nu_l$ decay provides access to the strength of the *bottom-to-charm* weak coupling, $|V_{cb}|$, a fundamental parameter of the standard model, whose determination presents a long-standing discrepancy between two measurement methods, the so-called *inclusive* and *exclusive* approaches. The $B^0 \rightarrow D^{*-}l^+\nu_l$ decay is the golden mode of the exclusive approach. In this approach, to determine $|V_{cb}|$ from experimental data, a parameterization of the strong-interaction contribution to the decay amplitude is needed. Recent calculations of this contribution in the $B^0 \rightarrow D^{*-}l^+\nu_l$ decay showed some inconsistencies, making the exclusive determination less precise.

This work aims to explore a novel experimental approach which provides a measurement of model-independent observables of the decay dynamics, which can be interpreted assuming any theoretical model to parameterize the strong interaction contribution. The analysis is conducted using a full, realistic simulation of the Belle II sample collected between 2019 and 2022. A selection is developed to obtain a high-purity signal sample, whose composition is studied in detail to model the data for a multi-dimensional χ^2 fit that measures the model-independent observables. The fit is inspected in search for configurations which minimize fit parameter biases. A comparison between two configurations of fit variables is performed to assess which one returns the best parameter sensitivity, and the model-independent observables obtained are interpreted with a theoretical model to obtain $|V_{cb}|$. The results show that in the fit performed, for the best sensitivity on $|V_{cb}|$, a better signal-to-background discrimination is preferred over adding more information about the decay dynamics.

Sommario

Questa è una tesi sperimentale di fisica delle particelle che ha lo scopo di studiare il decadimento semileptonico $B^0 \rightarrow D^{*-}l^+\nu_l$ a Belle II per una nuova misura della dinamica del decadimento e di $|V_{cb}|$. Belle II è un esperimento di fisica delle particelle che si concentra sui processi di interazione debole dei quark pesanti per cercare indirettamente delle prove di fisica oltre il modello standard. Il decadimento $B^0 \rightarrow D^{*-}l^+\nu_l$ permette di misurare $|V_{cb}|$, l'intensità dell'accoppiamento debole tra quark *bottom* e *charm*. Questo è un parametro fondamentale del modello standard la cui determinazione presenta da molti anni una discrepanza tra due metodi di misura, detti inclusivo ed esclusivo. Il decadimento $B^0 \rightarrow D^{*-}l^+\nu_l$ è il canale principale usato nel metodo esclusivo. Per ottenere $|V_{cb}|$ dai dati sperimentali, questo metodo richiede una parametrizzazione del contributo dell'interazione forte nell'ampiezza di decadimento. Calcoli recenti di questo contributo per il decadimento $B^0 \rightarrow D^{*-}l^+\nu_l$ presentano discrepanze tra loro, che rendono la misura di $|V_{cb}|$ meno precisa.

Questo lavoro mira ad esplorare un nuovo approccio sperimentale per misurare delle osservabili legate alla dinamica del decadimento, che possono essere interpretate assumendo qualsiasi modello teorico per il contributo dell'interazione forte nella determinazione di $|V_{cb}|$. L'analisi è condotta utilizzando una simulazione realistica dei dati acquisiti da Belle II dal 2019 al 2022. Ho sviluppato una selezione per ottenere un campione di alta purezza, studiandone la composizione in dettaglio per sviluppare un fit di χ^2 multidimensionale a più componenti e misurare le osservabili di interesse. Ho controllato diverse configurazioni di fit e i *bias* nella determinazione dei parametri. Ho effettuato un confronto tra due configurazioni di variabili di fit per valutare quale di esse fornisce la precisione migliore nella misura. Ho scelto un modello teorico come esempio con cui interpretare la misura per ottenere $|V_{cb}|$. I risultati dimostrano che avere una migliore discriminazione tra segnale e fondo garantisce risultati più precisi su $|V_{cb}|$ rispetto ad aggiungere nel fit nuova informazione sulla dinamica di decadimento.

Contents

Introduction	1
1 Theoretical framework	3
1.1 The standard model of particle physics	3
1.2 The quark-flavor sector	6
1.2.1 Current picture	9
1.3 Extending the standard model	10
1.4 The CKM element V_{cb}	12
2 The $B \rightarrow D^* \ell \nu$ decay	15
2.1 Semileptonic B decays: generalities	15
2.2 Exclusive B meson decay $B \rightarrow D^* \ell \nu_\ell$	17
2.3 Experimental status	19
2.4 A novel approach	23
2.4.1 Goal and plan of the thesis	25
3 The Belle II experiment	27
3.1 The SuperKEKB collider	27
3.2 The Belle II detector	29
3.3 Tracking detectors	30
3.3.1 Silicon-pixel vertexing detector	32
3.3.2 Silicon-microstrip vertexing detector	33
3.3.3 Central drift chamber	34

3.4	Particle-identification detectors	35
3.4.1	Time of propagation counter	35
3.4.2	Aerogel ring-imaging Cherenkov	36
3.4.3	K_L^0 and muon detection system	37
3.4.4	Electromagnetic calorimeter	37
3.4.5	Online event selection	39
3.5	Current status of Belle II operations	40
3.6	The Belle II software and simulation	42
4	Data sample and event selections	43
4.1	Data samples	43
4.1.1	Sample components	45
4.2	Event selection	46
4.2.1	Skim selection	47
4.2.2	Final requirements	49
4.2.3	Final sample composition	56
4.3	Monte Carlo validation	58
5	Fit of sample composition	61
5.1	Accessing the differential decay rate	61
5.2	Fit of sample composition	63
5.3	Assessing best fit configurations	65
5.3.1	Tested configurations	66
6	Measurement of the model-independent observables	71
6.1	Fit of the model-independent observables	71
6.1.1	Signal reweighting	72
6.1.2	Pseudo-experiment results	75
6.2	Sensitivity to $ V_{cb} $ and form factor parameters	78
6.2.1	Results	80
6.3	Final considerations	81
	Summary	83

Bibliography	85
A Form Factor parameterizations	95
B Data-simulation comparison	99
C Fit of sample composition: pull distributions	105
D Model-independent fit: pull distributions	107
E <i>A-posteriori</i> fit: pull distributions	111

Introduction

The standard model (SM) of particle physics is currently the accepted theory that describes elementary particles and three out of the four fundamental interactions. The SM predicts with extraordinary precision many experimental results in processes mediated by the electromagnetic, weak, and strong interactions across several orders of magnitudes in energy. However, a number of open questions and experimental observations suggest that the SM might be an effective theory, only valid at the energy we can currently probe, that is part of a more general unknown theory. Finding an extension to the SM is the main goal of modern particle physics.

There are two approaches adopted to search for SM extensions. The *direct* approach consists in searching for decay products of non-SM particles produced on-shell in high-energy collisions. This approach would provide clear evidence of new particles, but it is limited by the available collision energy of today's colliders. Another complementary method is the *indirect* approach, that aims to perform precise measurements in lower-energy processes in which off-shell non-SM particles could take part, and to search for deviations of experimental results from SM predictions. This is not limited by energy but experimental evidence of new phenomena is typically harder to establish: it requires great experimental and theoretical precisions and a coherent, clear pattern of discrepancies in several processes.

The Belle II experiment is one of the main ongoing experiments that tests indirectly the SM using data produced by SuperKEKB, the asymmetric positron-electron collider located in Tsukuba, Japan. Belle II has been designed to make precise measurements in weak interactions of *bottom* and *charm* quarks, as well as *tau* leptons. Belle II started collecting data in January 2019 and ended in June 2022, recording a sample of 424 fb^{-1} of integrated luminosity. This is the so-called Run I sample. Run II started in March 2024, after a 1.5 years shutdown to upgrade part of the

detector, and will go on until a second shutdown for a new upgrade, expected in 2027, with the goal of collecting a sample about 6-7 times larger than that of Run I.

The work presented in this thesis aims to study with Belle II data a semileptonic decay of the B^0 meson, the $B^0 \rightarrow D^{*-} \ell^+ \nu_\ell$ decay (ℓ indicates a muon or an electron). This decay is particularly suited to measure the strength of the Cabbibo-Kobayashi-Maskawa (CKM) matrix element, $|V_{cb}|$, which describes the intensity of the weak coupling between *bottom* and *charm* quarks. Precise measurements of $|V_{cb}|$ are key for testing the quark-flavour sector of the SM. These are obtained through semileptonic B meson decays using two different methods: *inclusive* measurements sum all possible final *charm* states which the B can decay into; *exclusive* methods focus on specific decay channels. Currently, there is a discrepancy of about 6% between the results of $|V_{cb}|$ from the two methods; this limits the knowledge of this important parameter of the SM.

The $B^0 \rightarrow D^{*-} \ell^+ \nu_\ell$ decay presented in this work is the golden mode of the exclusive method, which relies, to obtain $|V_{cb}|$, on a parameterization of the decay dynamics with effective functions, called *form factors* (FFs), which describe strong interactions between quarks bounded in mesons. Experimental results must be complemented by a precise calculation of the FFs to extract $|V_{cb}|$. Recent, more precise calculations of the FFs of the $B^0 \rightarrow D^{*-} \ell^+ \nu_\ell$ decay from different theoretical groups showed significant discrepancies, making the extraction of $|V_{cb}|$ from this channel less solid. My thesis aims to explore a novel experimental approach to provide a measurement of model-independent observables of the decay dynamics. These observables can be interpreted assuming any possible FF model: this eases a phenomenological analysis to determine $|V_{cb}|$ from experimental data with any possible theoretical advancement on the FF modelling.

The thesis is structured as follows. Chapter 1 introduces the SM, focusing on the quark-flavour sector. Chapter 2 describes the phenomenological features of semileptonic B decays, the current status of measurements and the novel approach employed in this thesis. Chapter 3 gives an overview of the Belle II detector, while Chapter 4 details the selection of the data and the sample composition. In Chapter 5 I report the experimental method to access the decay dynamics and the fit of the sample composition, with studies on simulated data. This fit is expanded to include the model-independent observables in Chapter 6 and tested with simulation, where I also show an interpretation of the results and compare the sensitivity to $|V_{cb}|$ in two different fit configurations. A brief summary concludes the thesis.

Chapter 1

Theoretical framework

In this Chapter, I give a brief overview of the standard model of particle physics. I focus on the quark-flavour sector, introducing how its experimental study can provide indirect evidence of physics beyond the standard model or powerful constraints to exclude possible new models. I conclude by discussing V_{cb} , the bottom-to-charm quark coupling, giving motivations for the precise measurement of its strength.

1.1 The standard model of particle physics

The standard model (SM) of particle physics is a quantum field theory that describes elementary particles and three of the four fundamental forces existing in the Universe. Electromagnetic, strong and weak processes are described with great precision, while gravity is still not included, due to conceptual difficulties that prevent achieving a description of gravity consistent with quantum mechanics [1–6]. The model is based on the symmetry group:

$$SU(3)_C \otimes SU(2)_L \otimes U(1)_Y, \quad (1.1)$$

where $SU(3)_C$ is the standard unitary group of strong interactions (described by quantum chromodynamics, QCD), and the product of the groups $SU(2)_L \otimes U(1)_Y$ yields the electromagnetic and weak interactions (the *electroweak* force): $SU(2)_L$ is the standard unitary group of the weak

*isospin*¹ and $U(1)_Y$ is the unitary group of the *hypercharge*.

Mediators of these interactions are spin-1 particles called *gauge bosons*. The strong force is mediated by eight *gluons*, which are massless neutral gauge particles corresponding to the eight $SU(3)_C$ generators. They carry the quantum charge of *color*, which can be *red*, *blue* or *green*, and mediate interactions between quarks. Weak interactions are mediated by three massive bosons, two charged (W^\pm) and one neutral (Z^0). Lastly, the mediator of electromagnetic force is the photon γ , which is a massless gauge boson: it mediates interactions between electric charged particles. The electroweak bosons (W^\pm, Z^0, γ) arise from the following linear combinations of $SU(2)_L \otimes U(1)_Y$ generators:

$$W^\pm = \frac{1}{\sqrt{2}}(W_1 \mp iW_2), \quad \begin{pmatrix} \gamma \\ Z^0 \end{pmatrix} = \begin{pmatrix} \cos \theta_W & \sin \theta_W \\ -\sin \theta_W & \cos \theta_W \end{pmatrix} \begin{pmatrix} B \\ W_3 \end{pmatrix}. \quad (1.2)$$

where θ_W is a free parameter, called *Weinberg angle*. The masses of the W^\pm and Z^0 weak bosons are connected with each other via the θ_W parameter, which are bounded by this relation:

$$\frac{m_W^2}{\cos^2 \theta_W m_Z^2} = 1. \quad (1.3)$$

In the SM, the Higgs mechanism is responsible for the electroweak symmetry breaking into the electromagnetic group ($U(1)_{\text{em}}$). This brings the system from four generators, shown in Eq. 1.2, to a single generator, thus breaking three degrees of freedom.

Excitations of spin- $\frac{1}{2}$ field correspond to fundamental particles of matter called *fermions*. Each fermion has its associated anti-particle, with the same mass but opposite quantum numbers. Fermions are categorized into two classes, which are organized in three families of weak isospin doublets:

- Quarks are particles characterized by a fractionary electric charge. Each family is formed by an up-like particle with electric charge of $\frac{2}{3}e$ and a down-like particle with $-\frac{1}{3}e$:

$$\begin{pmatrix} u \\ d \end{pmatrix} \begin{pmatrix} c \\ s \end{pmatrix} \begin{pmatrix} t \\ b \end{pmatrix}. \quad (1.4)$$

Each quark is identified by its flavor, and also carries a color. They couple with strong and electroweak interactions. Quarks cannot be observed individually but only in colorless bound

¹The L in the standard unitarity group stands for *left*, because only particles with left chirality engage in weak interactions.

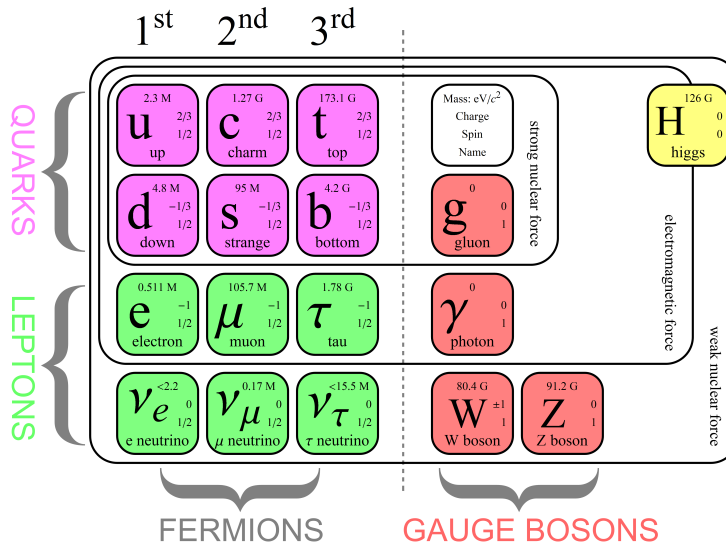


Figure 1.1: Particle contents of the standard model [7].

states called *hadrons*, and depending on the number of quarks that compose them, they are called *mesons* or *baryons*. Mesons are formed by a quark and an anti-quark while baryons are composed of three quarks or three anti-quarks. Baryons have a quantum number, called baryon number, which is conserved in interactions even if no symmetries in the Lagrangian of the SM require that.

- Lepton families are formed by a massive particle with charge $-e$ and a massless neutral particle called *neutrino*. They couple only via electroweak interactions. Similarly to baryons, each family has its own quantum number, called leptonic number, which is conserved in all interactions even if no symmetries requires that².

Figure 1.1 shows a summary scheme of the elementary particles of the SM.

Chirality is a particle’s property that describes how its spin is related to its momentum. Left (right) transformations affect only left- (right-) handed particles. This property plays an important role in the standard model: only left-chiral fermions (and right-chiral antifermions) take part in the charged weak interaction, so left- and right-handed fields of quarks and leptons transform differently under $SU(2)_L$. Right-handed fields are singlets; left-handed fields are doublets. Therefore, weak

²This description of the SM assumes massless neutrinos, although it has been proven that neutrinos oscillate and change flavor when propagating through space, showing that neutrinos have non-zero masses. This fact requires a modification of the SM to include a lepton mixing matrix, called PMNS matrix [8].

interactions violate parity (P), the transformation that inverts all spatial coordinates. Strong and electromagnetic interactions are P symmetric instead. Weak interactions also violate CP , the combined transformation of parity and charge-conjugation. The latter, denoted with C , inverts all quantum numbers of a particle. Electromagnetic interaction is CP symmetric. The strong interaction could violate CP symmetry too, but no experimental evidence of that has ever been observed. According to a quantum-field theorem [9], all interactions are symmetric under the combined CPT transformation, where T inverts the time axis. This implies that particles and anti-particles have the same mass and lifetime, as experimentally observed so far.

1.2 The quark-flavor sector

The *flavor* sector of particle physics refers to the study of the fermion species: the six quarks and six leptons, each with its individual flavor. In this Section, I will restrict the focus to flavor-changing interactions of quarks.

The development of flavor physics began in the early 1960's, when there were three known quarks (u, d, s). The inconsistencies in measurements of muon decay, neutron decay, and strange-particle decays led Gell-Mann and Levy [10], and then Cabibbo [11], to introduce a mixing angle θ_C between the *strange* and *down* quarks. With the addition of this new parameter, inconsistencies seen before were solved, but the corrected theory at that time predicted some rare kaon decay rates (*e.g.* that for $K^0 \rightarrow \mu^+ \mu^-$) inconsistent with experimental limits: this was corrected by Glashow, Iliopoulos and Maiani [12] by postulating the existence of a fourth quark, the *charm* quark, which gave an additional factor in "loop" amplitudes that suppresses the rates. Lastly, Kobayashi and Maskawa generalized Cabibbo's theory from a four-quark model to a six-quark model to include the phenomenon of CP violation observed in 1964 [13]. They introduced a matrix that describes the flavor-mixing between different quarks, the Cabibbo-Kobayashi-Maskawa matrix (CKM).

This CKM matrix has dimension $N \times N$, where N is the number of quark families. It has $\frac{N(N-1)}{2}$ independent angles and $\frac{(N-1)(N-2)}{2}$ physics phases. If $N = 2$, the only free parameter is the Cabibbo angle θ_C , while if $N = 3$ there are three angles (θ_{12} , θ_{23} and θ_{13}) and a complex phase (δ) which is responsible for CP violation. Kobayashi and Maskawa postulated that, in order to include this phase, three generation of quarks are required, even if no sign of the last family was

yet present at that time. The matrix can be written as follows:

$$V_{\text{CKM}} = \begin{pmatrix} V_{ud} & V_{us} & V_{ub} \\ V_{cd} & V_{cs} & V_{cb} \\ V_{td} & V_{ts} & V_{tb} \end{pmatrix}, \quad (1.5)$$

where V_{ij} indicates the coupling between an up-type quark i and a down-like quark j , mediated by the emission of a W^\pm boson. By expressing the matrix in terms of the four free parameters, it can be rewritten as follows:

$$V_{\text{CKM}} = \begin{pmatrix} 1 & 0 & 0 \\ 0 & c_{23} & s_{23} \\ 0 & -s_{23} & c_{23} \end{pmatrix} \begin{pmatrix} c_{13} & 0 & s_{13}e^{-i\delta} \\ 0 & 1 & 0 \\ -s_{13}e^{i\delta} & 0 & c_{13} \end{pmatrix} \begin{pmatrix} c_{12} & s_{12} & 0 \\ -s_{12} & c_{12} & 0 \\ 0 & 0 & 1 \end{pmatrix}, \quad (1.6)$$

where s_{ab} (c_{ab}) indicates the sine (cosine) of the angle θ_{ab} , and ab indicate the generations involved. Experimentally measured values of the three angles point out a hierarchy between them ($s_{13} \ll s_{23} \ll s_{12}$), while the phase implies a small violation of the CP symmetry although its value is relatively high ($\delta \approx 66^\circ$). The *Wolfenstein* parameterization [14] reflects the hierarchy of the three angles, expressing the matrix in terms of $\lambda = s_{12} \approx 0.225$:

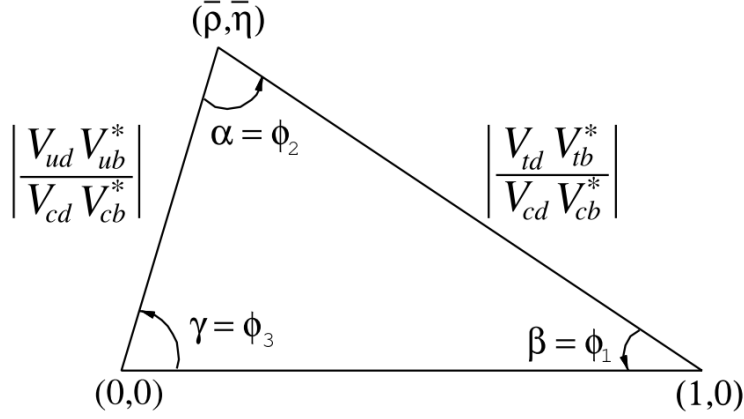
$$V_{\text{CKM}} = \begin{pmatrix} 1 - \lambda^2/2 & \lambda & A\lambda^3(\rho - i\eta) \\ -\lambda & 1 - \lambda^2/2 & A\lambda^2 \\ A\lambda^3(1 - \rho - i\eta) & -A\lambda^2 & 1 \end{pmatrix} + \mathcal{O}(\lambda^4). \quad (1.7)$$

The parameter λ expresses the mixing between the first and second quark generations, A and ρ are real parameters, and η is the parameter that accommodates CP violation.

The unitarity condition of the CKM matrix ($V_{\text{CKM}}^\dagger V_{\text{CKM}} = \mathbb{1}$) allows to obtain the following relations between elements:

$$\begin{aligned} \sum_{k=d,s,b} |V_{ik}|^2 &= 1 & \sum_{k=u,c,t} |V_{kj}|^2 &= 1 & \forall i, j, \\ \sum_{k=d,s,b} V_{ik}V_{jk}^* &= 0 & \sum_{k=u,c,t} V_{ki}V_{kj}^* &= 0 & \forall i \neq j. \end{aligned} \quad (1.8)$$

The latter two relations give rise to six combinations, which could be represented in the complex

Figure 1.2: Sketch of the *unitary triangle* [16].

plane as triangles. Usually, the relation used for this representation is

$$V_{ub}V_{ud}^* + V_{cb}V_{cd}^* + V_{tb}V_{td}^* = 0, \quad (1.9)$$

where all the terms have the same order of magnitude in terms of the parameter λ ; other relations compose nearly-degenerate triangles in the complex plane. Areas of all triangles are the same, half of the Jarlskog invariant J [15], which is a phase-convention independent measure of CP violation defined by $\text{Im}[V_{ij}V_{kl}V_{il}^*V_{kj}^*] = J \sum_{m,n} \epsilon_{ikm}\epsilon_{jln}$, where ϵ_{abc} indicates the Levi-Civita tensor. Normalizing Eq. 1.9 by $V_{cb}V_{cd}^*$ and taking the conjugate, we obtain

$$1 + \frac{V_{ud}V_{ub}^*}{V_{cd}V_{cb}^*} + \frac{V_{td}V_{tb}^*}{V_{cd}V_{cb}^*} = 0, \quad (1.10)$$

whose single terms indicate the sides' length of the triangle. This relation is referred to as the *unitary triangle* (UT), whose vertices are $(0,0)$, $(1,0)$ and $(\bar{\rho}, \bar{\eta})$, where $\bar{\rho} = \rho(1 - \lambda^2/2 + \mathcal{O}(\lambda^4))$ and $\bar{\eta} = \eta(1 - \lambda^2/2 + \mathcal{O}(\lambda^4))$. The angles are referred to as α or ϕ_2 , β or ϕ_1 , and γ or ϕ_3 . A sketch of the triangle in the complex plane is shown in Fig. 1.2.

1.2.1 Current picture

The CKM matrix elements are related to the four fundamental parameters of the SM describing quark-flavor mixing and their precise determination is an important goal of flavor-physics experiments. This is achieved by performing several complementary measurements of the elements to check for an overall consistency of the CKM picture. Measurements can be displayed and compared in the complex plane $(\bar{\rho}, \bar{\eta})$, pointing out disagreements between angles and sides of the UT.

The magnitudes of CKM matrix elements are usually measured with semileptonic or fully leptonic decays. The measured decay rates of the respective quark-flavor changing transitions are proportional to the coupling strength $|V_{ij}|^2$. This is the case for the matrix element $|V_{cb}|$, focus of this thesis, which is extracted by analyzing $B \rightarrow X_c \ell \nu_\ell^3$ transitions, where X_c is a hadron containing a c quark and ℓ either an electron or a muon (this will be extended in Section 1.4). Measurements of $|V_{ij}|$ elements need input from theoretical calculations to factor out the strong interaction from the decay rate as the quarks involved are bound in hadrons. Therefore, improvements in the determination of the matrix-element strengths require advancements in both the experimental measurements and QCD calculations. The current status [16] confirms the almost diagonal hierarchical structure of the CKM matrix:

$$V_{\text{CKM}} = \begin{pmatrix} 0.97435 \pm 0.00016 & 0.22501 \pm 0.00068 & 0.003732^{+0.000090}_{-0.000085} \\ 0.22487 \pm 0.00068 & 0.97349 \pm 0.00016 & 0.04183^{+0.00079}_{-0.00069} \\ 0.00858^{+0.00019}_{-0.00017} & 0.04111^{+0.00077}_{-0.00068} & 0.999118^{+0.000029}_{-0.000034} \end{pmatrix}. \quad (1.11)$$

The CKM matrix parameters can be most precisely determined by using a global fit that combines all available measurements and imposes the SM constraints (*e.g.*, three generation unitarity). The fit also uses theory predictions for hadronic matrix elements, which sometimes give the largest uncertainties. Currently, there are two approaches to combine the experimental data, given by the CKMfitter [17] and UTfit [18] collaborations. They provide similar results; Figure 1.3 shows the result obtained by the CKMFitter in March 2024 as an example.

The global picture is that the CKM description is the dominant mechanism at play. Despite this remarkable consistency, possible deviations of up to 10-20% are still unconstrained, especially those associated with rare decay processes. Most of the relevant measurements are currently dominated

³Charge conjugation is always implied through the document, unless stated otherwise.

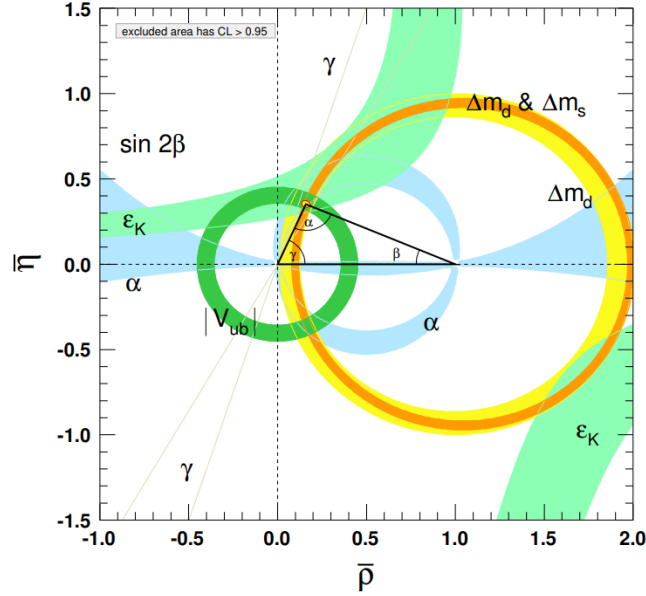


Figure 1.3: CKM global fit results and the constraints on $\bar{\rho}$ and $\bar{\eta}$ [17].

by statistical uncertainties, offering therefore promising opportunities for future experiments.

1.3 Extending the standard model

The SM framework has been completed in the 1970's. Since then, it has been abundantly tested in a range of energies from a few eV to a few TeV, where the experimental results confirmed the SM predictions with great precision. However, this model unlikely is the ultimate theory of Nature. There are still several questions that must be addressed. The SM relies on about twenty free parameters, which must be determined experimentally, that shape the world as we know it. The theory gives no explanation about the values that these fundamental parameters take. For instance, we have no clue on the origin of the hierarchical pattern of fermion masses or of the quark-mixing couplings in the CKM matrix. We also have no idea why there are three families of fermions in first place. Besides these questions concerning the model itself, there are also clear observations from cosmology and astrophysics indicating that the SM is incomplete, as it cannot provide an explanation for them within its current form. For instance, the SM fails to predict the asymmetry observed between matter and anti-matter in the Universe; or, it has no particle candidate for the

non-interacting matter (dark matter) that should populate the galactic halo. In addition, gravity must be also included in a particle physics theory, eventually.

Developing an extension of the SM is the main goal of modern particle physics. This is currently carried out via two approaches. The *direct* approach works at the energy frontier, using high-energy collisions to produce new on-shell particles that are not included in the current formulation of the SM. The new particles would be observed by detecting directly their decay products. This approach would provide striking, clear evidence of new phenomena, but it is limited by the maximum energy reachable at colliders.

The *indirect* approach aims to search for discrepancies between high-precision measurements and equally precise SM predictions in low-energy processes. The basic idea is that the discrepancy would be due to new massive particles that can take part *virtually* in the amplitude of the process. Taking an example from the past, this is exactly what happened with the $K_S^0 \rightarrow \mu^+ \mu^-$ decay before the GIM mechanism and the introduction of the *charm* quark, the new massive particle at that time. With the indirect approach, experimental evidence is typically harder to establish, but there are no restriction regarding maximum collision energies reachable by experiments.

Precision tests of forbidden or suppressed processes in the SM are powerful probes of the indirect approach. The SM features several accidental properties (*i.e.*, properties that are not postulated but arise automatically in the model), which can be challenged to look for new phenomena. Among these: baryon number conservation; the universality of the gauge couplings for the three charged leptons; the absence of interactions via a single W^\pm emission that change the flavour but not the charge (the so-called flavour-changing neutral current, forbidden at “tree level” in the SM). Most of the measurements for these tests are limited by the current samples’ size, but the potential sensitivity to new physics equally depends on the achievable experimental and theoretical precision. New experiments to accumulate more data of higher quality have just started, like Belle II or the upgrade of the LHCb experiment. Further upgrades are under development or discussion. Considering the experimental opportunities, assessing the factors that will limit the precision in the SM prediction of golden quark-flavour probes is critical. It turns out that, in several rare processes, a major limitation is due to the current knowledge of the strength of the matrix element V_{cb} [19]. Improving its determination is pivotal for the discovery potential of future quark-flavor experiments.

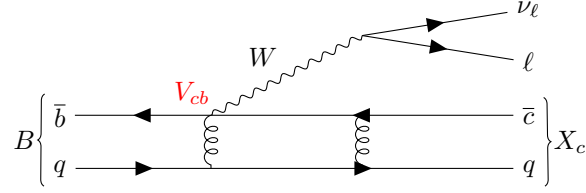


Figure 1.4: Feynman diagram of the $B \rightarrow X_c \ell \nu_\ell$ decay, where X_c is a meson containing a *charm* quark while ℓ is an electron or a muon. The gluons are represented by spring-like lines.

1.4 The CKM element V_{cb}

The CKM matrix element V_{cb} is the weak coupling between *bottom* and *charm* quarks. Recalling the Wolfenstein parametrization, a precise measurement of its strength, $|V_{cb}|$, amounts to a precise determination of the parameter A , since the Cabibbo angle $\lambda \sim \theta_C$ is known with only 0.2% uncertainty. In this respect, the measurement of $|V_{cb}|$ yields a fundamental SM parameter.

Rates of several rare processes, highly sensitive to potential beyond-SM contributions, are proportional to A^4 [20]; an uncertainty as small as 5% on A would lead to a 20% uncertainty on the SM prediction for the rate of those processes, hardly sufficient for a high-precision test when experimental uncertainties aim to get lower than a few percent (or at most 10% in the next decade).

Semileptonic decays of B mesons, $B \rightarrow X_c \ell \nu_\ell$, where X_c is a meson containing a *charm* quark, and ℓ is either an electron or a muon, proceed through the electroweak transition $b \rightarrow c \ell \nu_\ell$, as illustrated in Fig. 1.4. This is governed by the CKM-matrix elements V_{cb} and, since the intermediate W boson decays leptonically, does not involve any other CKM matrix elements. Hence, measurements of the $B \rightarrow X_c \ell \nu_\ell$ decay rate can be used to directly measure $|V_{cb}|$.

Semileptonic $B \rightarrow X_c \ell \nu_\ell$ decays have branching fractions of a few percent, thus providing large samples. Experimentally, reconstructing the neutrino in the final state is challenging as it can not be directly detected; however, these decays can be easily identified by a lepton carrying, on average, a large momentum, combined with a *charm* meson, which can be fully reconstructed with good efficiency. Theoretically, since the leptons in the final state do not interact strongly, the decay amplitude of a semileptonic decay can be factorized into a hadronic and a leptonic current (this will be expanded in Sec. 2.1). The challenge in the extraction of $|V_{cb}|$ is the determination of the decay matrix element of the hadronic current. For this purpose, different theoretical methods have been developed, depending on the specific decay mode under consideration and involving different

approximations. They can be grouped in two major categories:

- The *inclusive method* relies on the sum of all possible *charm* states which the B can decay into with a lepton-neutrino pair. By considering this sum, the partonic level of the $B \rightarrow X_c \ell \nu_\ell$ decays is the only relevant process to consider (an approximation called quark-hadron duality in literature). This eliminates any long-distance dependence (*i.e.* non-perturbative QCD) of the decay amplitude for the final state, while the short-distance correction (*i.e.* perturbative QCD) can be computed in terms of an expansion of the strong coupling constant at the b quark mass scale, $\alpha_S(m_b) \sim 0.2$. The remaining long-distance corrections related to the initial B meson can be expanded in powers of $\Lambda_{\text{QCD}}/m_b \sim 0.1$, where Λ_{QCD} is the hadronic scale of order $m_B - m_b \sim 0.5 \text{ GeV}/c^2$. This approximation is called *heavy quark expansion* (HQE): it systematically expresses the decay rate in terms of non-perturbative parameters that describe universal properties of the B meson.
- The *exclusive method*, where the semileptonic decay of the B meson into a specific *charm* state (*e.g.* D, D^*) is considered. In this case, the hadronic matrix element is parameterized in terms of form factors, which are non-perturbative functions of the recoil energy w of the *charm* meson in the B rest frame. The form factors encapsulate the non-perturbative dynamics of the transition between the initial and final states, providing essential insights into the underlying strong interactions. In $B \rightarrow D \ell \nu_\ell$ decays, form factors describe the transition between the B and the D mesons; similarly, in $B \rightarrow D^* \ell \nu_\ell$ decays, that from the B to the D^* . Precise theoretical calculations using lattice QCD methods, and experimental information on the shape of the form factors as a function of w , are crucial for extracting $|V_{cb}|$.

These methods rely on different experimental techniques too. They complement each other and provide largely independent determinations (of comparable accuracy) of $|V_{cb}|$. This feature would provide a crucial cross check of the results and of our understanding of semileptonic B decays. Unfortunately, this turned out to be the major limitation in the determination of $|V_{cb}|$. Indeed, the two methods, although reaching individually high precision (about 2% uncertainty) they provide two values of $|V_{cb}|$ that differ by about 6% as shown in Fig. 1.5, completely spoiling the knowledge of this CKM elements.

A precise determination of $|V_{cb}|$ requires improvements to overcome this “inclusive-exclusive puzzle”, both on the theoretical and experimental side. In this thesis, I will focus on the study

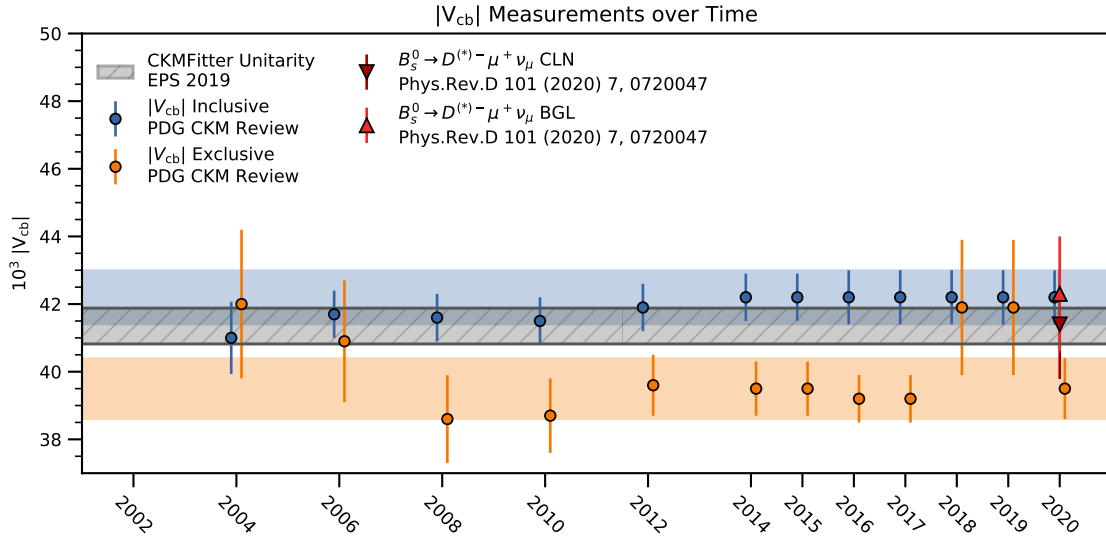


Figure 1.5: Measurements of V_{cb} over the last two decades [21].

of the $B^0 \rightarrow D^{*-} \ell^+ \nu_\ell$ decay, which is the golden channel of the exclusive method. In the next Chapter I will give more details on the theoretical description of semileptonic B decays and the channel of interest, outlining also the target of my study.

Chapter 2

The $B \rightarrow D^* \ell \nu$ decay

This Chapter outlines a phenomenological description of the semileptonic decay $B \rightarrow D^ \ell \nu$. I give a brief experimental status and introduce new model-independent observables sensitive to $|V_{cb}|$, which are the target of my study.*

2.1 Semileptonic B decays: generalities

Semileptonic decays of a *bottom* meson B into a *charm* meson D , a lepton ℓ , and a neutrino proceed through the electroweak decay $b \rightarrow c \ell \nu_\ell$ (Fig. 1.4). The CKM matrix element V_{cb} is the only quark-mixing coupling since the W boson decays leptonically. The other quark making the B meson (a d quark for the B^0 and u quark for B^+) do not engage in the electroweak transition and it is usually considered as a *spectator*.

The decay width can be decomposed as the product of two currents, L^μ and H_μ , by integrating out the contribution of the W boson at tree level, since $m_b \ll m_W$. The decay width takes the form

$$\Gamma \propto G_F^2 |V_{cb}|^2 |L^\mu H_\mu|^2, \quad (2.1)$$

where G_F is the Fermi constant, L^μ is the leptonic current and H_μ the hadronic current, and μ are Lorentz indexes. The leptonic current can be exactly calculated at the elementary-particle level, as it involves only leptons. On the other hand, the hadronic current cannot be, as the quarks are bounded in mesons. Indeed, the spectator quark can be considered as such only for the weak

interaction; it interacts strongly with the other quark exchanging soft gluons in the B and D mesons. Those interactions cannot be calculated exactly analytically, as perturbative QCD fails at this energy scale. An effective approach must be considered, as anticipated in Sec. 1.4. The hadronic current is therefore parameterized in terms of form factors, non-perturbative functions of the squared transferred momentum q^2 between the B and D^* mesons. Its definition can be extracted from w , the scalar product of four-velocities of the two mesons:

$$w = v_B \cdot v_{D^*} = \frac{m_B^2 + m_{D^*}^2 - q^2}{2m_B m_{D^*}}, \quad (2.2)$$

where m_B and m_{D^*} are the masses of the two mesons. The form factors can be computed by employing lattice QCD (LQCD), a non-perturbative method that adapts continuous equations derived from the original QCD Lagrangian in a discrete space, and then solves them numerically. However, these numerical calculations require intense CPU power and time, which limit the accessible phase-space region and achievable precision. The form factors can be calculated only for a few q^2 values close to the maximum values kinematically allowed (q_{\max}^2), and usually have 1-2% uncertainty only at q_{\max}^2 [22–24]. Approximated analytical methods (light cone sum rules, LCSR) are also used [25], but they yield much less precise results; their advantage consists in providing values of the form factors at low q^2 , to complement lattice QCD calculations.

Form factors can also be measured experimentally by analyzing the differential decay rate as a function of q^2 . However only the “shape” of the function can be accessed, *i.e.* only the relative variations of the form factors are measurable. As the decay rate is the product of $|V_{cb}|^2$ and the form factor, to disentangle them, the value of the form factor must be known at least for a q^2 value. Although any q^2 point could work, usually that with maximum precision is used (*i.e.* the value of the form factors at q_{\max}^2 from lattice QCD).

Parameterizations of the form factors are used to extrapolate them at any q^2 value, allowing to obtain precise predictions for decay rates. There are different parameterizations, named after the physicists who proposed them. The two most commonly used are:

- **Boyd-Grinstein-Lebed (BGL) parameterization** [26]. The form factors are expanded in a power series of a variable z , a function of q^2 , which takes values much smaller than 1, such that the series converges within a few terms. The series are constructed to satisfy basic constraints imposed by unitarity and flavor symmetries. The free parameters are the

coefficients of the power of z of the series. This is the most generic functional description of the form factors and has an arbitrary number of parameters depending on the truncation order of the series [27, 28].

- **Caprini-Lellouch-Neubert (CLN) parameterization** [29]. The form factors are also expanded in z , but imposing more restrictive theoretical constraints to reduce the number of free parameters. For this reason, it has been the preferred parameterization used in experimental analyses until few years ago. Phenomenologists have strongly criticized its used, as the assumptions made do not allow for enough flexibility to fit the data; resulting uncertainties associated with the form factor parameters and $|V_{cb}|$ are also considered to be underestimated in this approach.

Once the form factors of the decay are known, the value of $|V_{cb}|$ can be determined by a measurement of its branching fraction. This measurement can be differential as a function of the kinematic variables which characterize the decay rate, in order to gain experimental sensitivity from the form factor shape and its knowledge over the phase-space. In the next Section I will discuss the differential decay rate of the $B \rightarrow D^* \ell \nu$ decay.

2.2 Exclusive B meson decay $B \rightarrow D^* \ell \nu_\ell$

The $B \rightarrow D^* \ell \nu_\ell$ decay is a decay of a pseudo-scalar meson into a vector meson and two leptons. The two leptons originate from the virtual W decay: this can be described as the decay of spin-0 particle (the B meson) and into two spin-1 particles (the D^* and the W). The decay amplitude \mathcal{A} can be expressed in terms of three helicity amplitudes ($H_+(w), H_-(w), H_0(w)$) which correspond to the three polarization states of the D^* meson (two transverse and one longitudinal), allowed by angular-momentum conservation. The helicity states are characterized by different angular distributions of the final-state particles. Considering the decay $D^* \rightarrow D\pi$, the kinematics of the full decay can be described by four variables, the recoil energy w and three helicity angles, θ_ℓ, θ_D and χ :

- The recoil energy between B and D^* mesons w . This variable is confined between the minimum value of $w = 1$, corresponding to zero recoil of the D^* meson in the B meson rest frame, and thus the largest transferred momentum q^2 , and the maximum value $w \approx 1.5035$, corresponding to $q^2 = 0$, *i.e.* the largest recoil energy available.

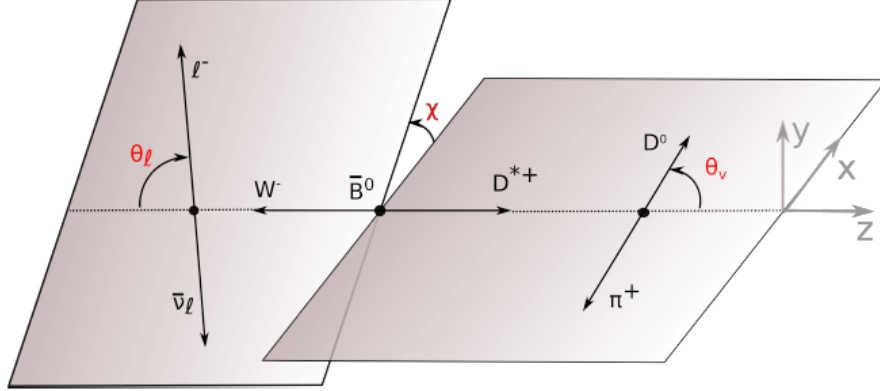


Figure 2.1: Illustration of the three helicity angles in the B rest frame for the decay $B \rightarrow D^* \ell \nu$, where $D^* \rightarrow D^0 \pi_s$ [30]. The π_s is a pion with low momentum in the center-of-mass frame, which is called *soft-pion*.

- Three helicity angles, displayed in Fig. 2.1, which are θ_ℓ , the angle between the direction of the lepton in the virtual W rest frame and the direction of the W in the B rest frame; θ_D , the angle between the direction of the D meson in the D^* rest frame and the direction of the D^* meson in the B rest frame; χ is the angle between the decay planes formed by the W and the D^* meson in the B rest frame.

In the massless lepton limit (*i.e.* for an electron or a muon), the four-dimensional differential decay rate is

$$\frac{d^4\Gamma(\bar{B}^0 \rightarrow D^{*+} \ell^- \bar{\nu}_\ell)}{dw d \cos \theta_\ell d \cos \theta_D d\chi} = \frac{3}{16\pi} \Gamma_0(w) |V_{cb}|^2 |\mathcal{A}(w, \theta_\ell, \theta_D, \chi)|^2, \quad (2.3)$$

where $\Gamma_0(w) = \eta_{\text{EW}}^2 m_B m_{D^*}^2 G_F^2 \sqrt{w^2 - 1} (1 - 2rw + r^2) / (4\pi^3)$, with $r = m_{D^*} / m_B$ and η_{EW} the electroweak correction factor [31]. The decay amplitude \mathcal{A} can be expressed in terms of the helicity amplitudes $H_+(w)$, $H_-(w)$, and $H_0(w)$ as

$$|\mathcal{A}(w, \theta_\ell, \theta_D, \chi)|^2 = \sum_{i=1}^6 \mathcal{H}_i(w) k_i(\theta_\ell, \theta_D, \chi), \quad (2.4)$$

where \mathcal{H}_i and k_i terms are defined in the Table 2.1.

The helicity amplitudes encode the form factors, which are expressed as functions of w . Based on the assumed parameterization, there are different functions that are related to helicity ampli-

i	\mathcal{H}_i	k_i
1	H_+^2	$\sin^2 \theta_D (1 - \cos^2 \theta_\ell)^2$
2	H_-^2	$\sin^2 \theta_D (1 + \cos^2 \theta_\ell)^2$
3	H_0^2	$4 \cos^2 \theta_D \sin^2 \theta_\ell$
4	$H_+ H_-$	$-2 \sin 2\theta_D \sin^2 \theta_\ell \cos 2\chi$
5	$H_+ H_0$	$-2 \sin 2\theta_D \sin \theta_\ell (1 - \cos \theta_\ell) \cos 2\chi$
6	$H_- H_0$	$2 \sin 2\theta_D \sin \theta_\ell (1 + \cos \theta_\ell) \cos 2\chi$

Table 2.1: Functions appearing in the Eq. 2.4 for the selected decay.

tudes. For example, a common basis used for the BGL expansion defines the following form factors functions:

$$g(w) = \frac{H_-(w) - H_+(w)}{2m_B^2 r \sqrt{w^2 - 1}}, \quad (2.5)$$

$$f(w) = \frac{H_+(w) - H_-(w)}{2}, \quad (2.6)$$

$$F_1(w) = m_B \sqrt{1 - 2rw + r^2 H_0(w)}. \quad (2.7)$$

The important point to make is that form factors are functions of the helicity amplitudes. A measurement of the helicity amplitudes as functions of w gives access to the form factors. The three form factor can be expressed using either the BGL or CLN parameterizations. In the case of the BGL parameterization, the parameters are the coefficients of three expansion series in powers of w (one for each function $g(w)$, $f(w)$ and $F_1(w)$), truncated at some arbitrary order. In the case of the CLN parameterization, the helicity amplitudes depend only on four parameters: three values of three form factors at $w = 1$: $h_{A_1}(1)$, $R_1(1)$ and $R_2(1)$; and a shape parameter ρ^2 . Details on the derivation of the form factors and their parameters for the CLN and BGL, are presented in Appendix A.

2.3 Experimental status

From the knowledge of the branching fraction and the form factors, $|V_{cb}|$ can be determined. I will briefly review the current experimental status of these ingredients.

The Heavy Flavor Averaging (HFLAV) group performs averages of the $\bar{B}^0 \rightarrow D^{*+} \ell^- \bar{\nu}_\ell$ branching fraction measurements to obtain the current best-known value [32]. The latest result is obtained

Experiment	$\mathcal{B}(\bar{B}^0 \rightarrow D^{*+} \ell^- \bar{\nu}_\ell)$ [%] (rescaled)
ALEPH [35]	$5.45 \pm 0.26 \pm 0.33$
OPAL inclusive [36]	$5.92 \pm 0.28 \pm 0.57$
OPAL exclusive [36]	$5.11 \pm 0.20 \pm 0.36$
DELPHI inclusive [37]	$4.70 \pm 0.14 \pm 0.35$
DELPHI exclusive [38]	$5.90 \pm 0.20 \pm 0.42$
CLEO [39]	$6.09 \pm 0.19 \pm 0.37$
Belle untagged [33]	$4.90 \pm 0.02 \pm 0.15$
BaBar untagged [40]	$4.69 \pm 0.04 \pm 0.32$
BaBar tagged [41]	$5.49 \pm 0.16 \pm 0.31$
Belle II untagged [42]	$4.60 \pm 0.05 \pm 0.48$
Belle II tagged [34]	$4.51 \pm 0.41 \pm 0.52$
Average	$4.97 \pm 0.02 \pm 0.12$

Table 2.2: Measurements of various experiments and the average of $\bar{B}^0 \rightarrow D^{*+} \ell^- \bar{\nu}_\ell$ branching fractions. The first error is statistical and the second one is systematic. The branching fractions reported are rescaled by HFLAV by adjusting input parameters to common values.

using the measurements presented in Table 2.2, which yield the following average:

$$\mathcal{B}(\bar{B}^0 \rightarrow D^{*+} \ell^- \bar{\nu}_\ell) = (4.97 \pm 0.02 \pm 0.12)\%, \quad (2.8)$$

where the first error is statistical and the second one is systematic. The measurements are all limited by the systematic uncertainties, whose principal sources are: lepton identification and track reconstruction of daughter particles, such as K , π and ℓ ; track reconstruction of the π_s , which is the greatest contribution to systematic uncertainty, is limited by the control sample statistics [33, 34]. These very same sources of systematic uncertainties also affect the $|V_{cb}|$ determination.

Measurements of $|V_{cb}|$ are obtained by assuming a parameterization of the form factors. Due to its reduced set of parameters, the CLN has been the parameterization used in all measurements until about 2017. In this case, the parameter ρ^2 (and in some cases also $R_1(1)$ and $R_2(1)$, see App. A) is measured and then the rate at zero recoil ($w = 1$) is extracted to determine $\eta_{EW} h_{A_1}(1) |V_{cb}|$, where $h_{A_1}(1)$ is the value of the CLN form factor at $w = 1$. HFLAV performed a four-dimensional fit of $\eta_{EW} h_{A_1}(1) |V_{cb}|$, ρ^2 , $R_1(1)$ and $R_2(1)$ with the measurements shown in Table 2.3. These measurements are obtained from both $B^0 \rightarrow D^{*-} \ell^+ \nu$ and decays $B^+ \rightarrow D^{*0} \ell^+ \nu$, assuming isospin symmetry (*i.e.*, the equality of the semileptonic decay width for B^0 and B^+ decays). The results

Experiment	$\eta_{EW} h_{A_1}(1) V_{cb} [10^{-3}]$ (rescaled)	ρ^2 (rescaled)
ALEPH [35]	$31.38 \pm 1.80 \pm 1.24$	$0.488 \pm 0.226 \pm 0.146$
OPAL exclusive [36]	$36.20 \pm 1.58 \pm 1.47$	$1.198 \pm 0.206 \pm 0.153$
OPAL partial reco [36]	$37.44 \pm 1.20 \pm 2.32$	$1.090 \pm 0.137 \pm 0.297$
DELPHI partial reco [37]	$35.52 \pm 1.41 \pm 2.29$	$1.139 \pm 0.123 \pm 0.382$
DELPHI exclusive [38]	$35.87 \pm 1.69 \pm 1.95$	$1.070 \pm 0.141 \pm 0.153$
CLEO [39]	$40.16 \pm 1.24 \pm 1.54$	$1.363 \pm 0.084 \pm 0.087$
Belle [33]	$34.82 \pm 0.15 \pm 0.55$	$1.106 \pm 0.031 \pm 0.008$
BaBar exclusive [40]	$33.37 \pm 0.29 \pm 0.97$	$1.182 \pm 0.048 \pm 0.029$
BaBar D^{*0} [43]	$34.55 \pm 0.58 \pm 1.06$	$1.124 \pm 0.058 \pm 0.053$
BaBar global fit [44]	$35.45 \pm 0.20 \pm 1.08$	$1.171 \pm 0.019 \pm 0.060$
Average	$35.00 \pm 0.11 \pm 0.34$	$1.211 \pm 0.014 \pm 0.019$

Table 2.3: Measurements of the Caprini, Lellouch and Neubert (CLN) form factor parameters in the $\bar{B}^0 \rightarrow D^{*+} \ell^- \bar{\nu}_\ell$. The first error is statistical while the second is systematic. Since most analyses does not measure $R_1(1)$ and $R_2(1)$, only $\eta_{EW} h_{A_1}(1) |V_{cb}|$ and ρ^2 are shown. The reported values are rescaled by HFLAV by adjusting input parameters to common values.

of the fit are:

$$\eta_{EW} h_{A_1}(1) |V_{cb}| = (35.00 \pm 0.36) \times 10^{-3}, \quad (2.9)$$

$$\rho^2 = 1.121 \pm 0.024, \quad (2.10)$$

$$R_1(1) = 1.269 \pm 0.026, \quad (2.11)$$

$$R_2(1) = 0.853 \pm 0.017, \quad (2.12)$$

where the uncertainties include both statistical and systematic contributions.

To obtain $|V_{cb}|$, the input value for the form factor normalization is required. The best known value from averages of lattice QCD calculations [45, 46] is

$$\eta_{EW} h_{A_1}(1) = 0.910 \pm 0.013, \quad (2.13)$$

where $\eta_{EW} = 1.0066 \pm 0.0050$, from which HFLAV obtains

$$|V_{cb}| = (38.46 \pm 0.40 \text{ (exp)} \pm 0.55 \text{ (th)}) \times 10^{-3}, \quad (2.14)$$

where the first uncertainty combines the statistical and systematic uncertainties from the exper-

imental measurement and the second is theoretical (lattice QCD calculation and the electroweak correction).

The CLN parameterization has been criticized by several phenomenological papers in recent years [47, 48], due to restrictive theoretical assumptions used to reduce the number of free parameters. Since no uncertainty is associated to those assumptions, the general prejudice is that uncertainties on the results using this parameterization are usually underestimated. For this reason, recent experimental analyses consider a different paradigm: first, whenever possible, the outcome of the measurements should be model-independent observables that can be analyzed using any model for the form factors; second, the more general parameterization given by BGL should be employed to fit such observables.

The first analysis of a $\bar{B}^0 \rightarrow D^{*+} \ell^- \bar{\nu}_\ell$ reporting model-independent observables is Ref. [49] from Belle in 2017, which was then updated in 2019 [33]. In this analysis, Belle reported one-dimensional distributions of w and the helicity angles θ_ℓ , θ_D , and χ . Despite the approximation of marginalizing the four-dimensional distribution, the four independent one-dimensional distributions lead to the possibility of re-analysing the data *a-posteriori* assuming a different form factor model to describe the differential decay rate with respect to that used by Belle. The additional challenge in this kind of analyses is that of unfolding the experimental effects, such as resolution of the measured kinematic variables and efficiency as a function of those, to provide the kinematic distribution that can be directly employed in phenomenological fits. Belle II contributed also to an analysis of this type using half of the data set collected during 2019-2022 operations [30].

A refined technique, which use improved determination of the neutrino reconstruction, leads to novel results presented in Ref. [50]. The disadvantage of this approach is that it features low efficiency, as the full decay of the B meson accompanying the B meson signal in $\Upsilon(4S)$ decays needs to be reconstructed (so-called *B tagging*). Ref. [50] still makes use of the approximation of marginalizing the full decay rate over four one-dimensional distributions. A different approach to provide model-independent observables that encodes the full four-dimensional information, has been also pursued very recently [51]. In this approach, angular coefficients of the decay rate as a function of w are measured: from those coefficients the full four-dimensional decay rate can be recovered. However, this analysis still requires large data samples, as the method is based again on *B tagging*.

2.4 A novel approach

The Belle II Trieste group is working on a simultaneous analysis of $B \rightarrow D \ell \nu$ and $B \rightarrow D^* \ell \nu$ decays which yields model-independent observables to determine $|V_{cb}|$ from data using any form factor model. The D^* meson of the B decay is partially reconstructed, thus removing the major systematic uncertainty on $|V_{cb}|$ from the soft-pion reconstruction. The method resembles the measurement of the angular coefficients of the $B \rightarrow D^* \ell \nu$ decay rate [51]. The idea is to define observables that are combinations of the helicity amplitudes and $|V_{cb}|$. For $B \rightarrow D^* \ell \nu$ decays, a measurement of the helicity amplitudes $H_i(w)$ gives access to the full decay rate similarly to a measurement of the multidimensional distribution of $(w, \cos \theta_\ell, \cos \theta_D, \chi)$. Such a measurement would yield directly the form factors without assuming any parameterization (*i.e.* in a model-independent fashion), as expressed by the dependence of Eq. 2.5.

These observables allow for an analysis to determine $|V_{cb}|$ using any model of the form factors and any inputs from calculations, in a similar fashion of the analysis of unfolded distributions (but without any approximation due to one-dimensional projection) or of the angular coefficients of $B \rightarrow D^* \ell \nu$ decays (but without the need of B tagging). A first complete study of this approach has been recently presented [52]. In this analysis, the partial reconstruction of the D^* decay prevents the measurement of the $\cos \theta_D$ and χ helicity angles: the full basis of the angular decomposition in Table 2.1 cannot be accessed. However, the higher efficiency of the partial reconstruction provides better statistical sensitivity on those coefficients that are accessible, which are sufficient to reconstruct the full decay rate (up to an ambiguity on the sign of the helicity amplitudes). The study presented in this thesis aims at investigating an expansion to the case where the D^* decay is fully reconstructed, to be sensitive to the full set of angular distributions. In what follows, I present the definition of such model-independent observables.

If only the angle θ_ℓ can be reconstructed (such as for in the D^* partial reconstruction), only the two-dimensional decay rate can be probed. Recalling Eq. 2.3 and integrating in $\cos \theta_D$ (from -1 to 1) and χ (from 0 to 2π), we obtain:

$$\frac{d^2\Gamma}{dw d \cos \theta_\ell} = \frac{1}{2} \Gamma_0(w) |V_{cb}|^2 \{a(w) + b(w) \cos \theta_\ell + c(w) \cos^2 \theta_\ell\}, \quad (2.15)$$

where

$$a(w) = H_+^2(w) + H_-^2(w) + 2H_0^2(w), \quad (2.16)$$

$$b(w) = 2[H_-^2(w) - H_+^2(w)], \quad (2.17)$$

$$c(w) = H_+^2(w) + H_-^2(w) - 2H_0^2(w). \quad (2.18)$$

A measurement of the coefficients $a(w)$, $b(w)$ and $c(w)$ yields the squares of the three helicity amplitudes: the form factors can be measured up to an ambiguity on their signs. Considering N bins of w , we define $3N$ model-independent observables :

$$a'_n \equiv |V_{cb}|^2 a_n = |V_{cb}|^2 a(\bar{w}_n), \quad (2.19)$$

$$b'_n \equiv |V_{cb}|^2 b_n = |V_{cb}|^2 b(\bar{w}_n), \quad (2.20)$$

$$c'_n \equiv |V_{cb}|^2 c_n = |V_{cb}|^2 c(\bar{w}_n), \quad (2.21)$$

where \bar{w}_i is the average value of w in the bin n , with $n = 1, \dots, N$. These are the model-independent observables used in the novel analysis of Ref. [52].

In fully reconstructed $B \rightarrow D^* \ell \nu$ decays it is possible to access the full set of helicity angles. A minimal extension of Eq. 2.15 is the addition of the helicity angle $\cos \theta_D$. In this case, by integrating Eq. 2.3 in the χ variable (from 0 to 2π), we are again left with a combination of the squared helicity amplitudes,

$$\begin{aligned} \frac{d^3\Gamma}{dw d\cos\theta_\ell d\cos\theta_D} &= \frac{3}{8}\Gamma_0(w)|V_{cb}|^2 \{H_+^2(w) \sin^2\theta_D(1 - \cos^2\theta_\ell)^2 \\ &\quad + H_-^2(w) \sin^2\theta_D(1 + \cos^2\theta_\ell)^2 \\ &\quad + 4H_0^2(w) \cos^2\theta_D \sin^2\theta_\ell\}. \end{aligned} \quad (2.22)$$

To maintain the same formalism adopted before and enable a direct comparison of the sensitivity to a measurement of a'_n , b'_n and c'_n , we can rewrite the three-dimensional decay rate in terms of

$a(w)$, $b(w)$ and $c(w)$:

$$\begin{aligned} \frac{d^3\Gamma}{dw d \cos \theta_\ell d \cos \theta_D} &= \frac{3}{32} \Gamma_0(w) |V_{cb}|^2 \left\{ [a(w) + c(w) - b(w)] \sin^2 \theta_D (1 - \cos^2 \theta_\ell)^2 \right. \\ &\quad + [a(w) + c(w) + b(w)] \sin^2 \theta_D (1 + \cos^2 \theta_\ell)^2 \\ &\quad \left. + 4[a(w) - c(w)] \cos^2 \theta_D \sin^2 \theta_\ell \right\}. \end{aligned} \quad (2.23)$$

To resolve the ambiguity on the sign of the helicity amplitudes, we should use the angle χ . So, we can integrate the four-dimensional decay rate in $\cos \theta_D$ (from -1 to 1), to obtain:

$$\begin{aligned} \frac{d^3\Gamma}{dw d \cos \theta_\ell d \chi} &= \frac{3}{32} \Gamma_0(w) |V_{cb}|^2 \left\{ H_+^2 (1 - \cos^2 \theta_\ell)^2 \right. \\ &\quad + H_-^2 (1 + \cos^2 \theta_\ell)^2 \\ &\quad + 4H_0^2 \sin^2 \theta_\ell \\ &\quad \left. - 2H_+ H_- \sin^2 \theta_\ell \cos 2\chi \right\}. \end{aligned} \quad (2.24)$$

In this case the mixed terms containing $H_0(w)$ are again equal to zero, but the mixed term with the product of $H_-(w)H_+(w)$ is now present in the decay rate, enabling to information access about their signs. This would then resolve the ambiguity for the form factor $f(w)$ and $g(w)$ in Eq. 2.5. From the same relations, the sign of $H_0(w)$ must be positive for any value of w , to prevent $F_1(w)$ to be imaginary. When using the decay rate of Eq. 2.24 in an analysis, it is more convenient to define the model-independent observables as:

$$H_{0,n}^{\prime 2} \equiv |V_{cb}|^2 H_{0,n}^2 = |V_{cb}|^2 H_0^2(\bar{w}_n), \quad (2.25)$$

$$H_{+,n}^{\prime} \equiv |V_{cb}| H_{+,n} = |V_{cb}| H_+(\bar{w}_n), \quad (2.26)$$

$$H_{-,n}^{\prime} \equiv |V_{cb}| H_{-,n} = |V_{cb}| H_-(\bar{w}_n). \quad (2.27)$$

2.4.1 Goal and plan of the thesis

This thesis explores the possibility to use the fully reconstructed $B \rightarrow D^* \ell \nu_\ell$ decays to access more information about the form factors with respect to the current analysis with partially reconstructed D^* mesons ongoing within the Trieste Belle II group. The data sample with the signal reconstruction is introduced in Chapter 4. This is a key point of the thesis, as we need to estimate the number

of expected signal candidates and background events to simulate different fitting configurations and assess possible sensitivity to the model-independent observables. Chapter 5 is dedicated to the development of the fit method to measure $a'(w)$, $b'(w)$ and $c'(w)$, either through the two-dimensional decay rate of Eq. 2.15 or the three-dimensional decay rate of Eq. 2.22, so to compare the expected precision on the measurement when passing from a partial to a complete reconstruction of the D^* decay. I investigate the analysis variables that can be used to access the two- or three-dimensional decay rates without performing a neutrino reconstruction. I also implement a fit of the measured model-independent observables, using a BGL parametrization of the form factors as an example, and check the sensitivity to the form factors parameters and $|V_{cb}|$ in the two fit configurations. Finally, I draw the conclusion of my study in Chapter 6.

Chapter 3

The Belle II experiment

The work presented in this thesis uses data collected by the Belle II experiment. This Chapter describes the Belle II detector at the SuperKEKB collider. Lastly, I will briefly describe the simulation used at Belle II.

3.1 The SuperKEKB collider

SuperKEKB is a high-luminosity electron-positron (e^+e^-) energy-asymmetric collider, designed to produce nearly 1000 $B\bar{B}$ pairs per second ($B^0\bar{B}^0$ and B^+B^- in approximately equal proportions) via decays of $\Upsilon(4S)$ mesons produced at threshold [53]. Such colliders are called "B-factories", and were proposed in the 1990's for the dedicated exploration of \mathcal{CP} -violation in B mesons. The main goal of B-factories is to produce low-background quantum-correlated $B\bar{B}$ pairs at high rates.

Intense beams of electrons and positrons are brought to collision at the energy corresponding to the $\Upsilon(4S)$ meson mass, $10.58 \text{ GeV}/c^2$, which is just above the $B\bar{B}$ production kinematic threshold. Such finely tuned collision energy is key. The production of $\Upsilon(4S)$ mesons, which decay in $B\bar{B}$ pairs 96% of the times with little available energy to produce additional particles, suppresses backgrounds, which are mainly due to competing non-resonant hadron production. In addition, usage of beams of point-like particles allows for knowing precisely the collision energy, which sets stringent constraints on the final-state kinematic properties, thus offering additional background suppression. Since bottom mesons are produced in a strong-interaction decay, flavour is conserved, and the null net

bottom content of the initial state implies production of a flavourless $B\bar{B}$ pair; even though B^0 and \bar{B}^0 undergo flavour oscillations before decaying, their time-evolution is quantum-correlated in such a way that no B^0B^0 or $\bar{B}^0\bar{B}^0$ pairs are present at any time. In fact, angular-momentum conservation implies that the decay of a spin-1 particle in two spin-0 particles yields total angular momentum $L = 1$. Because the simultaneous presence of two identical particles in an antisymmetric state would violate Bose statistics, the system evolves coherently as an oscillating $B^0\bar{B}^0$ particle-antiparticle pair until either one decays. This allows identification of the bottom (or antibottom) content of one meson at the time of decay of the other, if the latter decays in a final state accessible only by either bottom or antibottom states. This important capability is called ‘flavour tagging’ and allows measurements of flavour-dependent decay rates, as needed in many determinations of \mathcal{CP} -violating quantities.

Not just $\Upsilon(4S)$ mesons are produced in e^+e^- collisions; Fig. 3.1 shows the hadron-production cross-section in e^+e^- collisions as a function of the final-state mass. The various peaks are radial excitations of the Υ meson and the nearly uniform baseline at about 4 nb represents the so-called continuum of lighter-quark pair production ($e^+e^- \rightarrow q\bar{q}$, where q identifies u, d, c, s), which exceeds $\Upsilon(4S)$ production in rate. In addition, the most frequent outcomes of 10.58 GeV/ c^2 e^+e^- collisions are electroweak processes of lepton production, such as $e^+e^- \rightarrow e^+e^-(\gamma)$, $e^+e^- \rightarrow e^+e^-e^+e^-$ and $e^+e^- \rightarrow \mu^+\mu^-(\gamma)$. These form about 94% of the total cross-section, but can straightforwardly be discriminated online thanks to their distinctive final states.

Because the $\Upsilon(4S)$ mesons are produced at threshold, they would be nearly at rest in the laboratory frame in an energy-symmetric collider. The resulting B mesons too would be produced with low momentum (≈ 10 MeV/ c) in the laboratory, because of the 21 MeV/ c^2 difference between the $\Upsilon(4S)$ mass and the mass of a $B\bar{B}$ pair. With such low momenta they would only travel approximately 1 μm before decaying. The 10 μm typical spatial resolution of vertex detectors would not be sufficient to separate B -decay vertices and enable the study of the decay-time evolution for measurements involving mixing. Asymmetric beam energies are used to bypass this limitation. By boosting the collision center-of-mass along the beam in the laboratory frame, they achieve B -decay vertices separations resolvable with current vertex detectors [54]. SuperKEKB implements a 7-4 GeV energy-asymmetric double-ring design, which achieves a vertex displacement of about 130 μm .

SuperKEKB is designed to deliver collisions corresponding to some tens of ab^{-1} of integrated

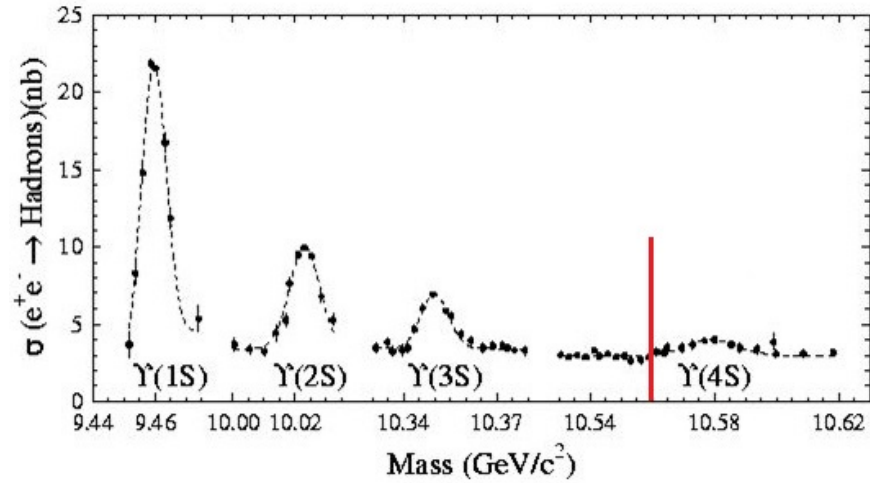


Figure 3.1: Hadron production cross section from e^+e^- collisions as a function of the centre-of-mass energy. The vertical red line indicates the $B\bar{B}$ production threshold.

luminosity by around 2035. This sample corresponds to an order of magnitude more data than the total amount collected by B -factories to date.

To achieve high luminosities, a nano-beam, large crossing-angle collision scheme is implemented [55]. This is an innovative configuration based on keeping small horizontal and vertical emittance and large crossing angle, as shown in Fig. 3.2. This is obtained with a specially designed final-focus superconducting-quadrupole-magnet system, made of magnets, corrector coils, and compensation solenoids installed at each longitudinal end of the interaction region. Functionally the nano-beam scheme mimics a collision with many short micro-bunches, offering great advantages in luminosity with respect to previous schemes. The reduction of the luminous volume size to about 5% with respect to the predecessor KEKB, combined with doubling of beam currents, is expected to yield a factor 40 gain in intensity.

3.2 The Belle II detector

The Belle II detector is a system of multiple subdetectors, each optimized to reconstruct some specific features of the collision final states, arranged in concentric layers forming an approximately cylindrical layout around the collision point of the SuperKEKB accelerator. It is about 8 meters in length, width, and height, and weights 1400 tons. It is located in the same experimental hall and

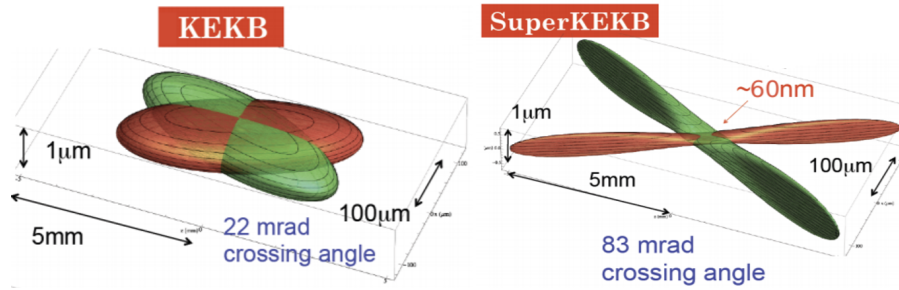


Figure 3.2: Two-dimensional sketch of the nano-beam mechanism implemented in SuperKEKB (right) compared with the previous KEKB collision scheme (left).

has a similar design to its predecessor, the Belle detector. The main subsystems are summarized in Table 3.1 and shown in Fig. 3.3. They are detailed in next Sections and can be broadly classified as follows:

- **Detectors for charged particle tracking:** silicon pixel and strip detectors close to the beam pipe and a wire drift chamber, all immersed in a 1.5 T magnetic field parallel to the beam axis, are used for reconstruction of charged-particle trajectories.
- **Detectors for particle identification:** Cherenkov radiators, an electromagnetic calorimeter, and scintillators for muon and long-lived neutral hadrons achieve particle identification.
- **Data acquisition system:** a two-stage online trigger is designed to acquire interesting events at the high rates expected at design luminosities.

3.3 Tracking detectors

The innermost detectors are used for charged-particle reconstruction. Effective track reconstruction is of great importance since flavour-physics analyses rely strongly on precise momenta measurements and on precise determination of the decay positions. These accurate measured momenta and vertices allow separation of signal from backgrounds, thanks to narrower signal invariant-mass peaks that are therefore more distinctive from smoothly distributed backgrounds. Moreover, precise vertices measurements are key to determine the decay time, a fundamental quantity for \mathcal{CP} -violating asymmetries measurements involving mixing. To simplify pattern recognition, tracks are first reconstructed in the outer tracking volume, and then are extrapolated into the innermost detector to

Purpose	Name	Component	Channels	θ coverage
Tracking	PXD	Silicon Pixel (DEPFET)	10M	[17°, 150°]
	SVD	Silicon Strip	245k	[17°, 150°]
	CDC	Drift Chamber (He-C ₂ H ₆)	14k	[17° : 150°]
Particle ID	TOP	RICH with quartz radiator	8k	[31°, 128°]
	ARICH	RICH with areogel radiator	78k	[14°, 30°]
Calorimetry	ECL	CsI(Tl)	6624 (Barrel)	[12.4°, 31.4°]
			1152 (FWD)	[32.2°, 128.7°]
			960 (BWD)	[130.7°, 155.1°]
Muon ID	KLM	barrel: RPCs and scintillator strips	θ, ϕ 16k	[40°, 129°]
	KLM	end-cap: scintillator strips	17k	[25°, 40°] [129°, 155°]

Table 3.1: Summary of the detector components.

define coarse regions of interest around their expected intersection points in the inner active layers. If an actual measurement point is found within the region of interest, the event associated to the tracks is included in the pattern recognition algorithm, otherwise it is discarded.

3.3.1 Silicon-pixel vertexing detector

The innermost detector, shown in Fig. 3.4, is a pixel vertexing detector (PXD). Its goal is to sample the trajectories of final-state charged particles in the closest vicinity of the decay position of their long lived ancestors, so that the decay point can be inferred by extrapolation inward.

PXD sensors are based on depleted field-effect transistor technology [57]. They are made of p-channel MOSFET integrated on a silicon substrate, which is fully depleted by applying an appropriate voltage. Incident particles generate electron-hole pairs in the depleted region, and thus induce a current passing through the MOSFET. Sensors are 75 μm thick, which allows on-pixel integration of most of the electronics.

The PXD consists of two sets of rectangular layers, called ladders, arranged around the beam pipe on a cylindrical layout: the inner layer consists of eight ladders at a radius of 14 mm while the outer layer has twelve ladders at 22 mm radius: the PXD extends longitudinally for 174 mm at the radius of the outer layer. It comprises around 8 million pixels, $50 \times (50 - 55) \mu\text{m}^2$ (inner layer) and $50 \times (70 - 85) \mu\text{m}^2$ (outer layer) each. The polar acceptance ranges from 17° to 150°. The transverse impact-parameter resolution is 12 μm , achieved by weighting the charge deposited

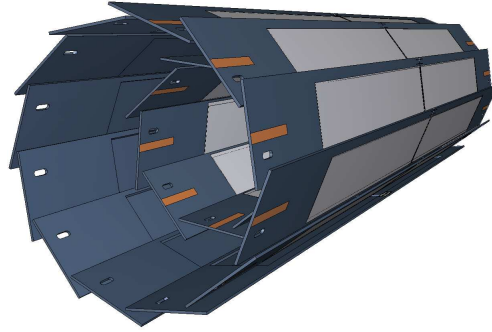


Figure 3.4: Scheme of the PXD detector geometry.

in neighbouring pixels.

Only the inner layer was fully mounted during Run I operations (i.e. between 2019 and 2022) of the experiment, while only two out of twelve ladders had been installed in the outer layer. The full detector was installed during the 2023 long shutdown. During 2024 operations, about 2% of the PXD channels were damaged by two sudden beam losses. Since the machine operations have been unstable due to the push to reach luminosities of about $10^{35} \text{ cm}^{-2} \text{ s}^{-1}$ (the target for 2024), to preserve the safety of the detector it was decided to run the experiment keeping the PXD off until more stable conditions are met. This should hopefully happen in late Fall 2024.

3.3.2 Silicon-microstrip vertexing detector

Around the PXD is the silicon-microstrip vertexing detector (SVD), a silicon detector aimed at reconstructing decay vertices and charged-particle tracks at high spatial resolution [58], an exploded view is reported in Fig. 3.5.

SVD uses double-sided silicon strips. Each sensor is made of a silicon n-doped bulk with an highly p-doped implant on one side. An applied bias increases the depletion region at the p-n junction, and removes intrinsic charge-carriers from the region. Traversing charged particles ionize the silicon, freeing electron-hole pairs that drift due to the electric field, and induce a signal in the highly granular strip electrodes implanted at both ends of the depletion region. The fine segmentation of SVD sensors reduces latency, to deal with the high expected rates.

SVD has a polar-asymmetric geometry that mirrors the asymmetry in particle density resulting from the center-of-mass boost. The polar acceptance ranges from 17° to 150° . SVD is radially

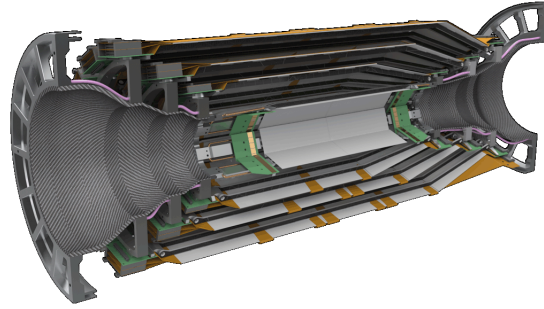


Figure 3.5: Exploded view of a SVD detector half.

structured into four concentric layers at 39, 80, 104, and 135 mm, composed of, respectively, 7, 10, 12, and 16 independently readout modules arranged in a cylindrical geometry.

Sensors are $300\ \mu\text{m}$ -thick, and the separation between adjacent sensing strips (d_{pitch}) ranges from $50\ \mu\text{m}$ to $240\ \mu\text{m}$. Hence, the spatial resolution $d_{\text{pitch}}/\sqrt{12}$ varies with the polar angle. Since the charge associated with an incident particle is usually distributed among several strips, position resolution is improved by interpolation.

3.3.3 Central drift chamber

The central drift chamber (CDC) [59] samples charged-particle trajectories at large radii. It provides trigger signals for events containing charged particles, and contributes to identification of charged-particle species by measuring their specific-ionization energy loss (dE/dx).

When a charged particle traverses the CDC volume, it ionizes the gas, freeing electrons and positive ions from gas atoms. An applied electric field then moves these charges toward the sensing wires, where high field gradients cause an abrupt acceleration with secondary ionizations that induce an electric signal on the sensing wires. The time taken to move these charges from the source position to the wires is called *drift time*. The tracks are reconstructed from the hits in the chamber, and each hit's position is calculated from the drift time.

The CDC has a hollow cylindrical geometry with an inner radius of 16 cm and an outer radius of 113 cm. Fig. 3.6 shows the configuration of the wires inside the CDC. Wires are organized in superlayer: the innermost superlayer contains eight layers, all the others contain six. Superlayers alternate between axial wires and stereo wires. The chamber is composed of 14336 sense wires, with a diameter of $30\ \mu\text{m}$, divided in 56 layers, immersed in a gaseous mixture of 50% He and 50%

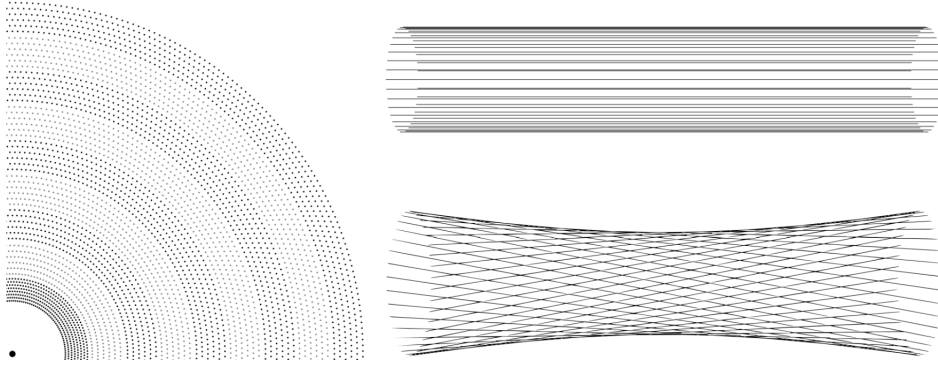


Figure 3.6: The left side shows a quadrant of a slice of the r - ϕ projection of the drift chamber [60]. The innermost superlayer contains eight layers, all the others contain six. The right side shows a visualization of axial wires (top) relative to stereo wires (bottom). The skew is exaggerated.

C_2H_6 (ethane), while 42'240 aluminum wires, with a diameter of 126 μm , shape the electric field. The azimuthal acceptance ranges from 17° to 180° .

The single hit spatial resolution is about 100 μm and the dE/dx resolution is 11.9% for an incident angle of 90° . The typical transverse momentum resolution is $\sigma(p_T)/p_T^2 \approx 0.5\% / [\text{GeV}/c]$.

3.4 Particle-identification detectors

Charged particle identification in the Belle II experiment is mainly performed by two detectors: the time of propagation counter (TOP) and the aerogel ring-imaging Cherenkov counter (ARICH). Both use Cherenkov light to identify charged particles. Particle-identification information is also provided by the electromagnetic calorimeter (ECL) and the K_L^0 and muon detector (KLM).

3.4.1 Time of propagation counter

The time of propagation (TOP) counter is located in the barrel region. It measures the time of propagation of the Cherenkov photons produced by charged particles and undergoing internal reflection in its quartz radiator. A three-dimensional image of the photon cone is reconstructed using the correlation between hit positions in the x-y plane and time of propagation. The TOP consists of 16 quartz bars mounted on the barrel at 1.2 m radius from the interaction point. Each bar is a photon radiator and has three main components, as shown in Fig. 3.7: a long section that

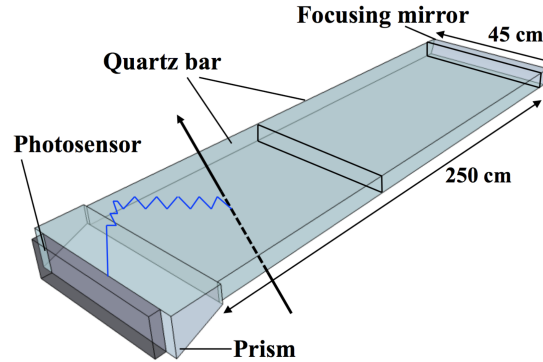


Figure 3.7: Sketch of a TOP quartz bar. A charged particle is shown passing through the radiator and emitting a Cherenkov photon.

acts as a Cherenkov radiator, where photons are generated and propagate towards the bar end; a spherical mirror mounted on the forward end, which focuses the light and reduces the chromatic error; and a prism, mounted on the backward end of the bar, which collects and guides the photons to a photomultiplier.

The polar angular acceptance ranges from 31° to 128° . The single-photon time resolution is about 100 ps, providing a good separation of pions and kaons in the $0.4\text{-}4\text{ GeV}/c$ momentum range (kaon identification efficiency is about 95%, pion fake rate is about 10%). This time resolution is achieved with a micro-channel plate photo-multiplier specially developed for this purpose.

3.4.2 Aerogel ring-imaging Cherenkov

Charged-particle identification in the forward end-cap is provided by the aerogel ring-imaging Cherenkov (ARICH) counter, which measures the Cherenkov ring produced by the passage of charged particles through a radiator. The ARICH provides discrimination between pions and kaons in a broad momentum range, and discrimination between pions, muons, and electrons below $1\text{ GeV}/c$. When charged particles pass through the aerogel radiator, Cherenkov photons are produced; they propagate in the volume where they form a ring on a photon sensitive surface consisting of position-sensitive photo-diodes. Photocathodes are used to convert photons into photoelectrons and generate electrical signals. As shown in Fig. 3.8, two aerogel radiators with different refraction indexes are used to increase the number of generated photons without degrading the

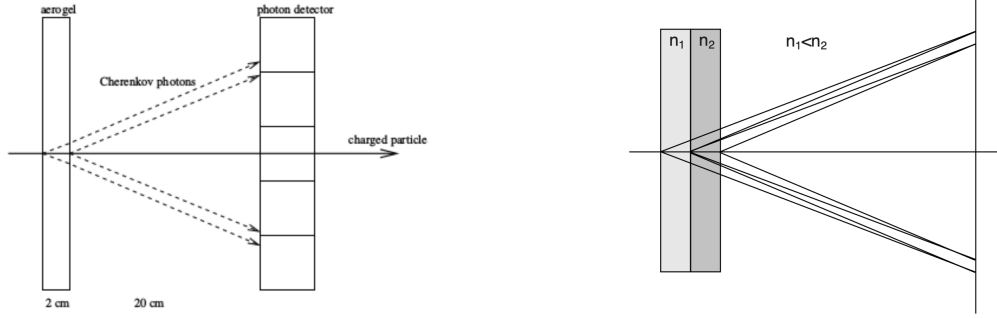


Figure 3.8: Scheme of the ARICH counter.

Cherenkov-angle resolution [61].

The ARICH is composed of 420 modules for photon detection arranged in seven layers extending from 0.41 to 1.14 m radii, and by 248 aerogel tiles placed on the detector endcaps. The polar angular acceptance ranges from 14° to 30° . The observed ARICH performance allows for a 5σ separation between kaons and pions of 0.4-4 GeV/ c momenta, and a 4σ separation between pions, muons and electrons with momenta smaller than 1 GeV/ c .

3.4.3 K_L^0 and muon detection system

The K_L^0 and muon detection system (KLM) detects muons and neutral particles that do not get absorbed in the inner detectors, such as K_L^0 [62]. It is made of alternating 4.7 cm-thick iron plates and active detector elements. Iron elements act also as magnetic flux return for the tracking solenoid. In the inner layers, the active material is scintillator, while in the outer layers glass-electrode resistive-plate chambers are used, with a gas mixture filling the space between electrodes. When particles traverse the KLM, they produce charges that are collected by applying an appropriate voltage. The barrel section of the detector covers 45° to 125° in polar angle. The endcaps cover 20° to 45° and 125° to 155° . Design reconstruction efficiency exceeds 80% for muons with momentum greater than 1 GeV/ c and K_L^0 with momentum greater than 3 GeV/ c .

3.4.4 Electromagnetic calorimeter

The electromagnetic calorimeter (ECL) [56] is a very important part of the Belle II detector, since one third of B -decay products are π^0 or neutral particles that provide photons. These photons

cover a wide energy range, from 20 MeV to 4 GeV and a high electromagnetic energy resolution is fundamental. The ECL reconstructs energy and position of photons and neutral hadrons, but it is also useful for electron and charged hadron reconstruction in regions with limited tracking coverage. ECL permits to identify electrons and separate them from hadrons by extrapolation of CDC tracks. If the incident particle stops in the calorimeter, the total energy is measured. In the ECL, photons and electrons are identified through their kinematics, shower shapes and timing information, as they have different (in shape and magnitude) energy losses with respect to charged hadrons. To separate electrons from photons, information from tracking detectors is correlated with the ECL signal. In addition, the sum of all the reconstructed showers constrains the missing energy in decays involving neutrinos. The ECL also allows for determining luminosity by measuring the Bhabha ¹ scattering rate and using its precisely known cross section.

The ECL is a highly-segmented array of 8'736 thallium-doped, cesium iodide crystals (CsI(Tl)) assembled in a projective geometry pointing to the interaction region (Fig. 3.3). Its detection principle is based on scintillation: the energy released by an incident particle causes a molecular excitation in the material with the passage of an electron from the valence band to the conduction band. The de-excitation of the electron to the valence band is associated with the emission of a photon, called scintillation light, that is usually inefficient and low-energetic. To improve the probability to emit a photon in the visible energy spectrum, thallium impurities are added to create activator sites for the electrons with energy levels in the forbidden zone between the two bands. The CsI(Tl) crystals offer short scintillation time, which reduces the contamination of beam-background photons, which are often 'out of time' with respect to collision products.

The ECL consists of a 3 m-long *barrel* section with an inner radius of 1.25 m and annular end caps at $z = 1.96$ m (*forward*) and $z = -1.02$ m (*backward*) from the interaction point. The polar angle coverage ranges from 12.4° to 155.1° . Between the barrel and the end caps there are two gaps of $\sim 1^\circ$. The barrel has a tower structure that projects to a region near the interaction point of the beams. It contains 6'624 CsI(Tl) crystals with 29 different shapes. Each crystal is a truncated pyramid of an average size of 6×6 cm² in cross section and 30 cm in length (corresponding to $16.1X_0$ radiations lengths). Each crystal is enveloped in a 200 μ m thick Gore-Tex teflon layer, coated by a 25 μ m laminated aluminium and mylar sheets.

¹Bhabha scattering is the electron-positron elastic scattering process $e^+e^- \rightarrow e^+e^-$.

The intrinsic energy resolution of the calorimeter can be expressed as [56]:

$$\frac{\sigma_E}{E} = \sqrt{\left(\frac{0.066\%}{E}\right)^2 + \left(\frac{0.81\%}{\sqrt[4]{E}}\right)^2 + (1.34\%)^2} \quad (3.1)$$

where E is the energy in GeV and the first term is the contribute of the electronic noise. The energy resolution ranges from $\sigma_E/E = 4\%$ at 100 MeV to $\sigma_E/E = 1.6\%$ at 8 GeV. The observed resolution for the reconstructed π^0 mass is $8 \text{ MeV}/c^2$.

3.4.5 Online event selection

Various processes occur in 10.58 GeV e^+e^- collisions (Fig. 3.9). Since events of physical interest for the Belle II program make up for a small fraction of the total cross section, the online event selection (trigger) identifies them in real time while rejecting background events, in order to reduce the data-writing rate. The trigger must be efficient for recording hadronic events from $\Upsilon(4S) \rightarrow B\bar{B}$ and events from the continuum to a manageable level, up to a maximum accept rate of about 30 kHz, due to data-acquisition restrictions. $B\bar{B}$ events have distinctive high-track multiplicity, and therefore are relatively straightforward to select. Events containing τ decays are harder to identify, since they have fewer tracks in the final state and can therefore be misclassified as electrodynamic backgrounds as $e^+e^- \rightarrow e^+e^-$ or $e^+e^- \rightarrow \mu^+\mu^-$ processes, that are not interesting for Belle II physics.

The trigger is composed of a hardware stage called Level1 (L1) [56] followed by a software high-level stage (HLT) [56]. The L1 decision is mainly based on information from CDC and ECL, but also TOP and KLM information is available. The L1 decision feeds the global decision logic [56], that sends out the final trigger based on the information it receives from the detector. The HLT is based on a more complete software reconstruction of the event similar to the offline reconstruction, that uses charged particles from the CDC and energy deposits in the ECL. The HLT selects events based on tracking multiplicity, vertex position, and total energy deposition, achieving a 30% event rate reduction without efficiency loss for $e^+e^- \rightarrow \text{hadron}$ processes.

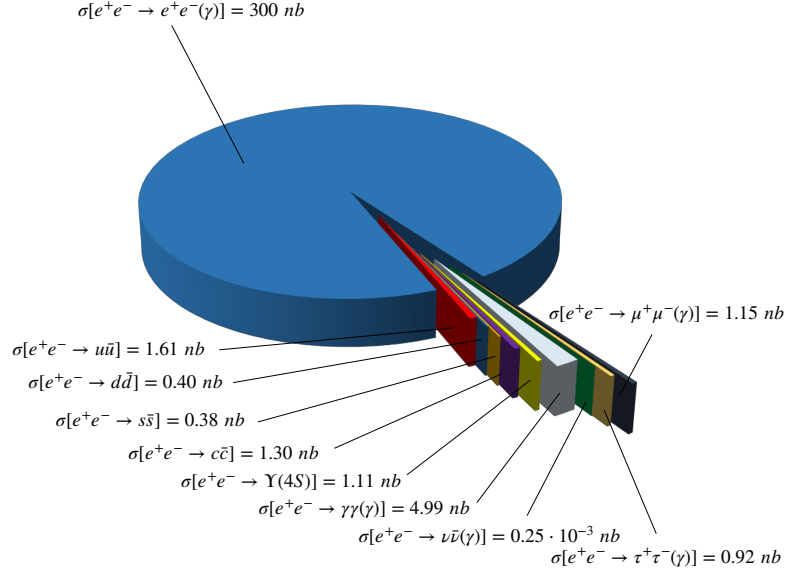


Figure 3.9: Cross sections of the main final states produced in $e^+ e^-$ collision at the $\Upsilon(4S)$ center-of-mass energy.

3.5 Current status of Belle II operations

SuperKEKB produced its first electron-positron collisions in April 2018, while Belle II started taking physics data in January 2019, after a commissioning period. The SuperKEKB collider achieved the world’s highest instantaneous luminosity for a colliding-beam accelerator, setting a record of $2.40 \times 10^{34} \text{ cm}^{-2}\text{s}^{-1}$, in June 2020.² During 2022, constantly higher instantaneous luminosities were recorded, with a maximum value of $\sim 4.4 \times 10^{34} \text{ cm}^{-2}\text{s}^{-1}$. In June 2022, both SuperKEKB and Belle II ended operations to enter a long shutdown period (LS1). During LS1, the PXD detector was extracted and replaced with a new PXD that has a complete outer layer of pixels. At the same time the TOP photomultipliers were upgraded. Other minor updates, regarding both the detector and the collider, were performed. In the recent Run II, the PXD was turned off to prevent further damages until more stable data-taking conditions are reached, probably in October. Run II will go on collecting data until a second long shutdown (LS2), expected in 2027.

The complete data sample available today corresponds to an integrated luminosity of 531 fb^{-1} ,

²Previous world’s highest instantaneous luminosity was set by LHC proton-proton collider at the European Organization for Nuclear Research (CERN) with a value of $2.14 \times 10^{34} \text{ cm}^{-2}\text{s}^{-1}$.

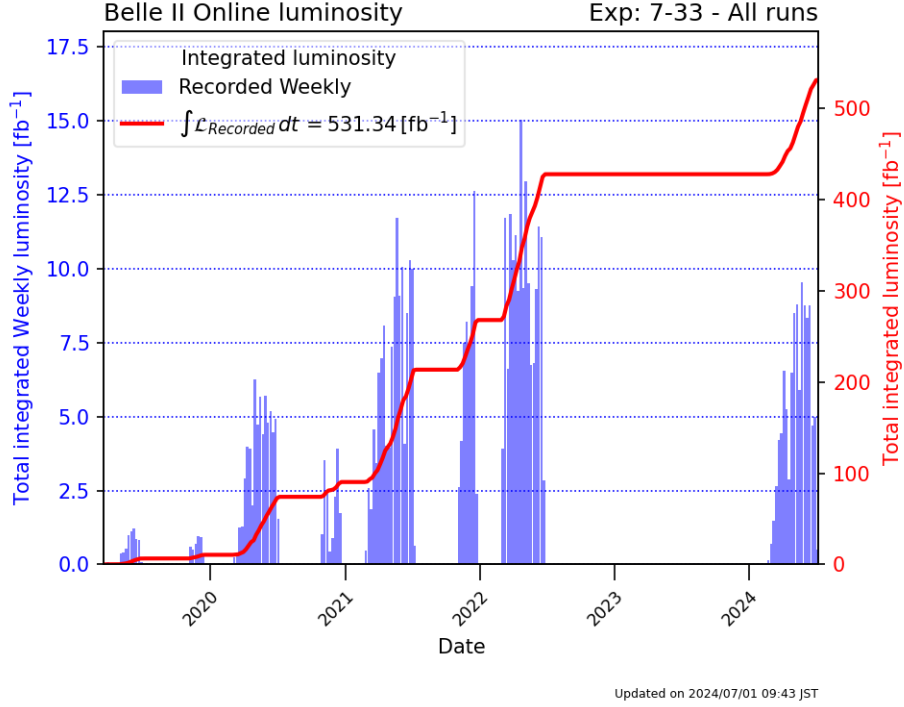


Figure 3.10: Weekly (blue histogram) and total (red line) integrated luminosity recorded using the Belle II detector during 2019-2022 operations of Run I and Run II after the long shutdown [64].

combining both Run I (424 fb^{-1}) and the initial period of Run II (107 fb^{-1}), from March to June 2024. This roughly corresponds to the data set collected by the BaBar experiment in its lifetime (9 years) and about to 50% of the Belle full sample (collected in about 11 years). Of the total Belle II sample, about 85% has been collected at the $\Upsilon(4S)$ resonance, while the rest with collision energy below or above the $\Upsilon(4S)$. The total integrated luminosity as a function of time from January 2019 to June 2024 is shown in Fig. 3.10.

To achieve the goal of collecting 50 ab^{-1} , SuperKEKB needs to be upgraded during the LS2 in order to reach a peak luminosity of $\sim 6.5 \times 10^{35} \text{ cm}^{-2}\text{s}^{-1}$. An international task force has been formed to provide advice to SuperKEKB on the possible upgrade options, which include a redesign of the interaction region and of the final focusing system. LS2 provides the possibility to upgrade parts of the Belle II detector as well. A new vertex detector might be required to accommodate the new interaction-region design, and other sub-detectors might require improved robustness against increasing machine background [63].

3.6 The Belle II software and simulation

The Belle II analysis software framework (basf2) [65] contains open source tools and algorithms for event simulation, reconstruction and analysis. In addition to basf2, other packages are used for event generation in Belle II: EvtGen [66] simulates the B -meson decays, PYTHIA [67] simulates hadronisation, KKMC [68, 69] generates $e^+e^- \rightarrow \tau^+\tau^-$ events, TAUOLA [70, 71] generates τ decays and GEANT4 [72] is used for the detector response simulation.

Monte Carlo (MC) samples are used for three main aspects: to study the expected number of events, to study the background composition of the analyzed samples and the selection efficiency of the applied cuts.

There are two different types of MC simulations used in Belle II: run-independent and run-dependent. The biggest difference between the two is in the beam background description. Run-dependent MC uses samples of background events recorded in data with random triggers (delayed Bhabha) and overlaid to the generated MC signal. For run-independent MC, the background events to be overlaid are simulated, a combination of various single beam backgrounds (*e.g.* beam gas) and low-angle high-cross section physics processes, such as radiative Bhabha or two photon fusion production of e^+e^- . A lot of work has gone into making these simulated backgrounds as realistic as possible, but they do not necessarily reflect reality. The run-dependent MC is also intended to reflect the varying status of the detector, such as dead channels, and the variations in the trigger. Run independent MC does not. Run-dependent simulation has been implemented only recently in the last months. In this work, I study the $B \rightarrow D^*\ell\nu_\ell$ decay using run-dependent MC.

Chapter 4

Data sample and event selections

In this Chapter I discuss the reconstruction and selection of the signal decay $B^0 \rightarrow D^{-} \ell^+ \nu_\ell$ from Belle II data. I use a simulated data set, which fully models the Run I sample, to study the requirements and the resulting sample composition. Finally, I present a comparison of simulated and experimental data for relevant distributions as to assess the simulation quality for the study presented in the next Chapters.*

4.1 Data samples

As described in the Sec. 2.2, the $B^0 \rightarrow D^{*-} \ell^+ \nu_\ell$ decay is particularly suited to measure $|V_{cb}|$: by featuring the largest semileptonic branching fraction (about 5%), it provides the best sensitivity. Experimentally, signal events are easily identified through a lepton paired to a D^* meson. The lepton carries on average a large momentum, which makes the signal distinguishable from hadronic B decays with a secondary semileptonic decay. The D^* meson can be efficiently reconstructed from $D^* \rightarrow D^0 \pi$ decays, and the D^* and D^0 invariant mass distributions feature narrow peaks to discriminate the background. However, the signal presents a key experimental challenge: the undetected neutrino, which makes the decay kinematics incomplete. The only way to access the full kinematics is to reconstruct both the signal and the decay of the accompanying B meson from $\Upsilon(4S)$ events. However, this *tagging* method (presented in Sec. 2.3) has a very low efficiency, generally less than 1%. My analysis, instead, is *untagged*: I will reconstruct only the signal side to retain a

large sample and access the decay kinematics on a statistical basis by using proxy variables. The latter point will be explained in the next Chapter. Here, I focus on the signal side selection.

The Belle II experiment accumulated a data set corresponding to an integrated luminosity of 424 fb^{-1} during Run I; 362 fb^{-1} of them have been taken at the energy of the $\Upsilon(4S)$ mass. This is the sample I focus on: I do not use Run II data as at the time of this work, such very new sample still needed a full calibration and reconstruction.

I use a simulation of the experiment to perform most of the analysis: to optimize the event selection, to choose variables for the fit to extract the signal, and to test multiple fitting configurations. The simulation is based on the Monte Carlo (MC) approach, which consists in producing samples through event-generator algorithms. These are achieved by producing final-state particles of e^+e^- collisions, whose properties and interactions are generated by pseudo-random number algorithms that follow theoretical models. These generated particles pass through the simulated experimental apparatus of Belle II, emulating the response of the detector system and reproducing the expected values of observed quantities.

Regarding beam interactions, the simulation can be *run-dependent* or *run-independent*, as introduced in Sec.3.6: in the first case, each e^+e^- interaction has been simulated accurately to emulate real experimental conditions, while in the second case the simulation is approximated to the mean expected conditions of the experiment. In this work I use run-dependent simulation. The simulated samples contain information about *reconstructed* particles, which have all information available as the experimental data (*e.g.* track parameters, vertexes coordinates, particle-identification likelihood, *etc.*), and *true* particles, which contain the truth-level information of particles in the detector (*e.g.* generated momenta, exact decay points, identification codes, *etc.*). The latter are used in the truth-matching procedure to check if the particles are correctly reconstructed. To ensure the identification of the signal decay chain, I use flag variables created during the truth-matching phase. These variables state if the reconstruction of all particles in the decay chain is correct while allowing for missing momentum caused by the neutrino. This is a key step to individuate the signal sample and inspect background sources.

The simulated data are generated in different samples: signal, background from light quarks (so-called continuum), and background from other B meson decays. For the signal sample, I simulate $e^+e^- \rightarrow B^0 \bar{B}^0$ events, where one of the two B mesons decays according to the signal final state: a lepton, which can be an electron or a muon, a neutrino of the same lepton's flavor, and a D^* meson.

The D^* then decays into a D^0 meson and a π_s , where the subscript “s” stands for *soft*, because this pion features low momentum due to the small difference between the D^0 and D^* masses. Lastly, I use the favored decay where the D^0 meson decays into a kaon and a pion. For the continuum sample, I generate $e^+e^- \rightarrow u\bar{u}$, $e^+e^- \rightarrow d\bar{d}$, $e^+e^- \rightarrow c\bar{c}$, $e^+e^- \rightarrow s\bar{s}$ events. Each quark pair hadronizes to form jets of particles, as pions, kaons, protons, charm mesons and others, which can eventually decay. For the sample of background B decays, called also $B\bar{B}$ background, $e^+e^- \rightarrow B^0\bar{B}^0$ and $e^+e^- \rightarrow B^+B^-$ samples are generated, where B mesons can undergo all possible decays. The total MC sample, composed of the parts presented above, is roughly four times the size of the Run I data set, corresponding to 1444 fb^{-1} .

In addition to these simulated data, I use another type of samples called pseudo-experiments, which are based on random generation of few distributions of interest from templates obtained with the fully simulated sample described above. The pseudo-experiments are usually employed to study fit properties and assess systematic uncertainties in data analysis. I will discuss them more in Sec. 5.3.

4.1.1 Sample components

I study the MC sample to define the selection of the signal channel. For this purpose, it is useful to categorize the sample into components, depending on the origin of the reconstructed particles for the final state. Signal and continuum events are two of such components; background from other B decays are split in three other components. Therefore, I define five sample components:

- Signal candidates, following the decay chain $B^0 \rightarrow D^{*-}l^+\nu_l$, $D^{*-} \rightarrow D^0\pi_s^-$, and $D^0 \rightarrow K^-\pi^+$.
- Continuum candidates, where the majority of events comes from a D^* meson reconstructed from $e^+e^- \rightarrow c\bar{c}$ events, and the lepton originates from a secondary decay of a hadron.
- $Xl\nu_\ell$ candidates, where the reconstructed particles originate from a semileptonic B meson decay different from the signal, $B \rightarrow D^{**}l\nu_\ell$. With D^{**} I indicate the excited D mesons $D_1^{(0,+)}$, $D_1^{\prime(0,+)}$ and $D_2^{*(0,+)}$. The D^{**} particle decays into a D^* meson, which is fully reconstructed, and another particle Y , which is not.
- Fake- D^* candidates, which are events composed of an incorrectly reconstructed D^* decay combined with a lepton, which in most cases is correctly identified and originates from B

meson decays.

- True- D^* candidates, which have correctly reconstructed D^* mesons originating from B meson decays, but associated leptons come from other sources, the majority being a semileptonic decay of the other B meson.

Current measurements of the branching fraction and $|V_{cb}|$ with $B^0 \rightarrow D^{*-}l^+\nu_l$ decay are limited by systematic uncertainties. Those related to background are not the major ones because the general strategy is to apply a selection that minimizes the background impact (uncertainties related to its knowledge and modelling). To select my sample, I follow the same principle of prioritizing signal purity over efficiency¹. In what follows, I describe the selections applied to the data sample. These are inspired by the work done in the analysis currently conducted by the Belle II Trieste group, in which both $B \rightarrow D\ell\nu_\ell$ and $B \rightarrow D^*\ell\nu_\ell$ decays are studied. Similar selections are adopted where possible, to facilitate an possible combination of the two analysis in the future.

4.2 Event selection

The Belle II experiment collects large amounts of data and, depending on the analysis performed, only a fraction of those is used for each study. To ease the reconstruction phase, raw data are centrally processed to produce summary data, called “mDST”, which are reduced in dimension and contain higher-level information related to physics quantities, including four-momenta, vertex positions, particle-identification likelihoods and others. A second centralized step consists in applying loose selection criteria on the mDST data to obtain analysis-specific subsets reduced in dimension (5% of the mDST) that can be released to collaborators for detailed studies. This is called *skimming*. An optimal skimming is important because any signal inefficiency occurred at this stage is laborious to recover. In the next Section I present the skimming selection applied. After the skimming, I show the study conducted to find selection criteria with the goal of increasing signal purity. These criteria are identified through the inspection of variable distributions in which the signal shape differs from that of the background.

¹Signal purity is the percentage of signal events on the total events present in the sample, while efficiency is the ratio between the events after and before selection(s).

4.2.1 Skim selection

The following selection criteria are applied in the skimming phase. Each requirement, if not specified otherwise, is applied to both the electron and muon channels.

- Measurements of distances between interaction points and charged tracks are used to individuate possible tracks caused by beam interactions with residual gases in the beam line. Usually, the quantities used are the longitudinal (dz) and transverse (dr) distances of a track from the interaction point. In this work, I require $|dr| < 1.0$ cm and $|dz| < 3.0$ cm for all charged particles. Additionally, all tracks are required to be in the CDC angular acceptance ($17^\circ < \theta < 150^\circ$) and have at least 20 hits in the CDC.
- The momentum of the kaon in the center-of-mass frame must be over 0.5 GeV/c. This is done to suppress background from low-momentum tracks.
- The visible energy of the event in the center-of-mass frame is required to be larger than 4 GeV, to avoid including events in which there are no B mesons.
- The momentum of the rest-of-event (ROE) particles must be less than 3.2 GeV/c in the center-of-mass frame. Among all the tracks in an event, ROE particles are those tracks that are not used for the signal reconstruction. For a signal event, ROE particles are daughter particles of the other B meson of the $\Upsilon(4S)$ decay.
- The momentum of the lepton in the center-of-mass frame must be over 0.6 GeV/c. This ensures to select B events with semileptonic decays.
- The Fox Wolfram variable R_2 , which is defined as the ratio between the 2-nd and 0-th order of the Fox Wolfram momenta [73], is required to be under 0.4. The variable R_2 accounts for the shape of the geometrical distribution of the particles in an event, and is usually used to suppress continuum.
- The thrust axis is the most probable direction axis of a particle, obtained by considering its daughters' momenta. The cosine of the angle between the thrust axis of the signal B meson and the ROE is called $\cos TBTO$. For signal events, this is the cosine of the angle between the two B mesons. It is a useful variable for continuum suppression and is required to be less than 0.9.

- Additionally, I use particle identification (PID) information. As seen in Sec. 3.4, several detectors provide information about the nature of the track from a charged particle, and this information is analyzed independently to determine the likelihood of charged particle hypothesis, one for each detector. The likelihood can be used to create a set of binary PID variables, which corresponds to the probability $(0, 1)$ of the first provided mass hypothesis with respect to the second mass hypothesis. I use the following PID variables:
 - Kaon-pion discrimination is used to properly reconstruct the $D^0 \rightarrow K\pi$ decay. This decay is already well identified from the kinematics; also, it has larger branching fraction than the other main background decays ($D^0 \rightarrow KK$ or $D^0 \rightarrow \pi\pi$). Given these motivations, a minimal requirement is sufficient: the PID is set to be higher than 0.1.
 - Another type of binary PID variable is used for muons only, which employs, unlike the kaon PID, information from all detectors except the Silicon Vertex Detector. It is required to be higher than 0.9.
 - For electrons, a Boosted Decision Tree (BDT) is used to distinguish them from the other charged particles by using information from all detectors available. The values accepted are above 0.6.

The criteria above are loose requirements in order to obtain samples of moderate dimensions. The signal efficiencies resulted from these selections for the muon and electron channels are

$$\epsilon(\mu) = (20.58 \pm 0.04) \% \quad (4.1)$$

$$\epsilon(e) = (20.38 \pm 0.04) \% \quad (4.2)$$

The uncertainties are only statistical. The relative fractions of each component in the sample are reported in Tab. 4.1. The signal fractions are about 10% after the skimming, and are different between muon and electron channels. The selections applied in the skimming phase affect differently the two channels since distributions of the requirement variables are different. In the next Section, I present the detailed study on diverse variables to obtain the final sample, which will be used for the analysis.

Component	Muon channel [%]	Electron channel [%]
Signal	9.04 ± 0.02	13.93 ± 0.03
Continuum	35.04 ± 0.03	24.65 ± 0.04
$X\ell\nu$	1.56 ± 0.01	2.42 ± 0.01
True- D^*	6.80 ± 0.02	6.11 ± 0.02
Fake- D^*	47.57 ± 0.03	52.90 ± 0.04

Table 4.1: Relative fractions of each component in the sample after the skimming selections. The uncertainties are only statistical.

4.2.2 Final requirements

After the skimming selections, the sample still needs to be revisited in order to increase the signal purity. So, I carry out the additional selections which are explained in what follows. The selection summary is presented in Table 4.2.

Optimal D^* candidate

To correctly reconstruct the initial B meson, all particles in the chain decay must be correctly identified. For the D^* and D^0 mesons, the invariant masses are ideal variables for this, since they are completely reconstructed and their mass distributions have narrow peaks. The D^0 meson is formed by a kaon and a pion candidate, while the D^* meson is obtained from the combination of the D^0 and a slow pion. An additional variable is the difference of invariant masses of these two mesons, $\Delta M(D^*, D^0)$, which should be distributed around values slightly higher than the rest mass of the charged pion ($m_\pi \approx 0.140 \text{ GeV}/c^2$). This additional variable has a narrower peak than that of invariant masses since part of experimental resolution cancels in the difference. I select values between $[1.855, 1.875] \text{ GeV}/c^2$ for the invariant mass of D^0 and $[0.144, 0.147] \text{ GeV}/c^2$ for the $\Delta M(D^*, D^0)$. In Fig. 4.1, the distributions of $\Delta M(D^*, D^0)$ and D^0 invariant mass are shown after the skimming selections to highlight the importance of these requirements in removing a good amount of continuum and fake- D^* events. The invariant mass of D^0 shows also that both $X\ell\nu$ and true- D^* components peak in the same region of the signal, so further variables need to be inspected. Tails of the $\Delta M(D^*, D^0)$ and D^0 invariant mass are composed exclusively of continuum and fake- D^* events: this will be better explored in Sec. 4.3. The data that I discuss in what follows already include these selections, since they remove a good amount of background while preserving almost all signal events. This allows focusing on the remaining distributions to add targeted requirements.

Object	Requirement
Tracks	$dr < 1 \text{ cm}$ $dz < 3 \text{ cm}$ $17^\circ < \theta_{CDC} < 150^\circ$
Kaons	$p_K^{\text{CMS}} > 0.5 \text{ GeV}/c$ $\text{PID}(K) > 0.1$
D mesons	$0.144 < \Delta M(D^*, D^0) < 0.147 \text{ GeV}/c^2$ $1.855 < M(D^0) < 1.875 \text{ GeV}/c^2$ $p_{D^*}^{\text{CMS}} < 2.5 \text{ GeV}/c$
Continuum	$R_2 < 0.4$ $\cos TBTO < 0.75$
Leptons	$\text{PID}(\mu) > 0.99$ $\text{PID}(e) > 0.90$ $0.8 < p_\ell^{\text{CMS}} < 2.4 \text{ GeV}/c$
Y system	$M(Y) > 3 \text{ GeV}/c^2$ $-1 < \cos \theta_{BY} < 1$
ROE	$p_{\text{ROE}}^{\text{CMS}} < 2.8 \text{ GeV}/c$
Event energy	$E_{\text{visible}}^{\text{CMS}} > 4 \text{ GeV}$

Table 4.2: Summary of the requirements applied. Notice that the requirement on $\text{PID}(\mu)$ is applied only to the muon channel, $\text{PID}(e)$ to the electron channel; the selection on the lepton momentum to both channel.

Continuum suppression

Continuum events make up most of the hadronic events at Belle II, so effective identification and reduction of these backgrounds are essential. In the skimming phase, the requirements on Fox-Wolfram parameter R_2 and $\cos TBTO$ contribute to reduce continuum, but are still quite loose. Among the two, the variable $\cos TBTO$ is more helpful since, as seen in Fig. 4.3, the signal distribution is uniform while the continuum peaks at values near 1. This difference arises from the topology of the event: the B mesons have momentum's directions that are distributed uniformly in the space and might be non-collinear in $\Upsilon(4S)$ decays. For $q\bar{q}$ events, quarks produce jets of particles that are headed in opposite directions. Fig. 4.2 shows a sketch of the two cases. The selected values are those below 0.75, where the reduction of the continuum sample is no longer convenient in favor of the signal sample.

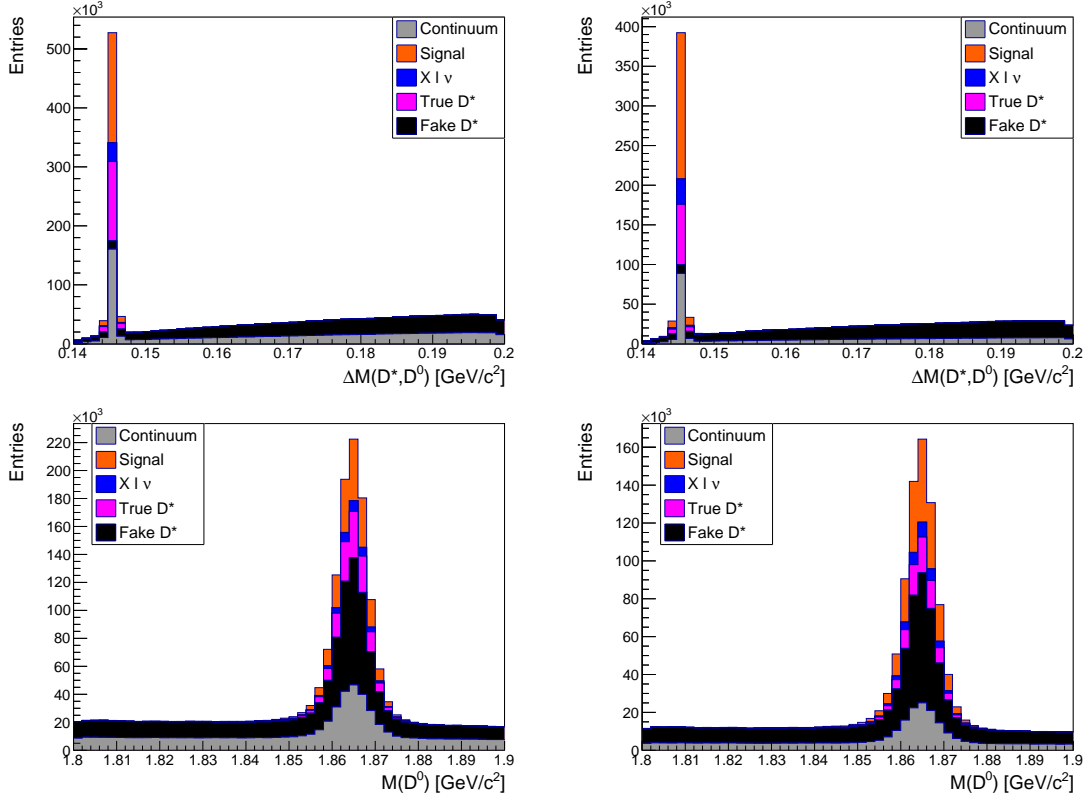


Figure 4.1: Top: distributions of the $\Delta M(D^*, D^0)$ for the muon (left) and electron (right) channel. Bottom: distributions of the $M(D^0)$ for the muon (left) and electron (right) channel. The histograms are stacked.

Kinematic constraints

For the $B^0 \rightarrow D^{*-} \ell^+ \nu_\ell$ decay, through the conservation of four-momenta, the following relation applies:

$$p_B = p_{D^*} + p_\ell + p_{\nu_\ell}, \quad (4.3)$$

or, by making explicit the four-momentum of the neutrino and squaring it,

$$p_{\nu_\ell}^2 = (p_B - p_{D^*} - p_\ell)^2. \quad (4.4)$$

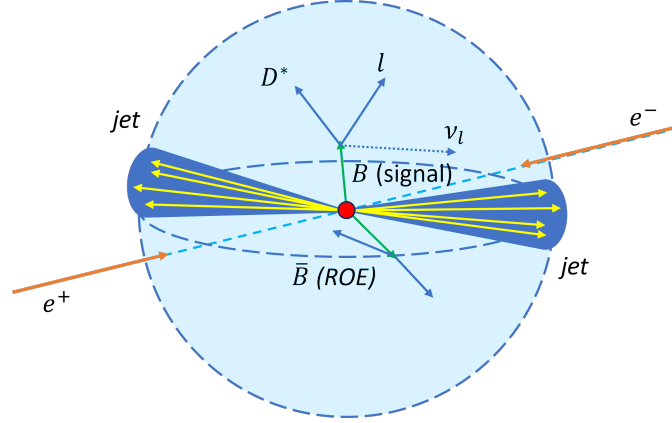


Figure 4.2: Illustration of the topology of an event. Beams of e^+e^- collide to produce a $\Upsilon(4S)$, which then decays into two B mesons: one is the signal, the other is the ROE. The B decays are isotropic. A continuum event is also represented: the $q\bar{q}$ pair hadronizes in two jets of particles headed in opposite directions.

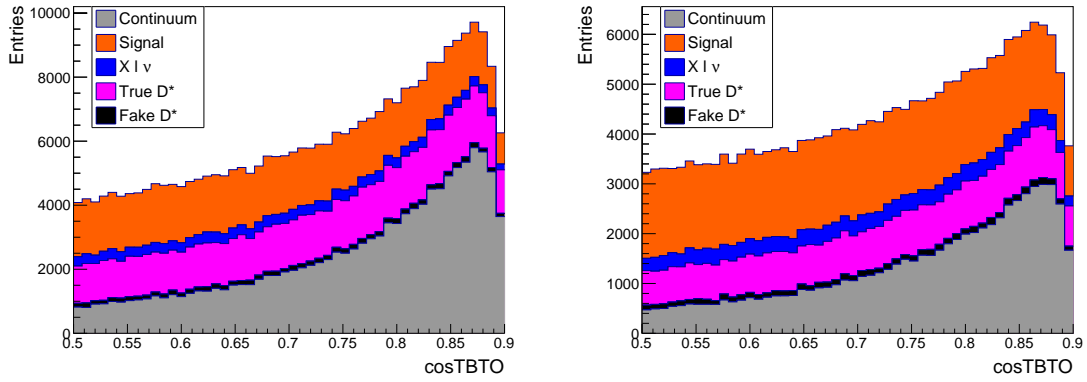


Figure 4.3: Distributions of $\cos TBTO$ for the muon (left) and electron (right) channel. The histograms are stacked.

This must equal zero for a signal neutrino. All four-momenta are in the center-of-mass frame. This can be expanded as:

$$M_B^2 + M_Y^2 - 2E_B E_Y + 2|\vec{p}_B||\vec{p}_Y| \cos \theta_{BY} = 0, \quad (4.5)$$

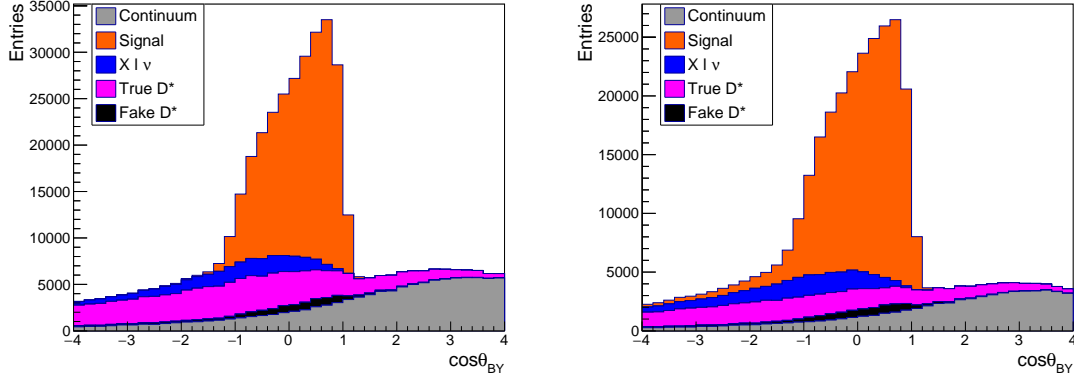


Figure 4.4: Distributions of the $\cos \theta_{BY}$ for the muon (left) and electron (right) channel. The histograms are stacked.

where Y results from the sum of D^* and lepton four-momenta. From the latter equation, an important variable in the analysis is obtained, the cosine between the B meson and the Y system,

$$\cos \theta_{BY} = \frac{2E_B E_Y - M_B^2 - M_Y^2}{2|\vec{p}_B||\vec{p}_Y|}. \quad (4.6)$$

This quantity can be calculated with all available information: the Y system is determined through the measurement of masses and momenta of the lepton and D^* , the value of the B meson mass from PDG [16] ($m_B = 5.27972 \text{ GeV}/c^2$) and the energy is half of the center-of-mass energy, which is about $5.29 \text{ GeV}/c^2$. For the signal, most of the events fall in the physical region $-1 < \cos \theta_{BY} < 1$, which is the range of values accepted in this analysis. These formulae are true by assuming that the only undetected particle is the neutrino. It is important to notice that, in Fig. 4.4, there are more events with $\cos \theta_{BY} < -1$ in the electron channel than in the muon channel for the signal: electrons are subject to bremsstrahlung losses, so the energy and momentum of the Y system are lower than those in the muon channel. This will bring differences in the final efficiency of the two channels.

Another constraint that can be imposed from the kinematic is on the Y system mass, which is required to be above $3 \text{ GeV}/c^2$. Below this value there are few signal events, as shown in Fig. 4.5.

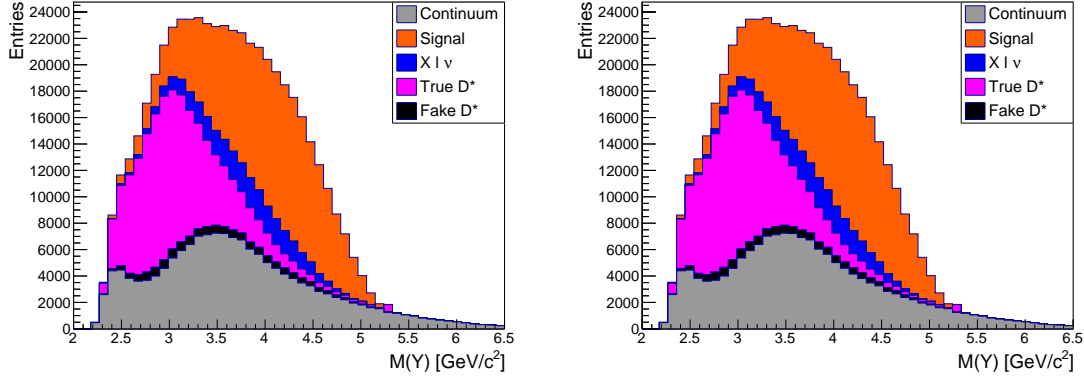


Figure 4.5: Distributions of the $M(Y)$ for the muon (left) and electron (right) channel. The histograms are stacked.

Particle ID criteria

In the skimming phase, particle identifications of muons and electrons are required to be higher than 0.9 and 0.6 respectively, but those thresholds are very loose (see Fig. 4.6). Both particles can be mis-identified, but muons tend to be so more frequently, given that their mass is close to that of charged pions. This is the reason for applying a stricter requirement to the muon channel, selecting PID values higher than 0.99. For electrons, which have a larger tail in the PID distribution, I use a requirement to select PID values higher than 0.9.

Table 4.3 reports the fraction of events removed after the PID selection and the fraction of fake leptons among the removed events. Fake leptons are all particles that are not the lepton indicated in the signal B decay. For instance, in the case of the muon channel, electrons are considered fake leptons, as well as pions, kaons and protons. The two PID requirements work differently on the two channels: the first row indicates how effective the PID selection is in the two channels, removing more events for muons among all components. The second indicates the fractions of fake leptons removed in each component, which are in general larger for muons.

True- D^* background reduction

A true- D^* event is characterized by an incorrect combination of a lepton with a properly reconstructed D^* meson, so inspecting the lepton's characteristics can be helpful. Fig. 4.7 shows the distribution of lepton momentum in the center-of-mass frame for both channels. A good amount

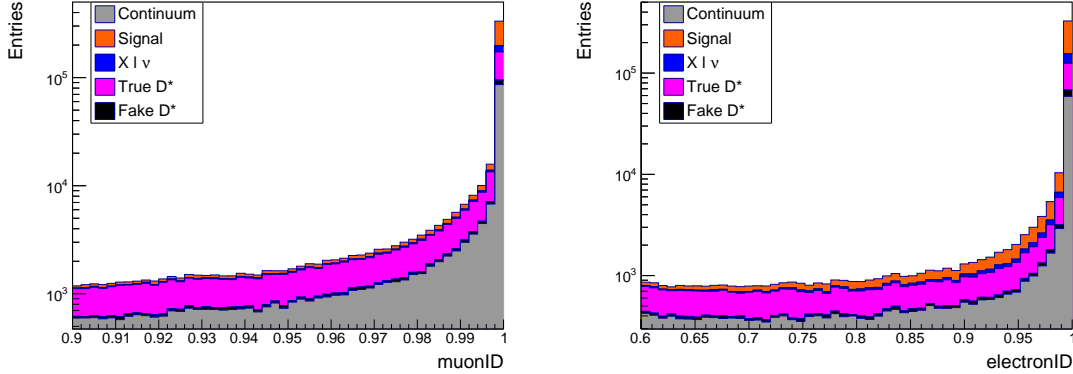


Figure 4.6: Distributions of the particle ID of the two channels in logarithmic scale. The histograms are stacked.

		Signal	Continuum	$X l \nu$	True- D^*	Fake- D^*
Muon	Removed fraction	3.44 ± 0.04	27.91 ± 0.11	6.89 ± 0.14	27.90 ± 0.12	15.16 ± 0.31
	Fraction of fakes	–	88.86 ± 0.15	1.36 ± 0.24	83.00 ± 0.12	73.98 ± 0.97
Electron	Removed fraction	2.44 ± 0.04	17.71 ± 0.13	2.82 ± 0.09	15.23 ± 0.13	7.25 ± 0.25
	Fraction of fakes	–	81.01 ± 0.32	0.76 ± 0.29	69.63 ± 0.42	46.46 ± 1.79

Table 4.3: Fractions (in %) of removed events after the PID selection and, among the removed events, the fraction of fake leptons. Uncertainties are statistical. Fractions are calculated after the $\Delta M(D^*, D^0)$ and $M(D^0)$ selections indicated above, which greatly reduce continuum and fake- D^* components. The signal component has no fake leptons.

of true- D^* events are located at low values of the lepton momentum, mostly due to a secondary semileptonic decay of another meson (*e.g.* a charm meson) from a B decay. This latter component features indeed a lepton momentum on average softer than the signal. For this reason, the selected lepton momenta are values higher than $0.8 \text{ GeV}/c$. Additionally, to fix the range in preparation of the fit, the lepton momentum must have an upper limit of $2.4 \text{ GeV}/c$, while the D^* momentum of $2.5 \text{ GeV}/c$. The latter requirements remove little to none events for all components. The momentum of the ROE in the center-of-mass frame, already mentioned in the skimming phase, can be further selected to be below $2.8 \text{ GeV}/c$. In Fig. 4.8, its distribution is shown for both channels. In the region removed, besides continuum events, many true- D^* events are present while signal events are negligible.

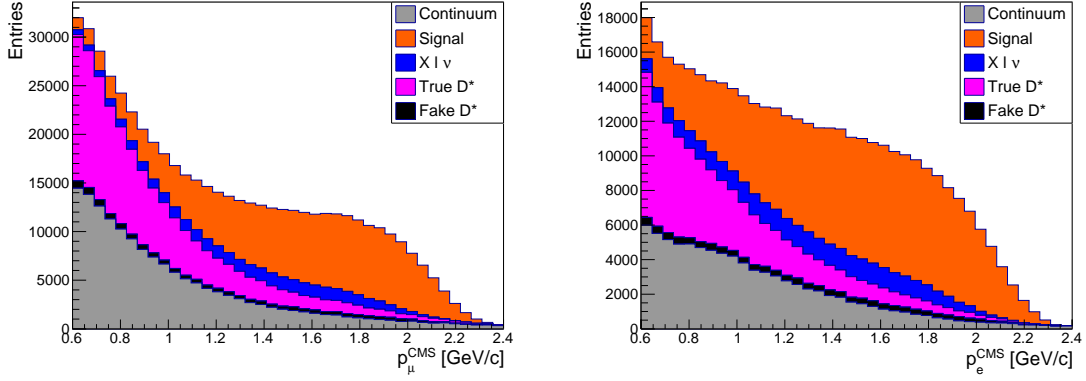


Figure 4.7: Distributions of the p_ℓ^{CMS} for the muon (left) and electron (right) channel. The histograms are stacked.

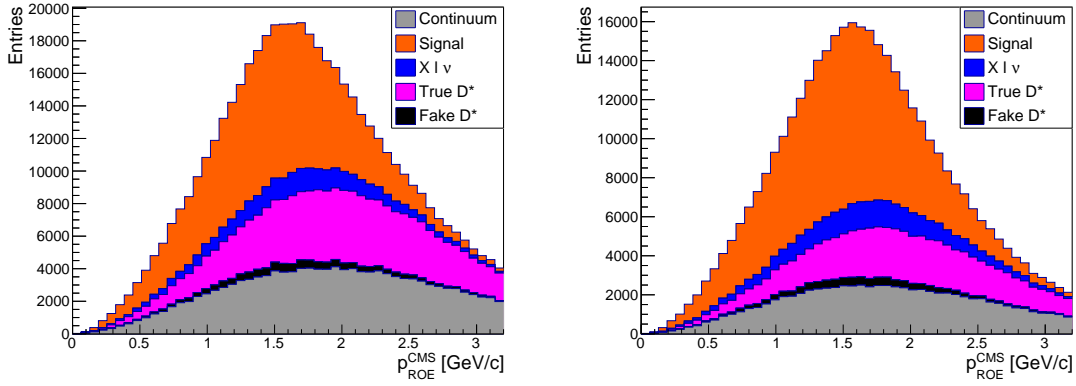


Figure 4.8: Distributions of the $p_{\text{ROE}}^{\text{CMS}}$ for the muon (left) and electron (right) channel. The histograms are stacked.

4.2.3 Final sample composition

The signal efficiencies for the electron and muon channels after all the selections are

$$\epsilon(\mu) = (12.92 \pm 0.03) \%, \quad (4.7)$$

$$\epsilon(e) = (11.64 \pm 0.03) \%. \quad (4.8)$$

The relative fraction of each component is reported in Tab. 4.4. Overall, I have improved the purity of the sample, from about 10% after skimming selections to over 80% after final selections.

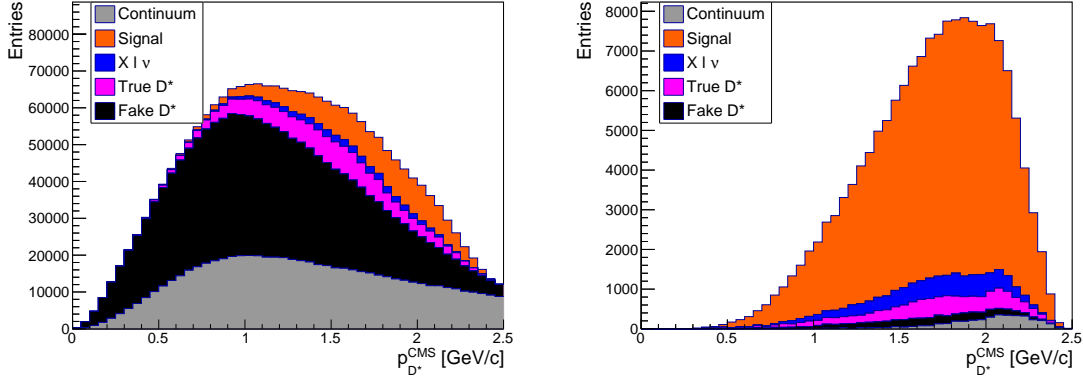


Figure 4.9: Distributions of $p_{D^*}^{\text{CMS}}$ before (left) and after (right) the application of the selected criteria of this Chapter for the muon channel. The histograms are stacked.

Component	Muon channel [%]	Electron channel [%]
Signal	81.85 ± 0.10	85.30 ± 0.10
Continuum	2.89 ± 0.04	2.34 ± 0.04
$X l \nu$	6.40 ± 0.06	6.28 ± 0.07
True- D^*	6.08 ± 0.06	3.32 ± 0.05
Fake- D^*	2.78 ± 0.04	2.86 ± 0.04

Table 4.4: Relative fractions of each component after the full selection. Uncertainties are statistical.

Figure 4.9 compares the distribution of $p_{D^*}^{\text{CMS}}$ in the two cases, visually demonstrating how the purity has improved. However, these selections significantly reduce the available statistic, since the signal efficiency is almost halved compared to the efficiency after the skimming phase. For the Run I data set, I expect (35620 ± 190) events for the muon channel and (32950 ± 180) events for the electron channel.

After skimming selections, the fraction of each component differs between the muon and the electron channels. This difference is enhanced in the true- D^* component after the full selection, while the others are similar. A detailed overview is given by Tabs. 4.5- 4.6, where I report the efficiency of the selection flow for both channels. A comparison of them quantifies how each selection affects a component in the two channels. The selections that originate significant differences are: for the fake- D^* component, the PID selection; for the continuum events, several requirements lead to a difference, with PID being the selection with highest impact; for the true- D^* component, the PID and $M(Y)$ selections are those causing the difference; for the signal, the $\cos\theta_{BY}$ selection

Selection	Signal	Continuum	$X\ell\nu_\ell$	True- D^*	Fake D^*
$\Delta M(D^*, D^0)$	98.76	22.53	98.67	97.45	2.83
$M(D^0)$	93.12	85.68	93.11	91.64	43.44
PID(μ)	96.56	72.09	95.38	72.10	84.84
$\cos TBT O$	83.25	51.11	83.01	77.95	80.39
$\cos \theta_{BY}$	93.81	15.06	44.36	24.78	56.69
$M(Y)$	94.63	77.83	95.65	63.51	89.89
p_μ^{CMS}	97.87	71.85	96.84	89.90	97.83
$p_{D^*}^{\text{CMS}}$	100.00	92.61	100.00	100.00	99.98
$p_{\text{ROE}}^{\text{CMS}}$	97.73	85.28	95.52	87.27	96.80

Table 4.5: Selection-flow table with relative efficiencies in % for the muon channel for each component. The value of a row refers to the efficiency of that requirement with respect to the sample obtained by applying all requirements of the preceding rows. The first selection ($\Delta M(D^*, D^0)$) is evaluated with respect to the skimming selection events.

Selection	Signal	Continuum	$X\ell\nu_\ell$	True- D^*	Fake- D^*
$\Delta M(D^*, D^0)$	98.70	27.39	98.80	96.86	3.02
$M(D^0)$	93.10	86.38	93.12	90.84	45.60
PID(e)	97.56	82.29	97.18	84.77	92.75
$\cos TBT O$	82.47	52.14	81.82	77.66	79.83
$\cos \theta_{BY}$	88.17	14.70	38.71	20.75	57.25
$M(Y)$	93.09	86.12	94.46	52.90	89.09
p_e^{CMS}	96.39	72.72	94.82	89.89	96.32
$p_{D^*}^{\text{CMS}}$	100.00	97.02	100.00	100.00	100.00
$p_{\text{ROE}}^{\text{CMS}}$	97.66	88.23	95.54	88.82	97.21

Table 4.6: Selection-flow table with relative efficiencies in % for the electron channel for each component. The value of a row refers to the efficiency of that requirement with respect to the sample obtained by applying all requirements of the preceding rows. The first selection ($\Delta M(D^*, D^0)$) is evaluated with respect to the skimming selection events.

removes more electron events; this also causes the difference in the $X\ell\nu$ component.

4.3 Monte Carlo validation

The selection is obtained through the study of the Monte Carlo sample, which is an helpful tool in understanding the data composition and background features. As presented in Sec. 4.1.1, the division of the data sample into five components is possible thanks to the knowledge of all information regarding the selected decay, accessible only through the use of the simulation. Different

components have different distribution shapes that allow for the study presented in Sec. 4.2.2, which is a key aspect of this work. An high purity sample reduces the impact of uncertainties caused by the presence of background.

However, simulation must correctly resemble the experimental data. Thus, it is important to verify this condition. I inspect the distributions of various observables, such as particle momenta or invariant masses, and compare the Monte Carlo sample with the experimental data sample. The selection defined above is applied in this study, as I am interested in understanding if the selected sample is well represented in simulation for the studies presented in the rest of this thesis. In this respect, I investigate the center-of-mass momenta of all particles participating in the decay, which are shown in Appendix B, and invariant masses of reconstructed D^* , D^0 and $\Delta M(D^*, D^0)$, shown in Fig. 4.10. The simulation is scaled to the data luminosity in all these plots. Overall, there is a good agreement between data and MC, meaning that the simulation correctly reproduces the data.

The invariant masses of the D^* and D^0 mesons and $\Delta M(D^*, D^0)$ are inspected without the requirements imposed on these variables to observe regions enriched in background, called *sidebands* (Fig. 4.10). The sidebands are defined with these requirements: $M(D^*) < 1.97 \text{ GeV}/c^2$ and $M(D^*) > 2.04 \text{ GeV}/c^2$, since the mass of D^* is not a selection variable. They are particularly interesting to study: they are composed principally by fake- D^* and marginally by continuum events, thus allowing to individuate these background sources in the experimental data sample. Simulation predicts fairly well the amount of background in these regions. I also compare the distributions of some variables ($\cos\theta_{BY}$, p_ℓ^{CMS} , $p_{D^*}^{\text{CMS}}$ and $p_{\pi_s}^{\text{CMS}}$) for data and simulation in the sidebands. I observe reasonable agreement between data and MC in both the shape and the normalization for these distributions, as shown in Figs. B.4- B.5 in Appendix B. This fact will be useful to constraint fake- D^* and continuum background in the fit for the sample composition, that will be discussed in the next Chapter.

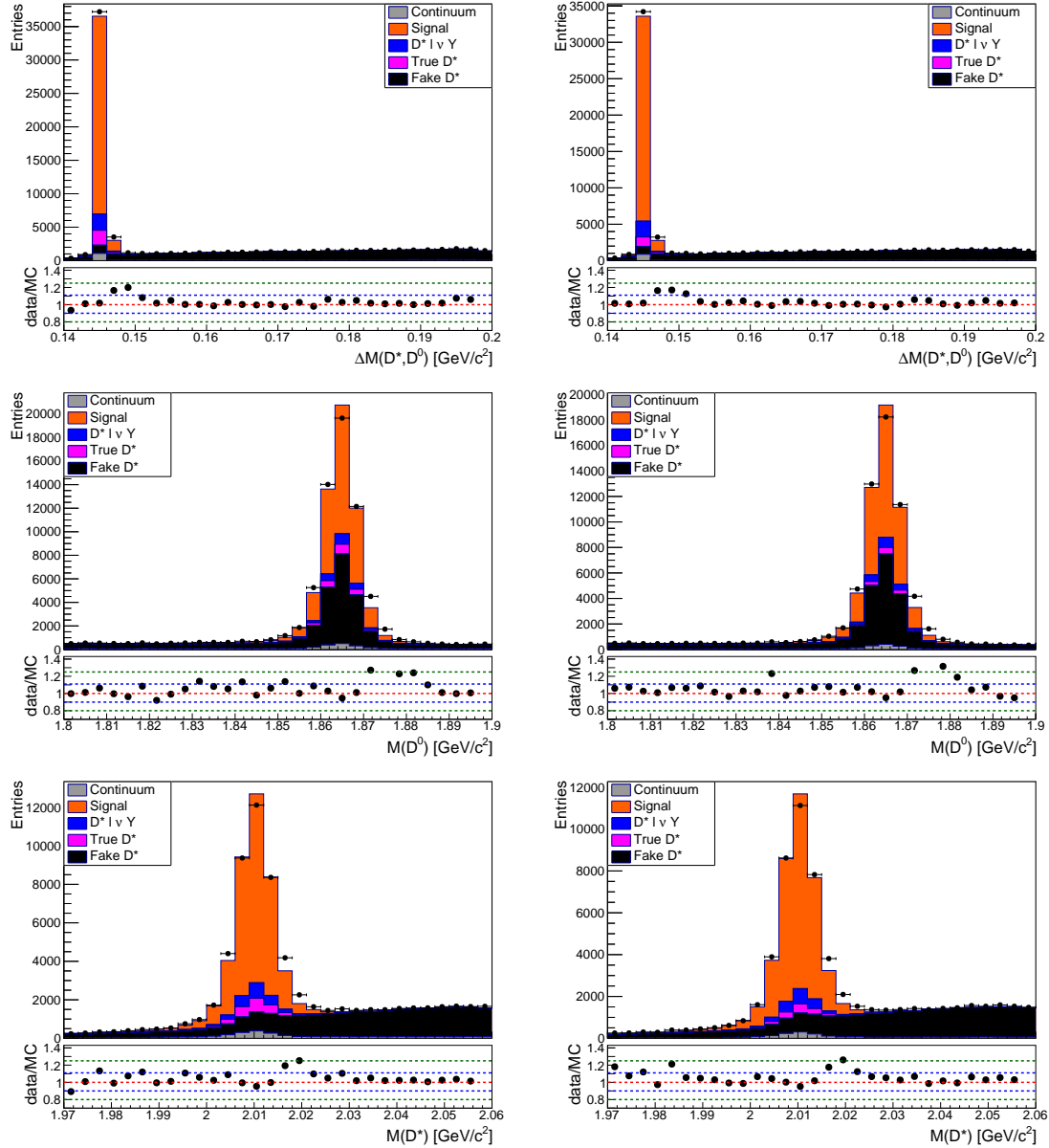


Figure 4.10: Data-simulation comparison for the distributions of $\Delta M(D^*, D^0)$ and invariant masses of D^* and D^0 mesons. Differences observed in the proximity of the peaks are likely due to a different mass resolution between data and simulation. The histograms are stacked.

Chapter 5

Fit of sample composition

In this Chapter I inspect the analysis variables that are used to access the two- and three-dimensional decay rates of the signal. Then I discuss the settings of the sample composition fit to measure the signal branching fraction, as a preliminary step before extending the fit to include model-independent observables a'_n , b'_n and c'_n . Lastly, I use pseudo-experiment data to find the fit configuration that gives the smallest biases in the estimation of the fit parameters.

5.1 Accessing the differential decay rate

In Section 2.2 I presented the four kinematic variables that describe the differential decay rate of the signal decay (see Eq. 2.3). Those variables¹ are defined in the B rest frame. To reconstruct them, one needs to know the B momentum, hence, to use B -tagging algorithms, which have very low efficiency (typically below 1%).

Untagged analysis can also approximate the kinematics of the decay by using the information of the rest-of-event in an inclusive way, *e.g.* estimating the other B momentum by the sum of the other visible particles in the events other than those of the signal. This process is very efficient, although it provides lower resolution on the measurement of the B -kinematics variables. Untagged analysis of $B \rightarrow D^* \ell \nu_\ell$ decays have so far exploited this method [42]. In this case, the measurement must rely on a good description of the rest-of-event particles to properly compute resolutions and

¹I refer to them also with the shorthand B -kinematics variables.

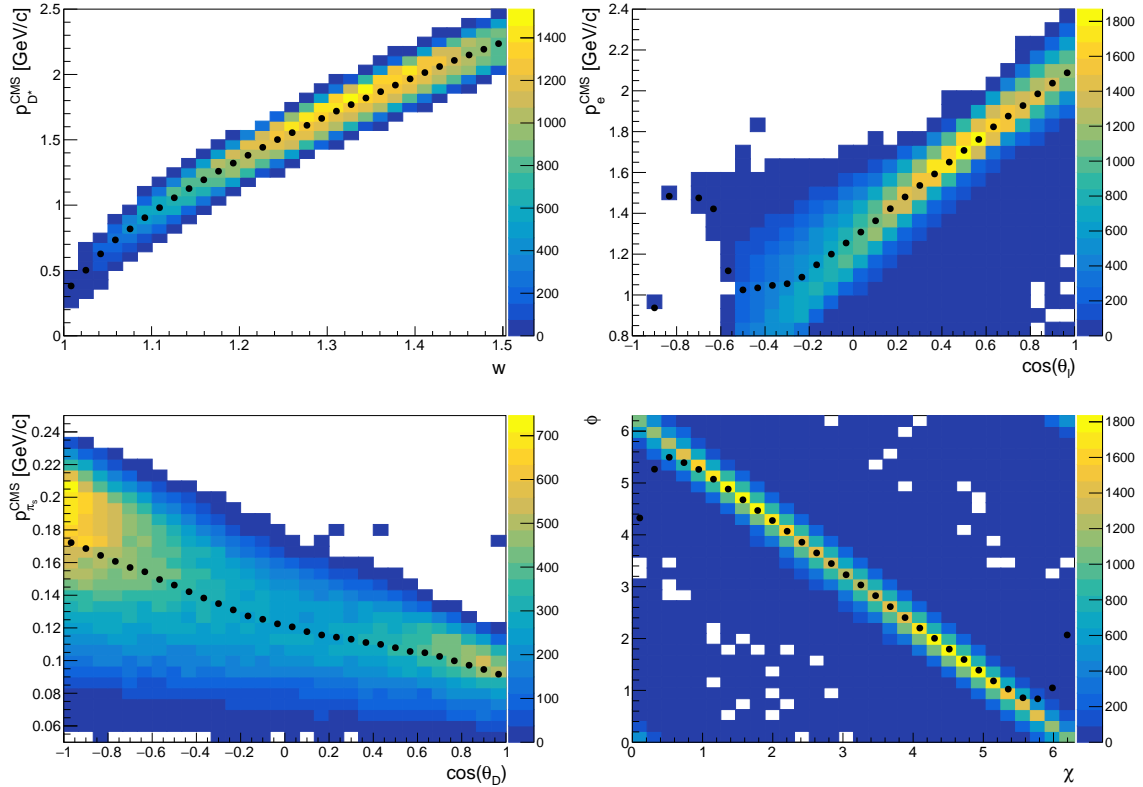


Figure 5.1: Two-dimensional distributions of (top-left) w and $p_{D^*}^{\text{CMS}}$, (top-right) $\cos\theta_{\ell}$ and p_{ℓ}^{CMS} , (bottom-left) $\cos\theta_D$ and $p_{\pi_s}^{\text{CMS}}$, (bottom-right) χ and ϕ . Simulated data of the electron channel are shown. Distributions of the muon channel present identical behaviours. The black points represent the mean value of the Y axis variable in each of the bin of the X axis variable.

efficiencies through migration matrices that are used to unfold experimental effects from the data.

Another possibility, which I investigate in my work, is the use of reconstructed variables from visible particles of the signal decays that are highly correlated with the kinematic variables of interest. In Fig. 5.1 I show the two-dimensional distribution obtained between the following pairs of variables: $(w, p_{D^*}^{\text{CMS}})$, $(\cos\theta_{\ell}, p_{\ell}^{\text{CMS}})$, $(\cos\theta_D, p_{\pi_s}^{\text{CMS}})$ and (χ, ϕ) . I show the case of the electron channel, but identical distributions hold for the muon channel.

The particle momenta in the center-of-mass frame, $p_{D^*}^{\text{CMS}}$, p_{ℓ}^{CMS} , $p_{\pi_s}^{\text{CMS}}$, and the angle ϕ are calculated from *reconstructed* particles, while the B -kinematics variables from *true* particles, both obtained in the simulation (see Sec. 4.1). The angle ϕ is a new variable introduced to find a proxy for the angle χ , and it is defined as the dihedral angle between the plane containing the lepton

Variable pair	Correlation (μ)	Correlation (e)
$(w, p_{D^*}^{\text{CMS}})$	0.97	0.97
$(\cos \theta_\ell, p_\ell^{\text{CMS}})$	0.95	0.93
$(\cos \theta_D, p_{\pi_s}^{\text{CMS}})$	-0.66	-0.66
(χ, ϕ)	-0.84	-0.84

Table 5.1: Linear correlation factors between B -kinematics variables and reconstructed variables in the muon and electron channels.

and D^* momenta and the plane containing the π_s and D^0 momenta, all calculated in the center-of-mass frame. In Tab. 5.1 I report the correlation factors of the four pairs of variables: the first two, $(w, p_{D^*}^{\text{CMS}})$ and $(\cos \theta_\ell, p_\ell^{\text{CMS}})$, show very high correlations; the $(\cos \theta_D, p_{\pi_s}^{\text{CMS}})$ pair is mildly anti-correlated; the latter pair, (χ, ϕ) , is very interesting, since, neglecting events near 0 and 2π , shows high anti-correlation.

These distributions prove that one can access the differential decay rate as a function of the B -kinematics variables through the use of reconstructed variables in the center-of-mass frame. Some dilution of the precision is present, as correlations are not 100%; however, this can be compensated by large size samples.

I use these variables to study measurements of the model-independent observables a'_n , b'_n and c'_n introduced in Chapter 2. I investigate the use of $p_{D^*}^{\text{CMS}}$, p_ℓ^{CMS} , and $p_{\pi_s}^{\text{CMS}}$ to access the two- and three-dimensional decay rates reported in Eq. 2.15 and Eq. 2.22, respectively. I do not use the angle ϕ , but the study that I present in this and in the next Chapter can be extended to access the decay rate of Eq. 2.24 and have sensitivity to the signs of the H_\pm helicity amplitudes.

5.2 Fit of sample composition

The scope of this analysis is to measure the branching fraction of the $B^0 \rightarrow D^{*-} \ell^+ \nu_\ell$ decay, and determine $|V_{cb}|$ and the form factors. I study the feasibility of doing these measurements using the proxy variables described in the previous Section to access the differential decay rates. As a preliminary step, I focus on the measurement of the branching fraction, assuming a fixed model of the form factors (which determines the shape of signal distributions) from previous measurements. In the next Chapter I release this assumption and extend the measurement to the model-independent variables a'_n , b'_n and c'_n , from which $|V_{cb}|$ and the form factors can be obtained. In my studies I

only use simulated data.

The core of this measurement is a multivariate fit. It is based on the method of least squares and minimizes the χ^2_{total} function, which is defined as the sum of the χ^2 of electron and muon samples, evaluated individually for each bin of the data histogram accordingly to the following formula:

$$\chi^2 = \sum_i \frac{[N_i - f_i(\bar{\theta})]^2}{\sigma_i^2}, \quad (5.1)$$

where N_i is the number of events in the i -th bin; $f_i(\bar{\theta})$ is the fitting function; and σ_i^2 is the uncertainty squared of the i -th bin, assumed to be the Poisson uncertainty of the number of events in the bin. For the χ^2 minimization, I use the MINUIT package implemented in the ROOT library.

The function $f_i(\bar{\theta})$ depends on the vector of parameters $\bar{\theta}$ and it is calculated for each i -th bin as:

$$f_i(\bar{\theta}) = N_{\text{sig}} p_i^{\text{sig}} + N_{\text{fake}} p_i^{\text{fake}} + N_{\text{true}} p_i^{\text{true}} + N_{\text{cont}} p_i^{\text{cont}} + N_{X\ell\nu} p_i^{X\ell\nu}, \quad (5.2)$$

where N_j is the total number of events of the sample component j (the *yield*), while the probability density functions p_i^j (pdfs), evaluated in each i -th bin, resembles the distributions of the component j . The pdf is a three-dimensional histogram of each component normalized to unity, called *template*. The component index j takes the following values: “sig” for the signal; “fake” for the fake- D^* background component; “true” for that of true- D^* background; “cont” for continuum; “ $X\ell\nu$ ” for $X\ell\nu$ background.

In Sec. 4.3 I observed a good agreement between true data and the Monte Carlo sample for fake- D^* and continuum background in the sideband distributions. Once the continuum yield is known, that of the fake- D^* background can be determined by the sideband data. The yield of the continuum can be easily obtained by the off-resonance sample, where only $e^+e^- \rightarrow u\bar{u}, d\bar{d}, c\bar{c}, s\bar{s}$ and $c\bar{c}$ events contribute, by scaling the sample size of the off-resonance sample to that of the $\Upsilon(4S)$ sample. Thus, the yield of the fake- D^* and continuum background can be fixed in the fit (this implies an additional systematic uncertainty which is not evaluated in this work). For simplicity I sum the yields and the pdfs of those two components in the fitting function and assume a single pdf from the simulation prediction.

Fixed parameters	Muon channel	Electron channel
N_{BB}		330×10^6
$(N_{\text{fake}} + N_{\text{cont}})$	5160	4150
ϵ [%]	12.9	11.6
f_{00}		0.486
$\mathcal{B}(D^* \rightarrow D^0 \pi_s)$ [%]		67.70
$\mathcal{B}(D^0 \rightarrow K\pi)$ [%]		3.95

Table 5.2: Values of the fixed parameters in the fit.

The signal yield is parameterized as:

$$N_{\text{sig}} = 2 N_{BB} \epsilon f_{00} \mathcal{B}(B \rightarrow D^* \ell \nu_\ell) \mathcal{B}(D^* \rightarrow D^0 \pi_s) \mathcal{B}(D^0 \rightarrow K\pi), \quad (5.3)$$

where N_{BB} is the number of $B\bar{B}$ pairs; ϵ is the efficiency of the electron and muon sample after the selection presented in the last Chapter; f_{00} is the fraction of $\Upsilon(4S)$ resonances that decay into $B^0\bar{B}^0$. The other factors are the branching fractions of the signal decay chain. The values of the fixed parameters are reported in Tab. 5.2: N_{BB} and $(N_{\text{fake}} + N_{\text{cont}})$ values are referred to an integrated luminosity of 1444 fb^{-1} (that of the simulated sample); efficiencies are those calculated in Sec. 4.2.3, while the other values are taken from Ref. [16].

The free parameters in the fit are the yields of $X\ell\nu$ and true- D^* components (for both the muon and electron channels) and the branching fraction of the $B \rightarrow D^*\ell\nu_\ell$ decay (common to the two samples), for a total of five free parameters.

In the next Section I present the generation and fit of pseudo-experiments to evaluate the fit properties, *i.e.*, to assess if the parameters are determined without biases. This is done for different fit configurations and it is an important preliminary step before extending the fit to the model-independent observables presented in the next Chapter.

5.3 Assessing best fit configurations

The fit can show statistical bias on the set of estimated parameters. To assess the presence of this phenomenon, I study distributions of pull values with simulated data. A pull of a parameter i is defined as the difference between the fitted value $\hat{\theta}_i$ and the true value θ_i and divided by its

estimated uncertainty $\hat{\sigma}_{\hat{\theta}_i}$:

$$\text{Pull}(\hat{\theta}_i) = \frac{\hat{\theta}_i - \theta_i}{\hat{\sigma}_{\hat{\theta}_i}}. \quad (5.4)$$

Those considered are the five free parameters of the pdf presented in the previous Section. The true values of the four background yields are the number of expected candidates found in the previous Chapter and for the $\mathcal{B}(B \rightarrow D^* \ell \nu_\ell)$ the generation value used in the Belle II simulation.

To check the pull distributions, I generate pseudo-experiments. A pseudo-experiment resembles a data sample: the number of event generated for each component is obtained from a Poisson distribution centered at the value expected from the simulation (the only exception being fake- D^* and continuum components, that are fixed in the fit). An event is generated by randomly extracting variable values from the templates of the chosen component. The pseudo-experiment total sample is composed by putting together the generated events of all components.

I generate and fit 1000 pseudo-experiments. For each fit, I obtain the values of fit parameters and its uncertainties to compute the pulls. The obtained pulls form a distribution, which is then fitted with a Gauss function. The results are unbiased if the pulls follow a Gaussian distribution with zero mean and unit standard deviation. If the mean differs from zero, it indicates that there is a systematic bias in the estimation of the parameter; if the standard deviation differs from unity, it corresponds to a wrong estimation of the parameter uncertainty.

5.3.1 Tested configurations

In this study I make use of three-dimensional histograms, which are filled by triplet of those variables correlated to the B -kinematics variables (as discussed in Sect. 5.1). I tested two configurations of fitting variables in my study:

- Configuration A: $(\cos \theta_{BY}, p_\ell^{\text{CMS}}, p_{D^*}^{\text{CMS}})$, which gives access the two-dimensional decay rate of Eq. 2.15.
- Configuration B: $(p_{\pi_s}^{\text{CMS}}, p_\ell^{\text{CMS}}, p_{D^*}^{\text{CMS}})$, which gives access the three-dimensional decay rate of Eq. 2.22.

The variable $p_{D^*}^{\text{CMS}}$ is highly correlated to w , while p_ℓ^{CMS} with $\cos \theta_\ell$ (Tab. 5.1). The variable $p_{\pi_s}^{\text{CMS}}$ is correlated to $\cos \theta_D$, while the cosine of the angle between the momenta of B meson and the Y system, $\cos \theta_{BY}$, has much less dependence on the the form factors, but helpful in discriminating

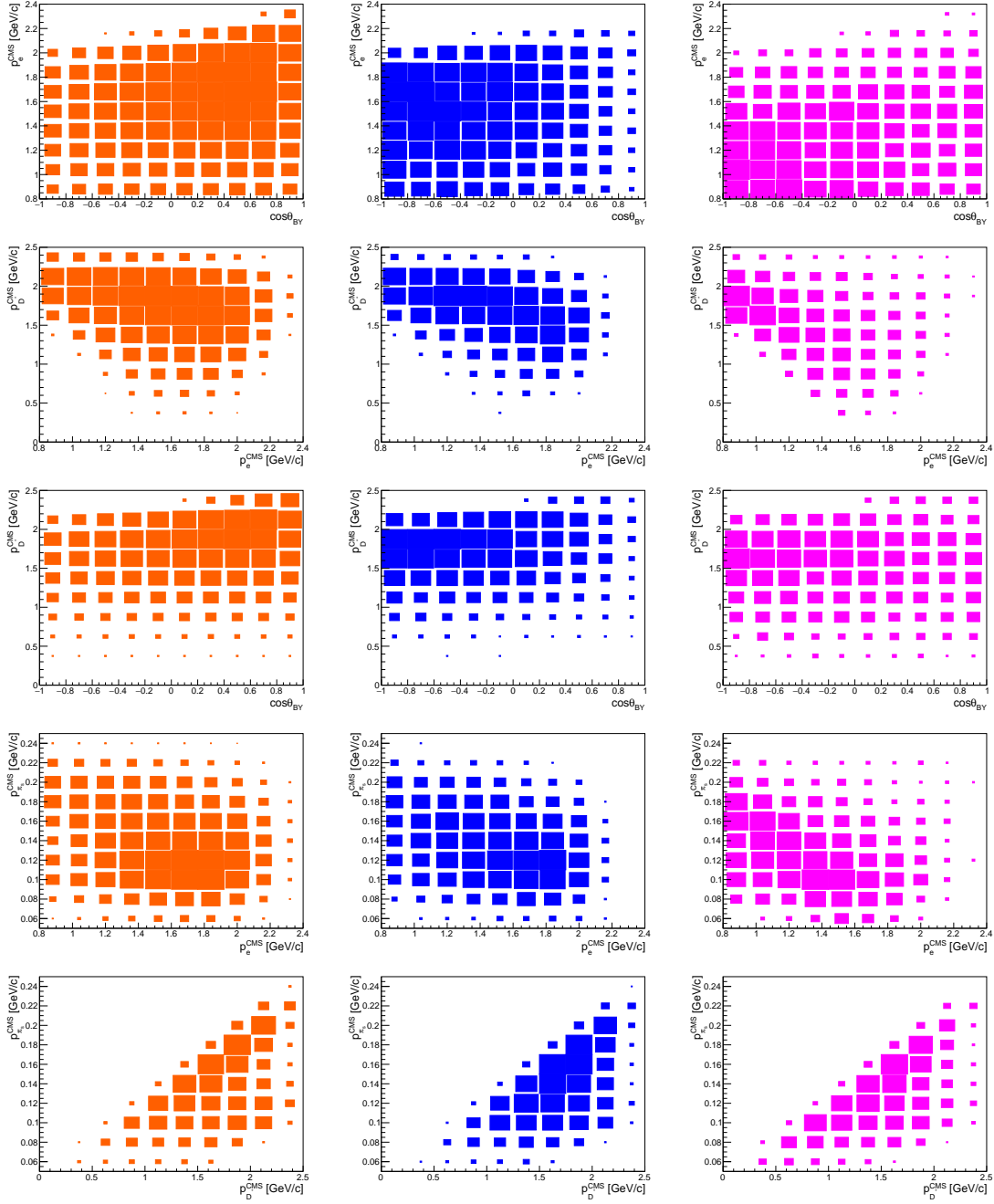


Figure 5.2: Two-dimensional distributions of configuration A and B variables for the electron channel: $(\cos\theta_{BY}, p_e^{\text{CMS}})$ in the first row, $(p_l^{\text{CMS}}, p_{D^*}^{\text{CMS}})$ in the second row, $(\cos\theta_{BY}, p_{D^*}^{\text{CMS}})$ in the third row, $(p_l^{\text{CMS}}, p_{\pi_s}^{\text{CMS}})$ in the fourth row, $(p_{D^*}^{\text{CMS}}, p_{\pi_s}^{\text{CMS}})$ in the fifth row. In orange the signal component, in blue the $X\ell\nu$ component, in purple the true- D^* component.

between background components. This is shown by the two-dimensional distributions of Fig. 5.2, where the distributions for the signal, $X\ell\nu$, and true- D^* components are reported. The separation of the components is noticeable by looking at the dimensions of boxes, which is proportional to the number of events per bin; the signal component events accumulates more in regions where $X\ell\nu$ and true- D^* are not. All pairs present this behaviour at different level, indicating that they can statistically discriminate the sample components.

Configuration A is expected to provide the best separation between the signal and background components, and it is the same configuration used in the ongoing analysis in Trieste with $B \rightarrow D\ell\nu_\ell$ and partially reconstructed $B \rightarrow D^*\ell\nu_\ell$ decays [52]. Therefore, I start from configuration A to inspect any bias as a function of the sample size expressed in terms of the integrated luminosity. For each configuration three scenarios of integrated luminosity are tested: 360 fb^{-1} , 700 fb^{-1} and 3000 fb^{-1} . The first value is the integrated luminosity of the $\Upsilon(4S)$ Run I Belle II dataset; the second is the integrated luminosity of Belle, which Belle II expect to reach next year; the last is the expected integrated luminosity that Belle II expected in Run II, *i.e.* in about three years.

The fit projections for one of these pseudo-experiments are shown in Fig. 5.3 as an example for the third scenario. The pulls distributions for the fit in the three scenarios are shown in the Figs. C.1-C.2- C.3 of Appendix C. A summary plot of the means and standard deviations of parameter pulls is reported in Fig. 5.4. The estimated parameters show little biases that get smaller in the scenario with 3000 fb^{-1} . The biases in the other two scenarios are not severe, and they might depends also on other fit settings as the binning scheme used for the data (this is discussed later). However, to fix an unbiased scenario to proceed with further studies, we choose to simulate 3000 fb^{-1} samples in what follows.

It is important to notice that, in the χ^2 fit I skip data bins that have less than 30 number of events, to prevent calculating the χ^2 with insufficient events to assume a Gaussian distribution (an assumption intrinsic of the χ^2 fit). It is key to find an adequate binning scheme which minimizes the number of bins with insufficient events, but it is also important to consider a sufficient number of bins to keep information on the distribution shape and discriminate between sample components. I test the two configurations with different binning schemes, *i.e.* varying the number of bins and/or using non-uniform bin widths. To select the optimal setting for each configuration, I inspect pull distributions and the presence of biases.

For configuration A, events are spread almost evenly among the space, leaving small regions

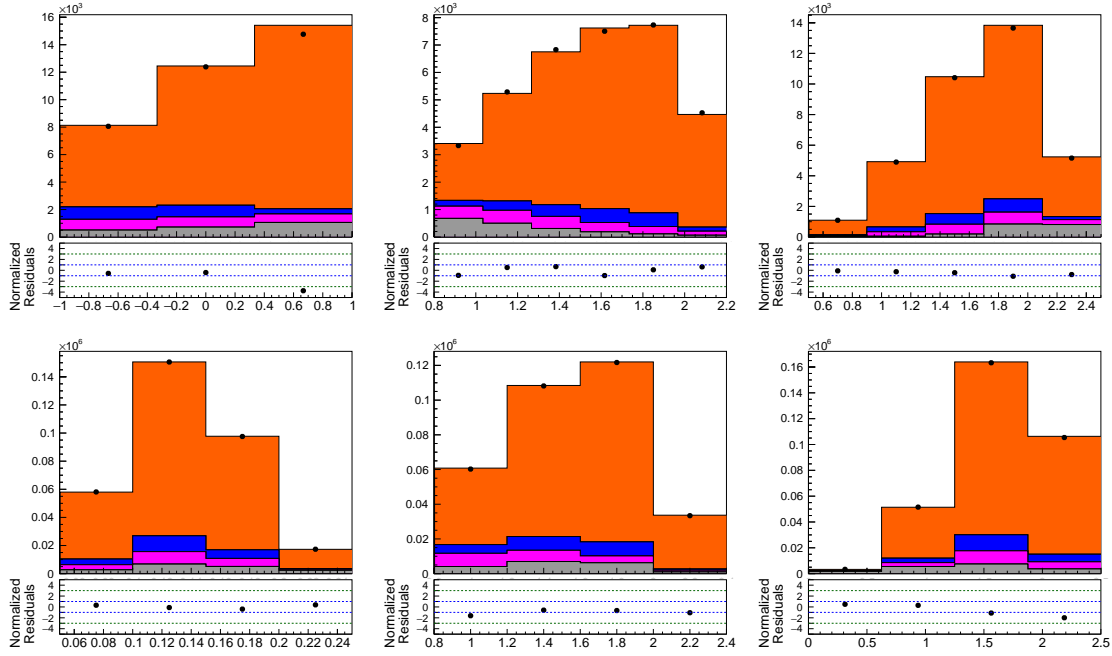


Figure 5.3: Projection distributions of a pseudo-experiment of configuration A (top row) and B (bottom row) for the muon channel. The distribution variables are (from left to right): $\cos \theta_{BY}$, p_ℓ^{CMS} , and $p_{D^*}^{\text{CMS}}$ (in GeV/c) for the first row; p_{π_s} , p_ℓ^{CMS} , and $p_{D^*}^{\text{CMS}}$ (in GeV/c) for the second row. The histogram components are stacked: signal (in orange), $Xl\nu$ (in blue), true- D^* (in purple), fake- D^* (in black) and continuum (in grey); black markers are data points (uncertainty is not visible). Under the stacked histogram are shown the normalized residuals for each bin.

with insufficient events. This fact allows to study directly settings with uniform bin widths. As for configuration B, the distributions show regions in space sparsely populated: several bins might not have enough events. I compare two schemes: one with uniform bin width, the other with an evenly-distributed number of events among the bins. By running the pseudo-experiments and inspecting the pull distributions, I find no significant difference between the two schemes. Therefore I proceed considering the simpler case with uniform bin width. In Tab. 5.3 is reported a summary of the final settings for the configurations A and B, that will be used in the next Chapter to extend the fit to measure the model-independent observables a'_n , b'_n , and c'_n . For both configurations, the fraction of skipped bins in the chosen settings is no more than 30%.

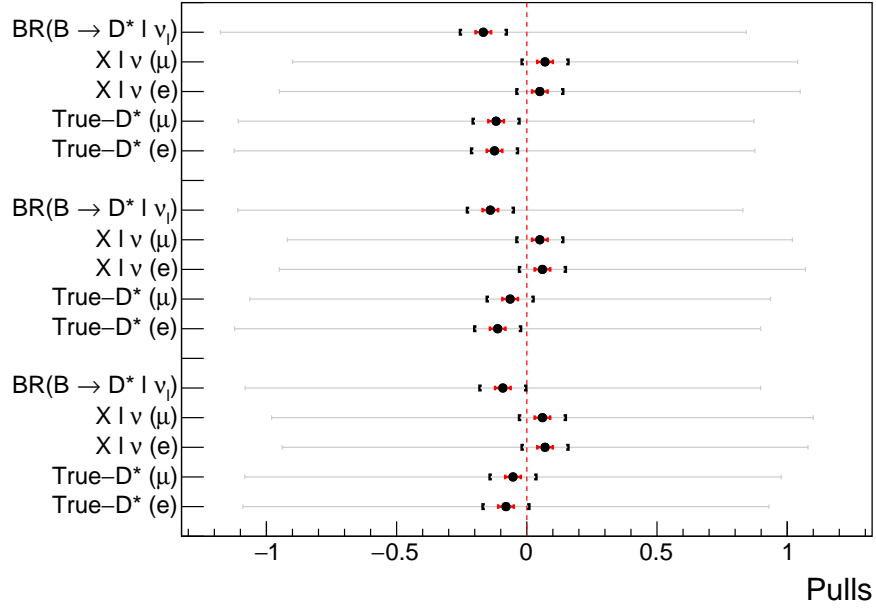


Figure 5.4: Summary plot of the mean value and standard deviation of the free parameters of the fit. The three tested integrated luminosity results are grouped: 360 fb^{-1} (top), 700 fb^{-1} (middle) and 3000 fb^{-1} (bottom). In grey are shown the standard deviation bars, which are all consistent with 1; black dots indicate the mean value obtained from the Gaussian fit; red and black ranges indicate, respectively, σ and 3σ of the mean uncertainties obtained from the Gaussian fit.

Configuration A	$\cos \theta_{BY}$	p_ℓ^{CMS}	$p_{D^*}^{\text{CMS}}$
Variable range	$[-1, 1]$	$[0.8, 2.4] \text{ [GeV/c]}$	$[0, 2.5] \text{ [GeV/c]}$
Number of bins	3	5	4
Fraction of skipped bins [%]		24	

Configuration B	$p_{\pi_s}^{\text{CMS}}$	p_ℓ^{CMS}	$p_{D^*}^{\text{CMS}}$
Variable range	$[0.05, 0.25] \text{ [GeV/c]}$	$[0.8, 2.4] \text{ [GeV/c]}$	$[0, 2.5] \text{ [GeV/c]}$
Number of bins	4	4	4
Fraction of skipped bins [%]		28	

Table 5.3: Binning scheme for the configurations A (top) and B (bottom). Both configurations have uniform bin width. The fraction of skipped bins is the number of bins with less than 30 entries over the total number of bins; those bins are skipped in the χ^2 fit.

Chapter 6

Measurement of the model-independent observables

In this Chapter I present the fit employed to measure the model-independent observables of the signal decay. Then, I show an interpretation of these measurements to determine $|V_{cb}|$ using a model for the form factors. I compare two configurations of fit variables to assess which one provides the best sensitivity to $|V_{cb}|$ and the form factor parameters.

6.1 Fit of the model-independent observables

Once the fit of the sample composition is set, I extend it to measure the model-independent observables. To this purpose, I re-parameterize the signal pdf of Eq. 5.3 to obtain the signal yield as a function of a'_n , b'_n and c'_n , which are the free parameters of the fit adopted in this Section. Thus, I refer to this improved version as the *model-independent* fit.

I first parameterize the signal yield as a function of the model-independent observables by decomposing the signal branching fraction, which is the current fit parameter. The branching fraction of $B \rightarrow D^* \ell \nu_\ell$ decay can be obtained from the following formula:

$$\mathcal{B}(B \rightarrow D^* \ell \nu_\ell) = \frac{\Gamma(B \rightarrow D^* \ell \nu_\ell)}{\Gamma_{\text{total}}}, \quad (6.1)$$

where $\Gamma(B \rightarrow D^* \ell \nu_\ell)$ is the decay width of the selected decay and Γ_{total} is the total decay width of B mesons, which is obtained as

$$\Gamma_{\text{total}} = \frac{\hbar}{\tau_B}, \quad (6.2)$$

with τ_B the B meson lifetime ($\tau_B = 1.638 \times 10^{-12}$ s) [16] and \hbar the reduced Planck constant ($\hbar = 65.82 \times 10^{-17}$ eV \times s).

The decay width of $B \rightarrow D^* \ell \nu_\ell$ is obtained by integrating the differential decay rate: configuration A uses the two-dimensional decay rate (Eq. 2.15) that is integrated in w and $\cos \theta_\ell$,

$$\Gamma(B \rightarrow D^* \ell \nu_\ell) = \int_1^{1.50349} dw \int_{-1}^1 d\cos \theta_\ell \frac{d^2 \Gamma(B \rightarrow D^* \ell \nu_\ell)}{dw d\cos \theta_\ell}, \quad (6.3)$$

while configuration B uses the three-dimensional decay rate (Eq. 2.22) that requires the additional integration of $\cos \theta_D$,

$$\Gamma(B \rightarrow D^* \ell \nu_\ell) = \int_1^{1.50349} dw \int_{-1}^1 d\cos \theta_\ell \int_{-1}^1 d\cos \theta_D \frac{d^3 \Gamma(B \rightarrow D^* \ell \nu_\ell)}{dw d\cos \theta_\ell d\cos \theta_D}. \quad (6.4)$$

The maximum value of w is obtained at zero recoil energy ($q^2 = 0$) using the formula of Eq. 2.2 and the mass values of B and D^* mesons of Ref. [16]. The two differential decay rates are functions of the model-independent variables a'_n , b'_n and c'_n as shown in Eqs. 2.19- 2.21. Signal yield can now be expressed in terms of these variables. However, the signal template is still fixed from the simulation: it needs to be modified to be function of the model-independent observables either.

6.1.1 Signal reweighting

The template that makes the signal pdf is generated assuming a given model (BGL) for the form factors (hence, fixed values of a'_n , b'_n and c'_n). I need a way to modify the shape templates according to new values of a'_n , b'_n and c'_n , which change in the χ^2 minimization to adapt the template (and the signal yield) to the data. This is achieved through a weighting technique that happens at every call of the χ^2 in MINUIT when a scan of the parameter space is done searching for the minimum of the χ^2 function.

The weighting acts on the simulated data to change the underlying physics model used to generate the sample. Let consider as an example the fit of configuration A. The signal template must contain the information on the w and $\cos \theta_\ell$ distribution of the original model. Therefore, the

three-dimensional template in $(\cos \theta_{BY}, p_\ell^{\text{CMS}}, p_{D^*}^{\text{CMS}})$ is extended to a five-dimensional template with $(\cos \theta_{BY}, p_\ell^{\text{CMS}}, p_{D^*}^{\text{CMS}}, w, \cos \theta_\ell)$. Then, I calculate the per-bin weight by evaluating the following quantity

$$p_i = \left[\frac{1}{\Gamma_{\text{new}}} \int_{\Delta x_i} \frac{d\Gamma_{\text{new}}}{dx} dx \right] / \left[\frac{1}{\Gamma_{\text{gen}}} \int_{\Delta x_i} \frac{d\Gamma_{\text{gen}}}{dx} dx \right], \quad (6.5)$$

where Δx_i is the two-dimensional space defined by the i -th bin in $(w, \cos \theta_\ell)$ of the template histogram; $d\Gamma_j/dx$ and Γ_j are the differential decay rate and its integral over the full phase space, with $j = \text{gen}$ for the decay-model (BGL) used in the generation of the simulated data, and $j = \text{new}$ for the new decay-model with the parameters a'_n , b'_n , and c'_n to be determined in the fit.

The five-dimensional histogram, with modified entries in the $(w, \cos \theta_\ell)$ bins, is marginalized to obtain the three-dimensional template in $(\cos \theta_{BY}, p_\ell^{\text{CMS}}, p_{D^*}^{\text{CMS}})$. The shape of the three-dimensional distribution is then changed according to the new underlying physics model. Notice that this weighting method allows to account for efficiency variations as a function of the reconstructed variables and resolution effects and makes the template independent from the form factor model assumed in the data generation. A similar procedure is adopted with the configuration B, with the only difference being that I need to add another dimension for $\cos \theta_D$.

Notice that the weighting is not dependent on how much populated is the space of the B -kinematics variables in the templates, (*i.e.* the number of bins defined for the extra dimensions added to the original template of the reconstructed variables). The weight can be always computed, and if there are no events in a particular bin, the weight will not modify the (zero) content. By marginalizing the distribution to project only on the space of reconstructed variables, the weights are summed up, and for the χ^2 fit only the bin content of the histogram of the reconstructed variables matters.

I choose to split the w range in 5 bins. This choice depends on the shape of the expected w distribution and has been optimized in Ref. [52]. From the same Reference, $\cos \theta_\ell$ is defined in three bins of different widths, while I choose to split $\cos \theta_D$ in three bin as well, but with uniform bin widths. These three distributions are shown in Fig. 6.1. Since I use five w bins to evaluate the three observables, there are now 15 free parameters for the signal in the model-independent fit.

In Fig. 6.2, I show how the one-dimensional distributions of $p_{\pi_s}^{\text{CMS}}$, p_ℓ^{CMS} and $p_{D^*}^{\text{CMS}}$ change for some different values of the parameters a'_n , b'_n and c'_n .

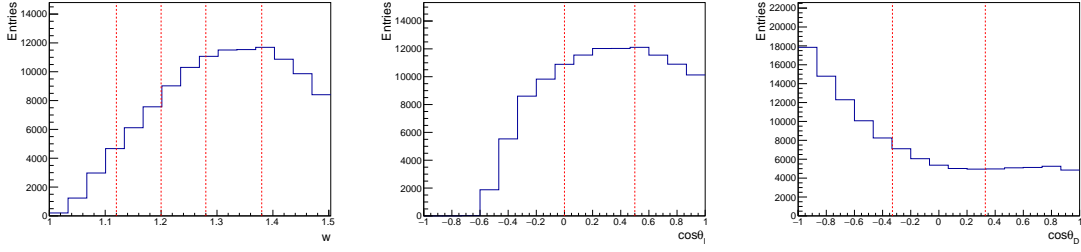


Figure 6.1: Distributions of w (left), $\cos\theta_\ell$ (middle) and $\cos\theta_D$ (right) for the electron channel. The vertical dotted red line indicates the bin edges chosen for this analysis.

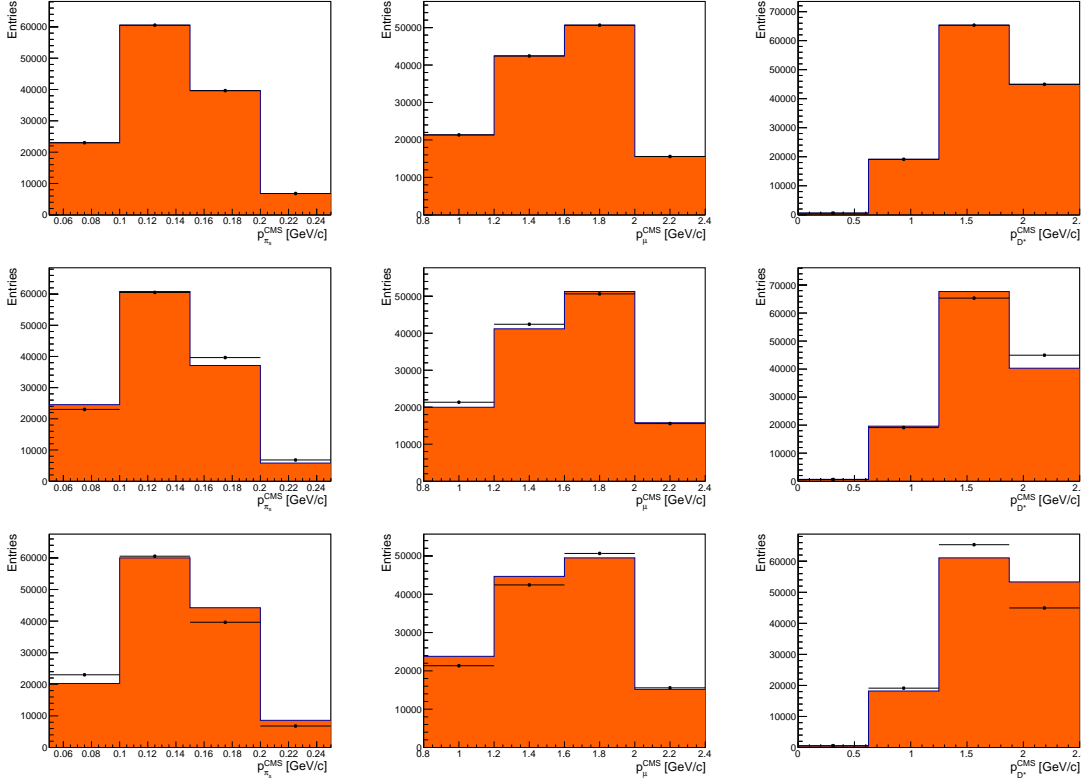


Figure 6.2: From left to right: one-dimensional distributions of $p_{\pi_s}^{\text{CMS}}$, p_ℓ^{CMS} and $p_{D^*}^{\text{CMS}}$ for the muon channel. These distributions show how the signal template changes its shape with different values of a'_n , b'_n and c'_n , compared with the generation values, indicated with black dots in each graph: in the first row, parameter values are the same as generation ones; in the second and third rows are shown different configurations of the model-independent observables.

Parameter	Value	Parameter	Value	Parameter	Value
a'_1	0.216913	b'_1	0.0838165	c'_1	-0.013205
a'_2	0.237823	b'_2	0.116515	c'_2	-0.0427276
a'_3	0.266600	b'_3	0.126478	c'_3	-0.0790286
a'_4	0.333476	b'_4	0.130480	c'_4	-0.154522
a'_5	0.703115	b'_5	0.130076	c'_5	-0.534632

Table 6.1: Generation values of the model-independent observables, which are free parameters of the fit.

6.1.2 Pseudo-experiment results

It is useful to run an analysis similar to that presented in Sec. 5.3, where I use pseudo-experiments to study possible fit biases. In this case, I also want to compare the statistical sensitivity on the parameters for the configurations A and B. At this scope, I generate and fit 1000 pseudo-experiments for each configuration. The generation of pseudo-experiments is performed identically as before, with the addition of considering the new, re-weighted template for the signal to generate a model with the parameters a'_n , b'_n and c'_n reported in Tab. 6.1. The signal template for the fit is the original template from the simulation with the BGL as the generation model.

Results of these fits are the pull distributions of the 19 free parameters (15 model-independent observables for the signal, and the same four background yields of fit in the Chapter 5), shown in the Appendix D. While most of fit parameters present no significative bias, for both configurations the parameters a'_5 and b'_4 have large biases (about 3 to 5 deviations from the mean error). For configuration A, also the yield of the true- D^* component for the muon channel has similar behaviour, while for configuration B this occurs for c'_5 . An example of fit projections are shown in Fig. 6.3 and 6.4 for configuration A and B, respectively.

Figure 6.5 shows the plots of the 15 model-independent observables for each configuration in bins of w , comparing the generation values with the mean values obtained from the 1000 pseudo-experiments (the uncertainties are averages of the fit uncertainties).

To compare the two configurations, I calculate the relative difference for the uncertainty of the model-independent observables:

$$\frac{(\sigma_A - \sigma_B)}{\sigma_A}, \quad (6.6)$$

used to highlight if there is an improvement in the measured parameter when passing from con-

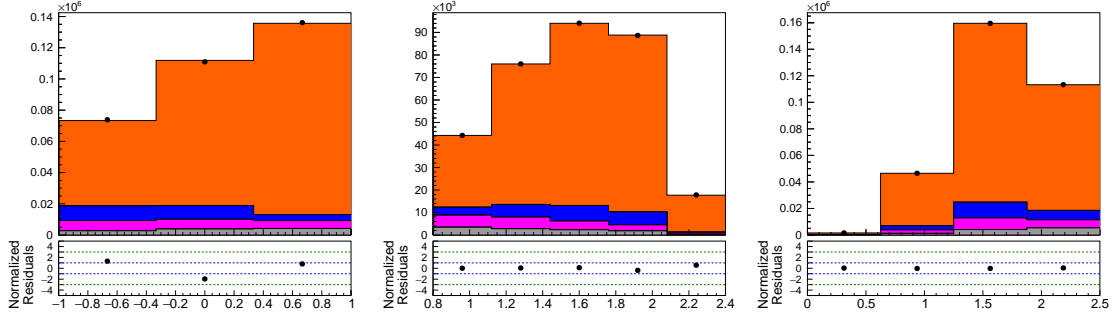


Figure 6.3: Projection distributions of a pseudo-experiment of configuration A after the model-independent fit for the muon channel. The distribution variables are (from left to right): $\cos \theta_{BY}$, p_ℓ^{CMS} , and $p_{D^*}^{\text{CMS}}$ (in GeV/c). The histogram components are stacked: signal (in orange), $X\ell\nu$ (in blue), true- D^* (in purple), fake- D^* (in black) and continuum (in grey).

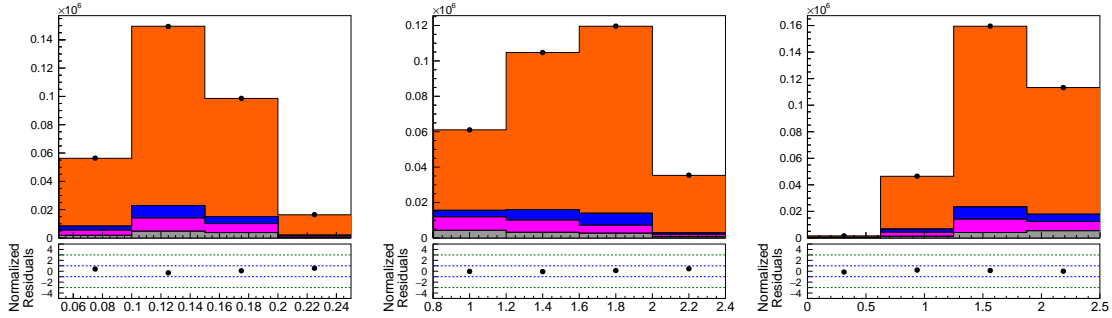


Figure 6.4: Projection distributions of a pseudo-experiment of configuration A after the model-independent fit for the muon channel. The distribution variables are (from left to right): $p_{\pi_s}^{\text{CMS}}$, p_ℓ^{CMS} , and $p_{D^*}^{\text{CMS}}$ (in GeV/c). The histogram components are stacked: signal (in orange), $X\ell\nu$ (in blue), true- D^* (in purple), fake- D^* (in black) and continuum (in grey).

figuration A, using the two-dimensional decay rate in $(w, \cos \theta_\ell)$, to configuration B, using the three-dimensional decay rate in $(w, \cos \theta_\ell, \cos \theta_D)$. Table 6.2 reports the results obtained. The uncertainties of background yields worsen in the configuration B: as noted in the fit of sample composition, the configuration B features less discriminating distributions of the sample components, diluting statistical sensitivity. On the other hand, all uncertainties of the model-independent observables improve (up to 70%) with respect to those in configuration A. It is also interesting to compare the average linear correlation factors between fit parameters in the two configurations: they are shown in Fig. 6.6. For the a'_n observables, neighboring parameters are highly anti-correlated in configuration A while configuration B strongly reduces them; the same can be applied to b'_n and c'_n .

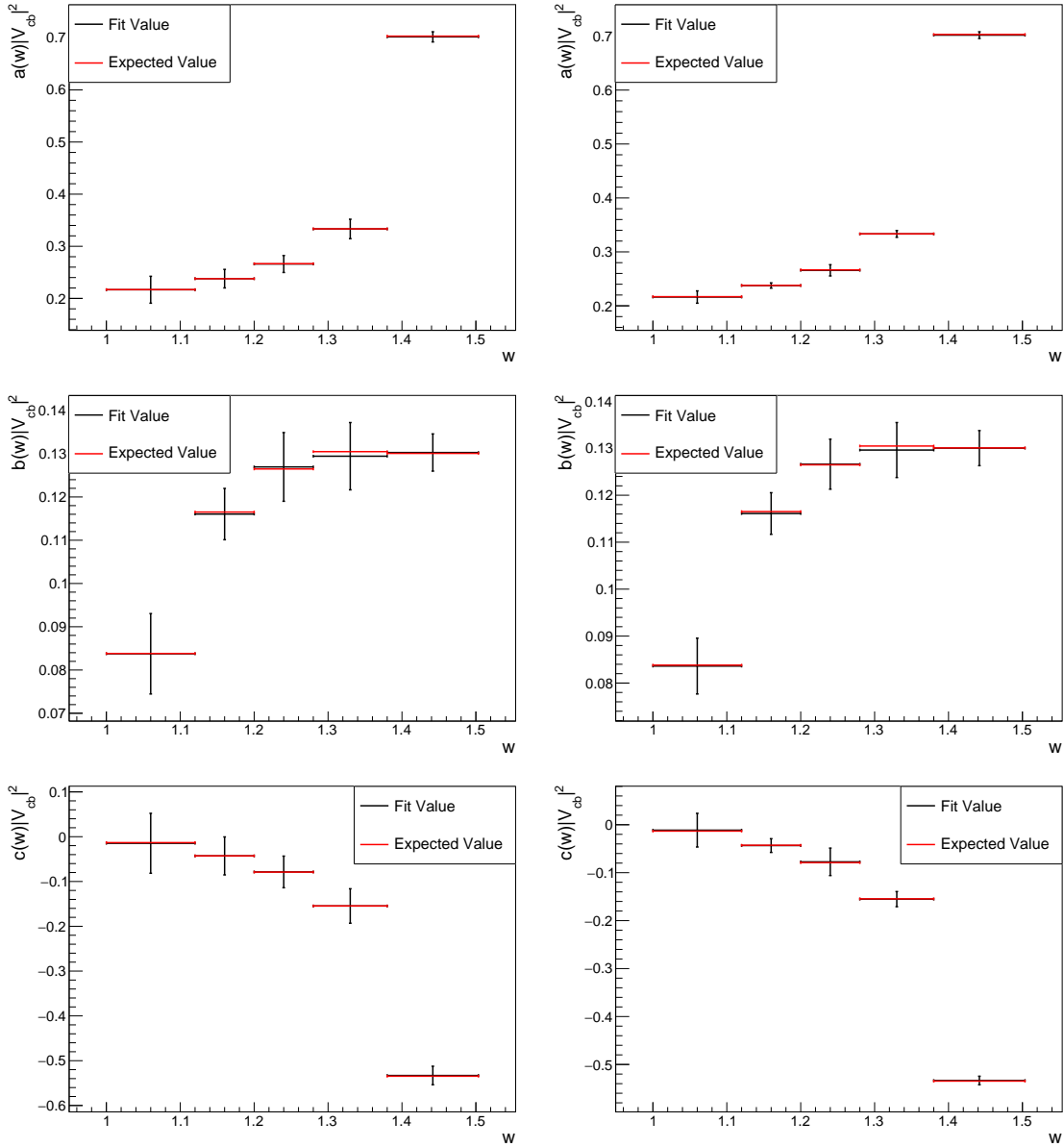


Figure 6.5: Values of model-independent observables of configuration A (left) and B (right) in bins w . Mean fit values are compared with the generated ones.

Parameter	Relative Difference [%]	Parameter	Relative Difference [%]	Parameter	Relative Difference [%]	Parameter	Relative Difference [%]
$N_{X\ell\nu}(\mu)$	-71.77	a'_1	55.80	b'_1	36.05	c'_1	47.45
$N_{\text{true}}(\mu)$	-31.94	a'_2	72.59	b'_2	25.26	c'_2	66.24
$N_{X\ell\nu}(e)$	-95.22	a'_3	36.07	b'_3	32.96	c'_3	18.83
$N_{\text{true}}(e)$	-25.29	a'_4	66.68	b'_4	24.73	c'_4	58.98
–	–	a'_5	36.26	b'_5	13.19	c'_5	56.99

Table 6.2: Relative difference of the uncertainties [in %] for the fit parameters when passing from configuration A to configuration B. N_{true} and $N_{X\ell\nu}$ are yields of the two unfixed backgrounds, defined in Sec. 5.2.

Between a'_n and c'_n of configuration A there are high (anti-)correlation indexes which are slightly reduced in configuration B. Observables b'_n have small correlations with a'_n and c'_n . In general, correlation indexes reduce their absolute values from configuration A to B.

6.2 Sensitivity to $|V_{cb}|$ and form factor parameters

The fit developed in the Sec. 6.1 allows to obtain model-independent observables in bin of w . This is a noticeable result, as it enables the interpretation of the measurement *a-posteriori* assuming any form factor parameterization (and so any theoretical advancement in this side) to obtain $|V_{cb}|$. I want now to test the sensitivity to $|V_{cb}|$ and form factor parameters, assuming a BGL model, and compare the results from the two configurations. The 1000 pseudo-experiments of the previous Section will be used for this study. The fit to determine $|V_{cb}|$ and the BGL parameters will be referred to as *a-posteriori* fit.

The χ^2 function used for this fit reads:

$$\chi^2 = \sum_{i,j}^{15} [x_i - \mu_i(\bar{\theta})] V_{ij}^{-1} [x_j - \mu_j(\bar{\theta})]^T, \quad (6.7)$$

where the sums run over all 15 observables; $x_{i(j)}$ is the model-independent fit values of the observable $i(j)$; $\mu_{i(j)}$ is its predicted value, calculated by using the BGL parameterization of the form factors; V_{ij} is the covariance between observables i and j .

The vector of free parameters $\bar{\theta}$ depends on the assumed parameterization: in this case, I truncate the BGL series expansion of $f(z)$, $g(z)$ and $\mathcal{F}_1(z)$ at the first order (see Eqs. A.1- A.3). The same number of parameters was also used in the data generation. Values of a'_n , b'_n and c'_n are

A	a'_1	a'_2	a'_3	a'_4	a'_5	b'_1	b'_2	b'_3	b'_4	b'_5	c'_1	c'_2	c'_3	c'_4	c'_5
a'_1	100.0														
a'_2	-95.7	100.0													
a'_3	34.8	-39.2	100.0												
a'_4	-8.8	13.0	-93.9	100.0											
a'_5	-12.8	10.6	73.8	-81.8	100.0										
b'_1	24.5	-20.9	4.3	0.9	-6.0	100.0									
b'_2	-20.2	17.8	-5.8	3.6	7.1	-81.5	100.0								
b'_3	-2.6	3.5	-14.8	14.3	-9.4	35.6	-43.2	100.0							
b'_4	-8.0	8.8	-6.5	6.0	-0.6	-22.3	36.1	-87.7	100.0						
b'_5	-5.4	5.7	-3.2	-1.3	-1.4	10.2	-19.9	61.2	-68.2	100.0					
c'_1	-98.6	91.9	-33.2	7.4	11.5	-19.8	14.0	5.5	3.8	6.6	100.0				
c'_2	96.9	-98.3	38.3	-11.6	-10.2	15.7	-9.8	-8.9	-3.8	-7.6	-95.5	100.0			
c'_3	-50.4	53.2	-93.1	81.0	-57.4	-2.8	2.6	34.2	-12.4	16.5	49.5	-54.6	100.0		
c'_4	15.5	-18.3	92.5	-95.7	75.7	-4.9	1.0	-32.9	12.2	-12.1	-14.8	19.0	-89.3	100.0	
c'_5	0.5	2.4	-74.9	79.4	-94.4	3.1	-6.2	21.1	-11.5	13.8	0.2	-2.5	66.0	-78.4	100.0
B	a'_1	a'_2	a'_3	a'_4	a'_5	b'_1	b'_2	b'_3	b'_4	b'_5	c'_1	c'_2	c'_3	c'_4	c'_5
a'_1	100.0														
a'_2	-72.0	100.0													
a'_3	-1.3	-1.8	100.0												
a'_4	28.1	8.2	-73.3	100.0											
a'_5	38.3	3.3	21.9	29.5	100.0										
b'_1	-25.6	25.9	7.2	-4.1	4.2	100.0									
b'_2	-3.0	8.7	-5.3	8.6	5.2	-55.2	100.0								
b'_3	-3.3	8.8	22.0	-14.3	15.2	29.2	-40.6	100.0							
b'_4	-16.8	-4.5	-14.1	-3.2	-28.3	-7.3	33.9	-76.4	100.0						
b'_5	-3.2	-12.4	3.7	-23.0	-16.3	0.1	-20.7	41.9	-42.5	100.0					
c'_1	-94.5	79.7	2.1	-19.9	-28.8	29.3	-1.8	7.2	5.3	-2.9	100.0				
c'_2	76.2	-78.9	2.6	17.0	30.2	-20.8	0.3	-6.2	-4.1	1.9	-86.4	100.0			
c'_3	8.5	6.5	-92.5	80.8	-0.9	-4.7	7.5	-14.2	2.4	-8.7	-4.1	-4.2	100.0		
c'_4	-6.4	-7.8	83.0	-76.3	0.0	5.3	-9.6	13.1	-1.5	9.9	2.5	6.6	-95.3	100.0	
c'_5	-14.8	2.3	-32.4	7.7	-71.4	-5.0	-1.8	-11.8	9.7	5.9	13.7	-18.3	30.4	-32.8	100.0

Figure 6.6: Correlation matrix of the 15 model-independent observables for configuration A (top) and B (bottom).

Parameter	Generation Value
a_0	0.0260
a_1	-0.0604
b_1	0.0171
c_1	0.0075
$ V_{cb} $	0.0387

Table 6.3: Generation values of the *a-posteriori* fit parameters.

obtained from the BGL form factor parameterization through Eqs. 2.16- 2.18).

The free parameters are a_0 , a_1 , b_1 , c_1 , and $|V_{cb}|$, and their generation values are reported in Tab 6.3. The initial terms of two coefficient series, b_0 and c_0 , are related to each other at zero recoil ($w = 1$) and fixed by the value $h_{A_1}(1) = 0.902^1$ [74] obtained from lattice QCD calculations.

6.2.1 Results

The model-independent observables from the 1000 pseudo-experiments of Sect. 6.1 are fitted individually for both configurations A and B, whose pull distributions are showed in Appendix E and in the summary plot in Fig. 6.7. Generally, form factor parameters show biases within uncertainties, while $|V_{cb}|$ has a bias of 30% in configuration A, and 15% in B: this is caused by the higher uncertainty of this parameter for configuration B. This must be furtherly inspected, as the bias may be caused by the fixed value of $h_{A_1}(1)$. To compare the two configurations, I evaluate the mean fit values and mean uncertainties of the BGL parameters and $|V_{cb}|$, which are reported in Tab. 6.4. Uncertainties of configuration B parameters are bigger than configuration A, which is unexpected: results obtained for the model-independent fit point out that the configuration B, featuring smaller uncertainties for the model-independent observables which are used in the *a-posteriori* fit, should show better sensitivity than configuration A.

The reason can be tracked down to the different correlations between the model-independent observables in the two configurations. This is tested by constructing, for each pair of model-independent observables (m, n), a covariance V_{mn} that uses uncertainties σ_m^B of the model-independent observable determined in the configuration B and linear correlation factors ρ_{mn}^A obtained in the fit of configuration A:

$$V_{mn} = \rho_{mn}^A \sigma_m^B \sigma_n^B. \quad (6.8)$$

¹The value of $h_{A_1}(1)$ is slightly different from that in Ref. [74] and tuned to that used in the Belle II simulation.

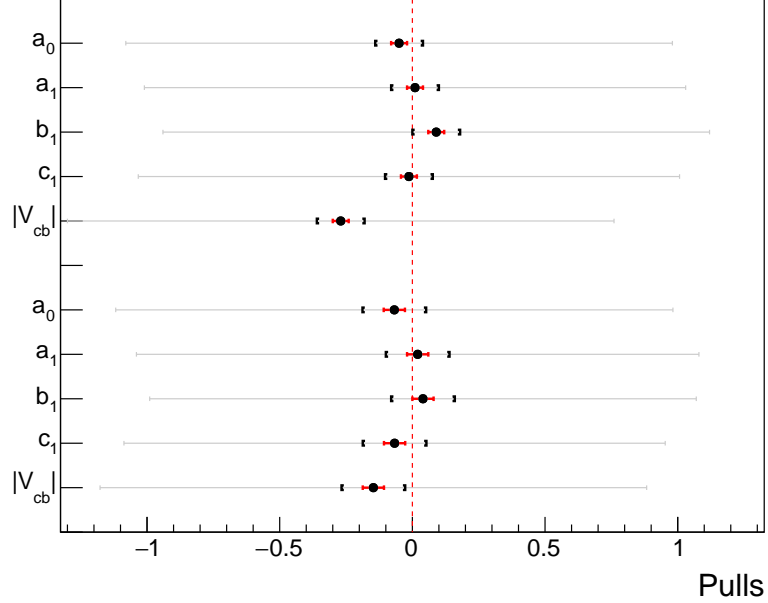


Figure 6.7: Summary plot of the mean value and standard deviation of the free parameters of the *a-posteriori* fit. The two configurations are grouped: the top group refers to configuration A while the bottom one to configuration B. In grey are shown the standard deviation bars, which are all consistent with 1; black dots indicate the mean value obtained from the Gaussian fit; red and black ranges indicate, respectively, σ and 3σ of the mean uncertainties obtained from the Gaussian fit.

The resulting values of the *a-posteriori* fit parameters are then compared with previous results from the individual configurations. Table. 6.5 reports the results of this test: the uncertainties reduce significantly respect to those obtained from configuration A. This shows that the correlations between the model-independent observables play a significant role in determining the sensitivity of the form factor parameters and $|V_{cb}|$.

6.3 Final considerations

In this Chapter I studied the model-independent fit in two configurations: both of them employ $p_{D^*}^{\text{CMS}}$ and p_ℓ^{CMS} , since they are highly correlated with B -kinematic variables; in addition, configuration A uses $\cos\theta_{BY}$, which helps to distinguish between background components; configuration B uses instead $p_{\pi_s}^{\text{CMS}}$, which allows to access the three-dimensional decay rate. Results from these fits

	Parameter	Mean Value (FIT)	Mean Error (FIT)	Relative Uncertainty [%]
A	$a_0(w)$	0.0259	0.0007	2.83
	$a_1(w)$	-0.0604	0.0206	34.06
	$b_1(w)$	0.0175	0.0039	22.46
	$c_1(w)$	0.0075	0.0002	2.48
	$ V_{cb} $	0.0387	0.0001	0.39
B	$a_1(w)$	0.0259	0.0008	3.03
	$a_1(w)$	-0.0595	0.0242	40.65
	$b_1(w)$	0.0171	0.0037	21.82
	$c_1(w)$	0.0075	0.0002	2.60
	$ V_{cb} $	0.0387	0.0002	0.48

Table 6.4: Mean values and errors of the free parameters of the *a-posteriori* fit for configurations A and B. Relative uncertainties are also reported.

	Parameter	Mean Value (FIT)	Mean Error (FIT)	Relative Uncertainty [%]
Test	$a_0(w)$	0.0275	0.0006	2.04
	$a_1(w)$	-0.1203	0.0155	12.93
	$b_1(w)$	0.0246	0.0019	7.55
	$c_1(w)$	0.0072	0.0001	1.68
	$ V_{cb} $	0.0388	0.0001	0.14

Table 6.5: Fit values of the free parameters of the *a-posteriori* fit for the test conducted. Relative uncertainties are also reported.

show small biases for some of the model-independent observables, but those are small enough that could be assessed by systematic uncertainties without spoiling the precision of the measurement and the bottom-message of this analysis. The model-independent observables offer the possibility to interpret the measurement to obtain $|V_{cb}|$ using any parameterization for the form factors.

In the model-independent fit, I observe that configuration B features smaller uncertainties for the model-independent observables (but not for the background yields) than configuration A. On the other hand, the *a-posteriori* fit, employed to determine $|V_{cb}|$, shows a better sensitivity for configuration A. This is due to the correlations between the model-independent observables: it seems that, when using proxy variables to access the B kinematics, a better signal-to-background discrimination (configuration A) is preferred over adding more information from the differential decay rate (configuration B).

Summary

The standard model is currently the best theory of elementary particles and their interactions. However, it cannot provide answers to several open questions in particle physics and cosmology and requires an extension to a more general theory, which extends to energies higher than those probed so far. The *indirect* approach offers a powerful way to search for those extensions through high-precision measurements seeking for deviations from clean, accurate standard model predictions in processes sensitive to new phenomena. The Belle II experiment, operating at the world highest luminosity electron-positron collider, is one of the main experiments to pursue the indirect approach through measurements in the weak interactions of heavy quarks. A flagship measurement of its physics program is a precise determination of the *bottom-to-charm* weak-coupling strength $|V_{cb}|$. Determinations of this coupling through two different methods have shown a long-standing inconsistency that must be resolved for the ultimate precision.

In this thesis, I focused on the exclusive measurement of $|V_{cb}|$ with the decay $B^0 \rightarrow D^{*-} \ell^+ \nu_\ell$ at Belle II. Using simulated data, I explored a novel experimental approach which provides a measurement of model-independent observables of the decay dynamics. These observables can be interpreted assuming any theoretical model to parameterize the strong interaction contribution to the decay amplitude, necessary to determine $|V_{cb}|$ from experimental data.

First, I studied a selection of the decay from Belle II data. Using a full, realistic simulation of the Belle II sample collected between 2019 and 2022, I inspected the distributions of several discriminating variables to reduce contributions from different background sources, obtaining a signal purity of 80%. I categorised the composition of the remaining background and made a comparison of simulated and experimental data as to assess the simulation quality.

Then, I inspected the kinematics variables that provide access to the decay dynamics and are

sensitive to the model-independent observables. The core of the measurement is a χ^2 fit to the binned distribution of those variables. I investigated the settings of the fit: first a simplified version to obtain the sample composition and measure the signal branching fraction; then an extension to include the model-independent observables. I used pseudo-experiment data to find the fit configuration that gives the smallest biases in the estimation of the fit parameters, simulating three scenarios for the experimental sample size and investigating two combinations of fitting variables.

Finally, I showed an interpretation of the model-independent observables to determine $|V_{cb}|$ using a specific theoretical parametrization for the description of the strong interaction contribution to the decay amplitude. I compared the two configurations of fit variables to assess which one provides the best sensitivity to $|V_{cb}|$ and the form factor parameters.

My work proves that the inspected kinematic variables offer sensitivity to the model-independent observables, such that their measurement can be pursued in Belle II data with the current sample. I showed the possibility to interpret the data with a theoretical model to obtain $|V_{cb}|$ from this measurement. I showed also that in the fit performed, for the best sensitivity on $|V_{cb}|$, a better signal-to-background discrimination is preferred over adding more information on the decay dynamics.

Bibliography

- [1] Steven Weinberg. “A Model of Leptons”. In: *Phys. Rev. Lett.* 19 (21 Nov. 1967), pp. 1264–1266. DOI: 10.1103/PhysRevLett.19.1264. URL: <https://link.aps.org/doi/10.1103/PhysRevLett.19.1264>.
- [2] Sheldon L. Glashow. “Partial-symmetries of weak interactions”. In: *Nuclear Physics* 22.4 (1961), pp. 579–588. ISSN: 0029-5582. DOI: [https://doi.org/10.1016/0029-5582\(61\)90469-2](https://doi.org/10.1016/0029-5582(61)90469-2). URL: <https://www.sciencedirect.com/science/article/pii/0029558261904692>.
- [3] Abdus Salam. “Weak and Electromagnetic Interactions”. In: *Conf. Proc. C* 680519 (1968), p. 367. DOI: 10.1142/9789812795915_0034.
- [4] Peter W. Higgs. “Broken Symmetries and the Masses of Gauge Bosons”. In: *Phys. Rev. Lett.* 13 (16 Oct. 1964), pp. 508–509. DOI: 10.1103/PhysRevLett.13.508. URL: <https://link.aps.org/doi/10.1103/PhysRevLett.13.508>.
- [5] F. Englert and R. Brout. “Broken Symmetry and the Mass of Gauge Vector Mesons”. In: *Phys. Rev. Lett.* 13 (9 Aug. 1964), pp. 321–323. DOI: 10.1103/PhysRevLett.13.321. URL: <https://link.aps.org/doi/10.1103/PhysRevLett.13.321>.
- [6] G. S. Guralnik, C. R. Hagen, and T. W. B. Kibble. “Global Conservation Laws and Massless Particles”. In: *Phys. Rev. Lett.* 13 (20 Nov. 1964), pp. 585–587. DOI: 10.1103/PhysRevLett.13.585. URL: <https://link.aps.org/doi/10.1103/PhysRevLett.13.585>.
- [7] Universität Zürich. *Standard Model*. <https://www.physik.uzh.ch/groups/serra/StandardModel.html>.

- [8] Ziro Maki, Masami Nakagawa, and Shoichi Sakata. “Remarks on the Unified Model of Elementary Particles”. In: *Progress of Theoretical Physics* 28.5 (Nov. 1962), pp. 870–880. ISSN: 0033-068X. DOI: 10.1143/PTP.28.870. eprint: <https://academic.oup.com/ptp/article-pdf/28/5/870/5258750/28-5-870.pdf>. URL: <https://doi.org/10.1143/PTP.28.870>.
- [9] Hilary Greaves and Teruji Thomas. “On the CPT theorem”. In: *Studies in History and Philosophy of Science Part B: Studies in History and Philosophy of Modern Physics* 45 (2014), pp. 46–65. ISSN: 1355-2198. DOI: <https://doi.org/10.1016/j.shpsb.2013.10.001>. URL: <https://www.sciencedirect.com/science/article/pii/S1355219813000853>.
- [10] Murray Gell-Mann and Maurice Lévy. “The axial vector current in beta decay”. In: *Il Nuovo Cimento (1955-1965)* 16.4 (1960), pp. 705–726.
- [11] Nicola Cabibbo. “Unitary Symmetry and Leptonic Decays”. In: *Phys. Rev. Lett.* 10 (12 June 1963), pp. 531–533. DOI: 10.1103/PhysRevLett.10.531. URL: <https://link.aps.org/doi/10.1103/PhysRevLett.10.531>.
- [12] S. L. Glashow, J. Iliopoulos, and L. Maiani. “Weak Interactions with Lepton-Hadron Symmetry”. In: *Phys. Rev. D* 2 (7 Oct. 1970), pp. 1285–1292. DOI: 10.1103/PhysRevD.2.1285. URL: <https://link.aps.org/doi/10.1103/PhysRevD.2.1285>.
- [13] Makoto Kobayashi and Toshihide Maskawa. “CP-Violation in the Renormalizable Theory of Weak Interaction”. In: *Progress of Theoretical Physics* 49.2 (Feb. 1973), pp. 652–657. ISSN: 0033-068X. DOI: 10.1143/PTP.49.652. eprint: <https://academic.oup.com/ptp/article-pdf/49/2/652/5257692/49-2-652.pdf>. URL: <https://doi.org/10.1143/PTP.49.652>.
- [14] Lincoln Wolfenstein. “Parametrization of the Kobayashi-Maskawa Matrix”. In: *Phys. Rev. Lett.* 51 (21 Nov. 1983), pp. 1945–1947. DOI: 10.1103/PhysRevLett.51.1945. URL: <https://link.aps.org/doi/10.1103/PhysRevLett.51.1945>.
- [15] C. Jarlskog. “Commutator of the Quark Mass Matrices in the Standard Electroweak Model and a Measure of Maximal CP Nonconservation”. In: *Phys. Rev. Lett.* 55 (10 Sept. 1985), pp. 1039–1042. DOI: 10.1103/PhysRevLett.55.1039. URL: <https://link.aps.org/doi/10.1103/PhysRevLett.55.1039>.
- [16] S. Navas et al. “Review of particle physics”. In: *Phys. Rev. D* 110.3 (2024), p. 030001. DOI: 10.1103/PhysRevD.110.030001.

- [17] A. Höcker et al. “A new approach to a global fit of the CKM matrix”. In: *The European Physical Journal C* 21.2 (June 2001), pp. 225–259. ISSN: 1434-6052. DOI: 10.1007/s100520100729. URL: <http://dx.doi.org/10.1007/s100520100729>. and updates at <http://ckmfitter.in2p3.fr/>.
- [18] Marcella Bona et al. “The 2004 UTfit collaboration report on the status of the unitarity triangle in the standard model”. In: *Journal of High Energy Physics* 2005.07 (July 2005), pp. 028–028. ISSN: 1029-8479. DOI: 10.1088/1126-6708/2005/07/028. URL: <http://dx.doi.org/10.1088/1126-6708/2005/07/028>. and updates at <http://www.utfit.org/UTfit/>.
- [19] Jérôme Charles et al. “New physics in B meson mixing: future sensitivity and limitations”. In: *Phys. Rev. D* 102.5 (2020), p. 056023. DOI: 10.1103/PhysRevD.102.056023. arXiv: 2006.04824 [hep-ph].
- [20] Andrzej J. Buras and Elena Venturini. “Searching for New Physics in Rare K and B Decays without $|V_{cb}|$ and $|V_{ub}|$ Uncertainties”. In: *Acta Phys. Polon. B* 53.6 (Sept. 2021), 6–A1. DOI: 10.5506/APhysPolB.53.6-A1. arXiv: 2109.11032 [hep-ph].
- [21] Maximilian Welch. *Latest results on semileptonic and electroweak penguin decays at Belle II*. <https://moriond.in2p3.fr/QCD/2022/TuesdayMorning/Welsch.pdf>. 2022.
- [22] Y. Aoki et al. “ $B \rightarrow D^* \ell \nu_\ell$ semileptonic form factors from lattice QCD with Möbius domain-wall quarks”. In: *Phys. Rev. D* 109.7 (2024), p. 074503. DOI: 10.1103/PhysRevD.109.074503. arXiv: 2306.05657 [hep-lat].
- [23] Judd Harrison and Christine T. H. Davies. *$B \rightarrow D^*$ vector, axial-vector and tensor form factors for the full q^2 range from lattice QCD*. 2024. arXiv: 2304.03137 [hep-lat]. URL: <https://arxiv.org/abs/2304.03137>.
- [24] A. Bazavov et al. “Semileptonic form factors for $B \rightarrow D^* \ell \nu$ at nonzero recoil from 2 + 1-flavor lattice QCD: Fermilab Lattice and MILC Collaborations”. In: *The European Physical Journal C* 82.12 (Dec. 2022). ISSN: 1434-6052. DOI: 10.1140/epjc/s10052-022-10984-9. URL: <http://dx.doi.org/10.1140/epjc/s10052-022-10984-9>.
- [25] Marzia Bordone, Martin Jung, and Danny van Dyk. “Theory determination of $\bar{B} \rightarrow D^{(*)} \ell^- \bar{\nu}$ form factors at $\mathcal{O}(1/m_c^2)$ ”. In: *The European Physical Journal C* 80.2 (Jan. 2020). ISSN: 1434-6052. DOI: 10.1140/epjc/s10052-020-7616-4. URL: <http://dx.doi.org/10.1140/epjc/s10052-020-7616-4>.

- [26] C. Glenn Boyd, Benjamín Grinstein, and Richard F. Lebed. “Precision corrections to dispersive bounds on form factors”. In: *Physical Review D - Particles, Fields, Gravitation and Cosmology* 56.11 (1997). Cited by: 221; All Open Access, Green Open Access, pp. 6895–6911. DOI: 10.1103/PhysRevD.56.6895. URL: <https://www.scopus.com/inward/record.uri?eid=2-s2.0-0001514365&doi=10.1103%2fPhysRevD.56.6895&partnerID=40&md5=8e88db3d690150ad92499d6c19b9ebdd>.
- [27] Florian U. Bernlochner, Zoltan Ligeti, and Dean J. Robinson. “ $N = 5, 6, 7, 8$: Nested hypothesis tests and truncation dependence of $|V_{cb}|$ ”. In: *Physical Review D* 100.1 (July 2019). ISSN: 2470-0029. DOI: 10.1103/physrevd.100.013005. URL: <http://dx.doi.org/10.1103/PhysRevD.100.013005>.
- [28] Paolo Gambino, Martin Jung, and Stefan Schacht. “The V puzzle: An update”. In: *Physics Letters B* 795 (Aug. 2019), pp. 386–390. ISSN: 0370-2693. DOI: 10.1016/j.physletb.2019.06.039. URL: <http://dx.doi.org/10.1016/j.physletb.2019.06.039>.
- [29] Irinel Caprini, Laurent Lellouch, and Matthias Neubert. “Dispersive bounds on the shape of $B \rightarrow D^* \ell \nu_\ell$ form factors”. In: *Nuclear Physics B* 530.1 (1998), pp. 153–181. ISSN: 0550-3213. DOI: [https://doi.org/10.1016/S0550-3213\(98\)00350-2](https://doi.org/10.1016/S0550-3213(98)00350-2). URL: <https://www.sciencedirect.com/science/article/pii/S0550321398003502>.
- [30] I. Adachi et al. “Determination of $|V_{cb}|$ using $B^0 \rightarrow D^{*+} \ell^- \nu_\ell$ decays with Belle II”. In: *Phys. Rev. D* 108.9 (2023), p. 092013. DOI: 10.1103/PhysRevD.108.092013. arXiv: 2310.01170 [hep-ex].
- [31] A. Sirlin. “Large m_W, m_Z behaviour of the $O(\alpha)$ corrections to semileptonic processes mediated by W ”. In: *Nuclear Physics B* 196.1 (1982), pp. 83–92. ISSN: 0550-3213. DOI: [https://doi.org/10.1016/0550-3213\(82\)90303-0](https://doi.org/10.1016/0550-3213(82)90303-0). URL: <https://www.sciencedirect.com/science/article/pii/0550321382903030>.
- [32] Yasmine Sara Amhis et al. “Averages of b-hadron, c-hadron, and τ -lepton properties as of 2021”. In: *Phys. Rev. D* 107.5 (2023), p. 052008. DOI: 10.1103/PhysRevD.107.052008. arXiv: 2206.07501 [hep-ex].
- [33] E. Waheed et al. “Measurement of the CKM matrix element $|V_{cb}|$ from $B^0 \rightarrow D^{*-} \ell^+ \nu_\ell$ at Belle”. In: *Phys. Rev. D* 100.5 (2019). [Erratum: Phys.Rev.D 103, 079901 (2021)], p. 052007. DOI: 10.1103/PhysRevD.100.052007. arXiv: 1809.03290 [hep-ex].

- [34] F. Abudinén et al. “Measurement of the semileptonic $\bar{B}^0 \rightarrow D^{*+}\ell^-\nu_\ell$ branching fraction with fully reconstructed B meson decays and 34.6 fb^{-1} of Belle II data”. In: (Aug. 2020). arXiv: 2008.10299 [hep-ex].
- [35] D. Buskulic et al. “Measurements of $|V_{cb}|$, form factors and branching fractions in the decays $B^0 \rightarrow D^{*+}\ell^-\nu_\ell ll$ and $B^0 \rightarrow D^+\ell^-\nu_\ell$ ”. In: *Physics Letters B* 395.3 (1997), pp. 373–387. ISSN: 0370-2693. DOI: [https://doi.org/10.1016/S0370-2693\(97\)00071-3](https://doi.org/10.1016/S0370-2693(97)00071-3). URL: <https://www.sciencedirect.com/science/article/pii/S0370269397000713>.
- [36] G. Abbiendi et al. “Measurement of $|V_{cb}|$ using $B^0 \rightarrow D^{*+}\ell^-\nu_\ell$ decays”. In: *Physics Letters B* 482.1–3 (June 2000), pp. 15–30. ISSN: 0370-2693. DOI: 10.1016/S0370-2693(00)00457-3. URL: [http://dx.doi.org/10.1016/S0370-2693\(00\)00457-3](http://dx.doi.org/10.1016/S0370-2693(00)00457-3).
- [37] P. Abreu et al. “Measurement of V_{cb} from the decay process $B^0 \rightarrow D^{*+}\ell^-\bar{\nu}$ ”. In: *Physics Letters B* 510.1–4 (June 2001), pp. 55–74. ISSN: 0370-2693. DOI: 10.1016/S0370-2693(01)00569-X. URL: [http://dx.doi.org/10.1016/S0370-2693\(01\)00569-X](http://dx.doi.org/10.1016/S0370-2693(01)00569-X).
- [38] “Measurement of $|V_{cb}|$ using the semileptonic decay $\bar{B}_d^0 \rightarrow D^*\ell^-\bar{\nu}_\ell$ ”. In: *The European Physical Journal C* 33.2 (Mar. 2004), pp. 213–232. ISSN: 1434-6052. DOI: 10.1140/epjc/s2004-01598-6. URL: <http://dx.doi.org/10.1140/epjc/s2004-01598-6>.
- [39] N. E. Adam et al. “Determination of the $\bar{B} \rightarrow D^*\ell\bar{\nu}_\ell$ Decay Width and $|V_{cb}|$ ”. In: *Physical Review D* 67.3 (Feb. 2003). ISSN: 1089-4918. DOI: 10.1103/PhysRevD.67.032001. URL: <http://dx.doi.org/10.1103/PhysRevD.67.032001>.
- [40] Bernard Aubert et al. “Determination of the form-factors for the decay $B^0 \rightarrow D^{*-}\ell^+\nu_\ell$ and of the CKM matrix element $|V_{cb}|$ ”. In: *Phys. Rev. D* 77 (2008), p. 032002. DOI: 10.1103/PhysRevD.77.032002. arXiv: 0705.4008 [hep-ex].
- [41] B. Aubert et al. “Measurement of the Branching Fractions of Exclusive $\bar{B} \rightarrow D^{(*)}(\pi)l^-\bar{\nu}_l$ Decays in Events with a Fully Reconstructed B Meson”. In: *Phys. Rev. Lett.* 100 (15 Apr. 2008), p. 151802. DOI: 10.1103/PhysRevLett.100.151802. URL: <https://link.aps.org/doi/10.1103/PhysRevLett.100.151802>.
- [42] F. Abudinén et al. “Studies of the semileptonic $\bar{B}^0 \rightarrow D^{*+}\ell^-\bar{\nu}_\ell$ and $B^- \rightarrow D^0\ell^-\bar{\nu}_\ell$ decay processes with 34.6 fb^{-1} of Belle II data”. In: (Aug. 2020). arXiv: 2008.07198 [hep-ex].

- [43] Bernard Aubert et al. “Measurement of the Decay $B^- \rightarrow D^{*0}e^- \bar{\nu}(e)$ ”. In: *Phys. Rev. Lett.* 100 (2008), p. 231803. DOI: 10.1103/PhysRevLett.100.231803. arXiv: 0712.3493 [hep-ex].
- [44] Bernard Aubert et al. “Measurements of the Semileptonic Decays $\bar{B} \rightarrow D\ell\bar{\nu}$ and $\bar{B} \rightarrow D\ell\bar{\nu}$ Using a Global Fit to $DX\ell\bar{\nu}$ Final States”. In: *Phys. Rev. D* 79 (2009), p. 012002. DOI: 10.1103/PhysRevD.79.012002. arXiv: 0809.0828 [hep-ex].
- [45] Y. Aoki et al. “FLAG Review 2021”. In: *The European Physical Journal C* 82.10 (Oct. 2022). ISSN: 1434-6052. DOI: 10.1140/epjc/s10052-022-10536-1. URL: <http://dx.doi.org/10.1140/epjc/s10052-022-10536-1>.
- [46] Jon A. Bailey et al. “Update of $|V_{cb}|$ from the $\bar{B} \rightarrow D^*\ell\bar{\nu}$ form factor at zero recoil with three-flavor lattice QCD”. In: *Phys. Rev. D* 89 (11 June 2014), p. 114504. DOI: 10.1103/PhysRevD.89.114504. URL: <https://link.aps.org/doi/10.1103/PhysRevD.89.114504>.
- [47] Dante Bigi, Paolo Gambino, and Stefan Schacht. “A fresh look at the determination of $|V_{cb}|$ from $B \rightarrow D^*\ell\nu_\ell$ ”. In: *Physics Letters B* 769 (2017), pp. 441–445. ISSN: 0370-2693. DOI: <https://doi.org/10.1016/j.physletb.2017.04.022>. URL: <https://www.sciencedirect.com/science/article/pii/S0370269317302964>.
- [48] Benjamín Grinstein and Andrew Kobach. “Model-independent extraction of $|V_{cb}|$ from $\bar{B} \rightarrow D^*\ell\bar{\nu}_\ell$ ”. In: *Physics Letters B* 771 (2017), pp. 359–364. ISSN: 0370-2693. DOI: <https://doi.org/10.1016/j.physletb.2017.05.078>. URL: <https://www.sciencedirect.com/science/article/pii/S0370269317304410>.
- [49] A. Abdesselam et al. “Precise determination of the CKM matrix element $|V_{cb}|$ with $\bar{B}^0 \rightarrow D^{*+}\ell^- \bar{\nu}_\ell$ decays with hadronic tagging at Belle”. In: (Feb. 2017). arXiv: 1702.01521 [hep-ex].
- [50] M. T. Prim et al. “Measurement of differential distributions of $B \rightarrow D^*\ell\nu_\ell$ and implications on $|V_{cb}|$ ”. In: *Phys. Rev. D* 108.1 (2023), p. 012002. DOI: 10.1103/PhysRevD.108.012002. arXiv: 2301.07529 [hep-ex].
- [51] Belle Collaboration et al. *Measurement of Angular Coefficients of $\bar{B} \rightarrow D^*\ell\bar{\nu}_\ell$: Implications for $|V_{cb}|$ and Tests of Lepton Flavor Universality*. 2023. arXiv: 2310.20286 [hep-ex]. URL: <https://arxiv.org/abs/2310.20286>.

- [52] M. Mantovano. *Simultaneous analysis of $B \rightarrow D^* \ell \nu_\ell$ and $B \rightarrow D \ell \nu_\ell$ to improve the determination of $|V_{cb}|$* . <https://indico.cern.ch/event/1345421/contributions/6040065/>.
- [53] Yuki Yoshi Ohnishi et al. “Accelerator design at SuperKEKB”. In: *Prog. Theo. Exp. Phys.* (2013), 03A011. DOI: 10.1093/ptep/pts083.
- [54] P. Oddone. “Detector Considerations”. In: *D. H. Stork, proceedings of Workshop on Conceptual Design of a Test Linear Collider: Possibilities for a BB Factory* (1987), p. 423.
- [55] Paolo Raimondi et al. “Beam-beam issues for colliding schemes with large Piwinski angle and crabbed waist”. In: (2007). arXiv: physics/0702033.
- [56] T. Abe, I. Adachi, et al. *Belle II Technical Design Report*. 2010. DOI: 10.48550/ARXIV.1011.0352. URL: <https://arxiv.org/abs/1011.0352>.
- [57] C. Marinas. “The Belle II pixel detector: High precision with low material”. In: *Nucl. Instrum. Meth.* A731 (2013), p. 31. DOI: 10.1016/j.nima.2013.03.025.
- [58] K. Adamczyk et al. “The Belle II silicon vertex detector assembly and mechanics”. In: *Nucl. Instrum. Meth.* A845 (2017), p. 38. DOI: 10.1016/j.nima.2016.03.100.
- [59] N. Taniguchi. “Central Drift Chamber for Belle II”. In: *JINST* 12 (2017), p. C06014. DOI: 10.1088/1748-0221/12/06/C06014.
- [60] Valerio Bertacchi et al. “Track finding at Belle II”. In: *Computer Physics Communications* 259 (Feb. 2021), p. 107610. DOI: 10.1016/j.cpc.2020.107610. URL: <https://doi.org/10.1016%2Fj.cpc.2020.107610>.
- [61] Belle II Collaboration and B2TiP theory Community. *The Belle II Physics Book*. 1st. Prog. Theor. Exp. Phys., 2018.
- [62] A. Abashian et al. “The K_L/μ detector subsystem for the BELLE experiment at the KEK B factory”. In: *Nucl. Instrum. Meth.* A449 (2000), p. 112. DOI: 10.1016/S0168-9002(99)01383-2.
- [63] Francesco Forti. “Snowmass Whitepaper: The Belle II Detector Upgrade Program”. In: *2022 Snowmass Summer Study*. Mar. 2022. arXiv: 2203.11349 [hep-ex].
- [64] Belle II collaboration. *Belle II Luminosity*. 2024. URL: <https://www.belle2.org/research/luminosity/>.

- [65] T. Kuhr et al. “The Belle II Core Software”. In: *Computing and Software for Big Science* 3.1 (Nov. 2018). DOI: 10.1007/s41781-018-0017-9. URL: <https://doi.org/10.1007/2Fs41781-018-0017-9>.
- [66] David J. Lange. “The EvtGen particle decay simulation package”. In: *Nuclear Instruments and Methods in Physics Research Section A: Accelerators, Spectrometers, Detectors and Associated Equipment* 462.1 (2001). BEAUTY2000, Proceedings of the 7th Int. Conf. on B-Physics at Hadron Machines, pp. 152–155. ISSN: 0168-9002. DOI: [https://doi.org/10.1016/S0168-9002\(01\)00089-4](https://doi.org/10.1016/S0168-9002(01)00089-4). URL: <https://www.sciencedirect.com/science/article/pii/S0168900201000894>.
- [67] Torbjörn Sjöstrand et al. “An introduction to PYTHIA 8.2”. In: *Computer Physics Communications* 191 (2015), pp. 159–177. ISSN: 0010-4655. DOI: <https://doi.org/10.1016/j.cpc.2015.01.024>. URL: <https://www.sciencedirect.com/science/article/pii/S0010465515000442>.
- [68] S. Jadach et al. “The precision Monte Carlo event generator for two-fermion final states in collisions”. In: *Computer Physics Communications* 130.3 (Aug. 2000), pp. 260–325. DOI: 10.1016/s0010-4655(00)00048-5. URL: <https://doi.org/10.1016%2Fs0010-4655%2800%2900048-5>.
- [69] S. Jadach et al. “Coherent exclusive exponentiation for precision Monte Carlo calculations”. In: *Phys. Rev. D* 63 (11 May 2001), p. 113009. DOI: 10.1103/PhysRevD.63.113009. URL: <https://link.aps.org/doi/10.1103/PhysRevD.63.113009>.
- [70] S. Jadach et al. “TAUOLA - a library of Monte Carlo programs to simulate decays of polarized tau leptons”. In: *Computer Physics Communications* 64.2 (1991), pp. 275–299. ISSN: 0010-4655. DOI: [https://doi.org/10.1016/0010-4655\(91\)90038-M](https://doi.org/10.1016/0010-4655(91)90038-M). URL: <https://www.sciencedirect.com/science/article/pii/001046559190038M>.
- [71] N. Davidson et al. “Universal interface of TAUOLA: Technical and physics documentation”. In: *Computer Physics Communications* 183.3 (2012), pp. 821–843. ISSN: 0010-4655. DOI: <https://doi.org/10.1016/j.cpc.2011.12.009>. URL: <https://www.sciencedirect.com/science/article/pii/S0010465511003973>.

- [72] S. Agostinelli et al. “Geant4 - a simulation toolkit”. In: *Nuclear Instruments and Methods in Physics Research Section A: Accelerators, Spectrometers, Detectors and Associated Equipment* 506.3 (2003), pp. 250–303. ISSN: 0168-9002. DOI: [https://doi.org/10.1016/S0168-9002\(03\)01368-8](https://doi.org/10.1016/S0168-9002(03)01368-8). URL: <https://www.sciencedirect.com/science/article/pii/S0168900203013688>.
- [73] Geoffrey Fox and Stephen Wolfram. “Observables for the Analysis of Event Shapes in e^+e^- Annihilation and Other Processes”. In: *Physical Review Letters* 41 (Dec. 1978), pp. 1581–1585. DOI: 10.1103/PhysRevLett.41.1581.
- [74] Daniel Ferlewicz, Phillip Urquijo, and Eiasa Waheed. “Revisiting fits to $B^0 \rightarrow D^{*-} \ell^+ \nu_\ell$ to measure $|V_{cb}|$ with novel methods and preliminary LQCD data at nonzero recoil”. In: *Phys. Rev. D* 103.7 (2021), p. 073005. DOI: 10.1103/PhysRevD.103.073005. arXiv: 2008.09341 [hep-ph].

Appendix A

Form Factor parameterizations

The BGL parameterization, already presented in Sec. 2.1, is reported in terms of helicity amplitudes. They can be expressed in series of z :

$$g(z) = \frac{1}{P_{1^-}(z) \phi_g(z)} \sum_{n=0}^{\infty} a_n z^n, \quad (\text{A.1})$$

$$f(z) = \frac{1}{P_{1^+}(z) \phi_f(z)} \sum_{n=0}^{\infty} b_n z^n, \quad (\text{A.2})$$

$$\mathcal{F}_1(z) = \frac{1}{P_{1^+}(z) \phi_{\mathcal{F}_1}(z)} \sum_{n=0}^{\infty} c_n z^n, \quad (\text{A.3})$$

with $z = (\sqrt{w+1} - \sqrt{2}) / (\sqrt{w+1} + \sqrt{2})$ the conformal variable. The functions ϕ_{f,g,\mathcal{F}_1} are called outer functions, and the Blaschke factors $P_{1^\pm}(z)$ are functions that describe the resonance $J^P = 1^\pm$:

$$P_{1^\pm}(z) = C_{1^\pm} \sum_{k=1}^{poles} \frac{z - z_k}{1 - z z_k}, \quad (\text{A.4})$$

with

$$z_k = \frac{\sqrt{t_+ - m_k^2} - \sqrt{t_+ - t_-}}{\sqrt{t_+ - m_k^2} + \sqrt{t_+ - t_-}}, \quad (\text{A.5})$$

where $t_\pm = (m_B \pm m_{D^*})^2$, m_k indicates the pole mass of the k -th excited B_c^* state and C_1^\pm is a coefficient. The assumed values of these parameters are in Table A.1. The outer functions are

J^P	Pole mass [GeV/ c^2]				$\tilde{\chi}_{J^P}(0)$	C_{J^P}
1^-	6.337	6.899	7.012	7.280	5.131	1
1^+	6.730	6.736	7.135	7.142	3.894	1

Table A.1: Pole masses assumed in this work. The values are taken from [74].

defined as follows:

$$\phi_g(z) = 16r^2 \sqrt{\frac{n_I}{3\pi\tilde{\chi}_{1^-}(0)}} \frac{(1+z)^2}{\sqrt{1-z}[(1+r)(1-z) + 2\sqrt{r}(1+z)]^4}, \quad (\text{A.6})$$

$$\phi_f(z) = \frac{4r}{m_B^2} \sqrt{\frac{n_I}{3\pi\tilde{\chi}_{1^+}(0)}} \frac{(1+z)\sqrt{(1-z)^3}}{[(1+r)(1-z) + 2\sqrt{r}(1+z)]^4}, \quad (\text{A.7})$$

$$\phi_{\mathcal{F}_1}(z) = \frac{4r}{m_B^3} \sqrt{\frac{n_I}{6\pi\tilde{\chi}_{1^+}(0)}} \frac{(1+z)\sqrt{(1-z)^5}}{[(1+r)(1-z) + 2\sqrt{r}(1+z)]^5}, \quad (\text{A.8})$$

where $r = m_{D^*}/m_B$, n_I is the effective number of light quarks, which is 2.6, $\tilde{\chi}_{1^\pm}(0)$ are coefficients of outer functions, also reported in Table A.1. The coefficients in the series of Eqs A.1-A.3 are bounded by the unitarity constraints:

$$\sum_{n=0}^{\infty} a_n^2 \leq 1, \quad \sum_{n=0}^{\infty} (b_n^2 + c_n^2) \leq 1. \quad (\text{A.9})$$

These coefficients are the free parameters of the BGL model; depending on the desired truncation, there can be an arbitrary number of them. Two initial values of the series can be fixed from lattice calculation: the coefficient b_0 is related to $h_{A_1}(1)$:

$$b_0 = 2\sqrt{m_B m_{D^*}} P_{1^+}(0) \phi_f(0) h_{A_1}(1), \quad (\text{A.10})$$

and it is related to the coefficient c_0 :

$$c_0 = (m_B - m_{D^*}) \frac{\phi_{\mathcal{F}_1}(0)}{\phi_f(0)} b_0. \quad (\text{A.11})$$

The CLN parametrization functions can be connected with BGL functions

$$h_{A_1}(w) = \frac{f(w)}{\sqrt{m_B m_{D^*}}(1+w)}, \quad (\text{A.12})$$

$$R_1(w) = (w+1)m_B m_{D^*} \frac{g(w)}{f(w)}, \quad (\text{A.13})$$

$$R_2(w) = \frac{w-r}{w-1} - \frac{\mathcal{F}_1(w)}{m_B(w-1)f(w)}, \quad (\text{A.14})$$

and can be expressed in terms of three form factors, $h_{A_1}(w)$, $R_1(w)$, $R_2(w)$:

$$H_{\pm,0} = 2 \frac{\sqrt{m_B m_{D^*}}}{m_B + m_{D^*}} (1-r^2)(w+1)(w^2-1)^{1/4} h_{A_1}(w) \tilde{H}_{\pm,0}(w) \quad (\text{A.15})$$

and

$$\tilde{H}_{\pm}(w) = \frac{\sqrt{1-2wr+r^2}}{1-r} \left[1 \mp \sqrt{\frac{w-1}{w+1}} R_1(w) \right], \quad (\text{A.16})$$

$$\tilde{H}_0(w) = 1 + \frac{(w-1)(1-R_2(w))}{1-r}. \quad (\text{A.17})$$

We can rewrite $h_{A_1}(w)$ in powers of the conformal variable z and the two remaining form factors in powers of $(w-1)$:

$$h_{A_1}(z) = h_{A_1}(1)[1 - 8\rho^2 z + (53\rho^2 - 15)z^2 - (231\rho^2 - 91)z^3] \quad (\text{A.18})$$

$$R_1(w) = R_1(1) - 0.12(w-1) + 0.05(w-1)^2 \quad (\text{A.19})$$

$$R_2(w) = R_2(1) - 0.11(w-1) - 0.06(w-1)^2 \quad (\text{A.20})$$

In this way, the three form factors depend only on four parameters: $h_{A_1}(1)$, $R_1(1)$, $R_2(1)$ and ρ .

Appendix B

Data-simulation comparison

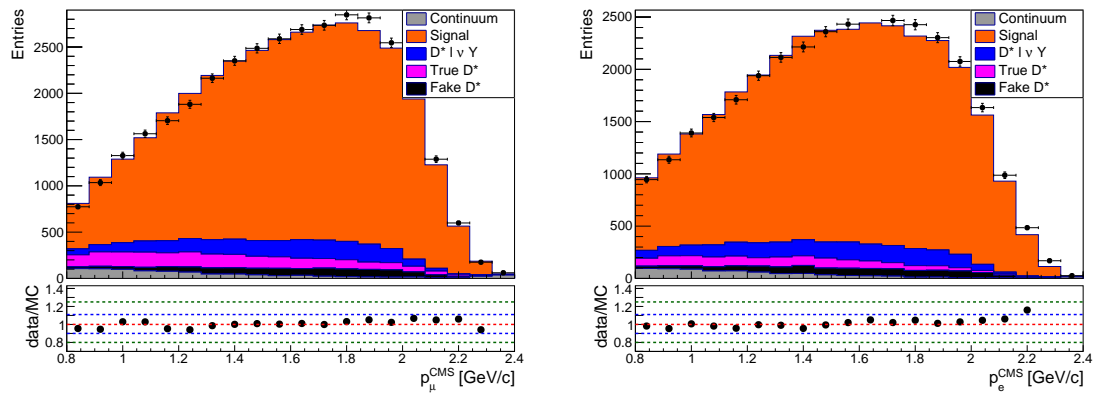


Figure B.1: Data-simulation comparison for distributions of the muon channel (left) and electron channel (right). The graphs show the distributions of p_{ℓ}^{CMS} . Ratio of data and MC distributions is also shown in the bottom part of each plot.

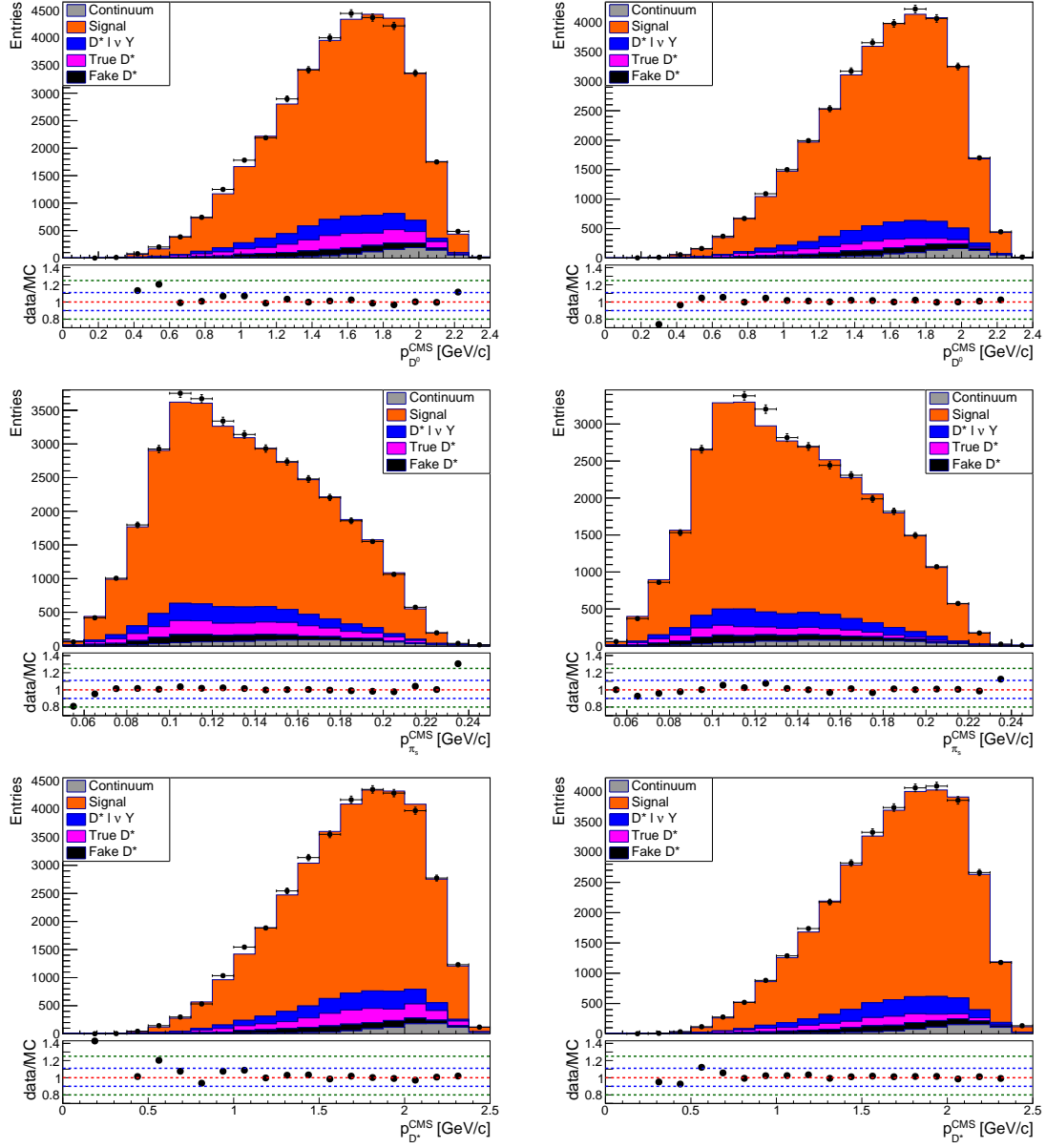


Figure B.2: Data-simulation comparison for distributions of the muon channel (left) and electron channel (right). The graphs show the distributions of $p_{D^*}^{\text{CMS}}$ (top row), $p_{\pi_s}^{\text{CMS}}$ (middle row) and $p_{D^*}^{\text{CMS}}$ (bottom row). Ratio of data and MC distributions is also shown in the bottom part of each plot.

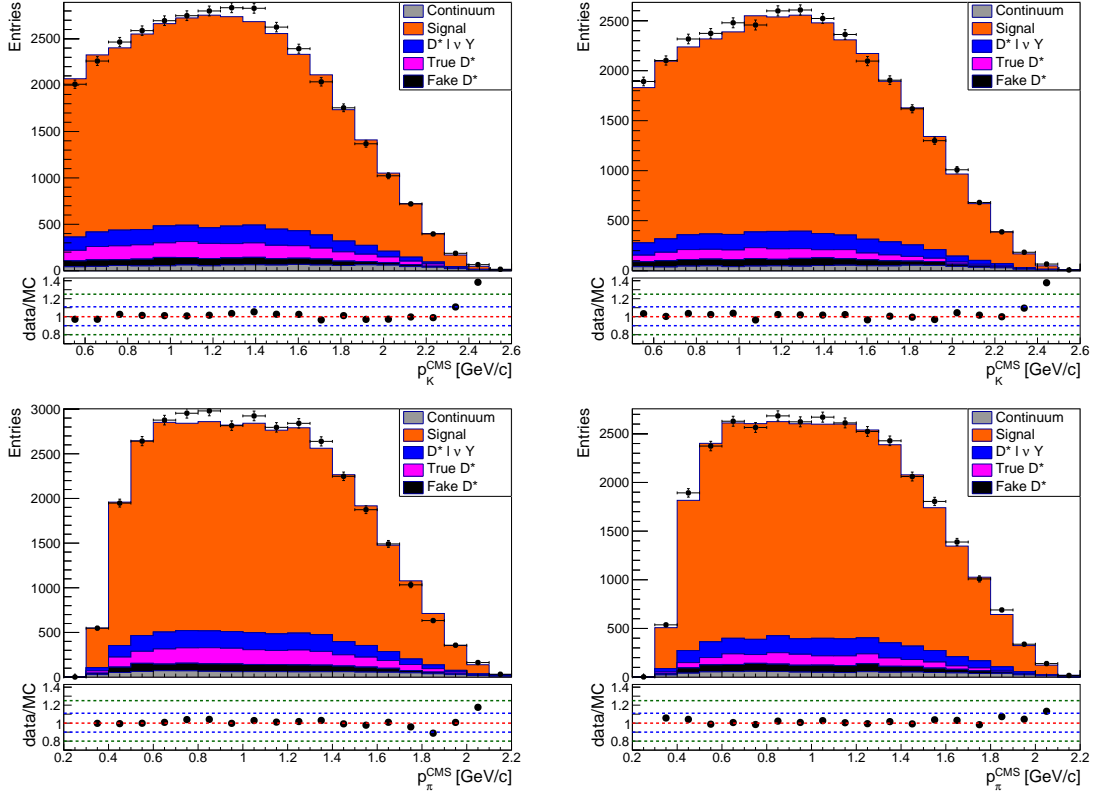


Figure B.3: Data-simulation comparison for distributions of the muon channel (left) and electron channel (right). The graphs show the distributions of p_K^{CMS} (top row) and p_π^{CMS} (bottom row). Ratio of data and MC distributions is also shown in the bottom part of each plot.

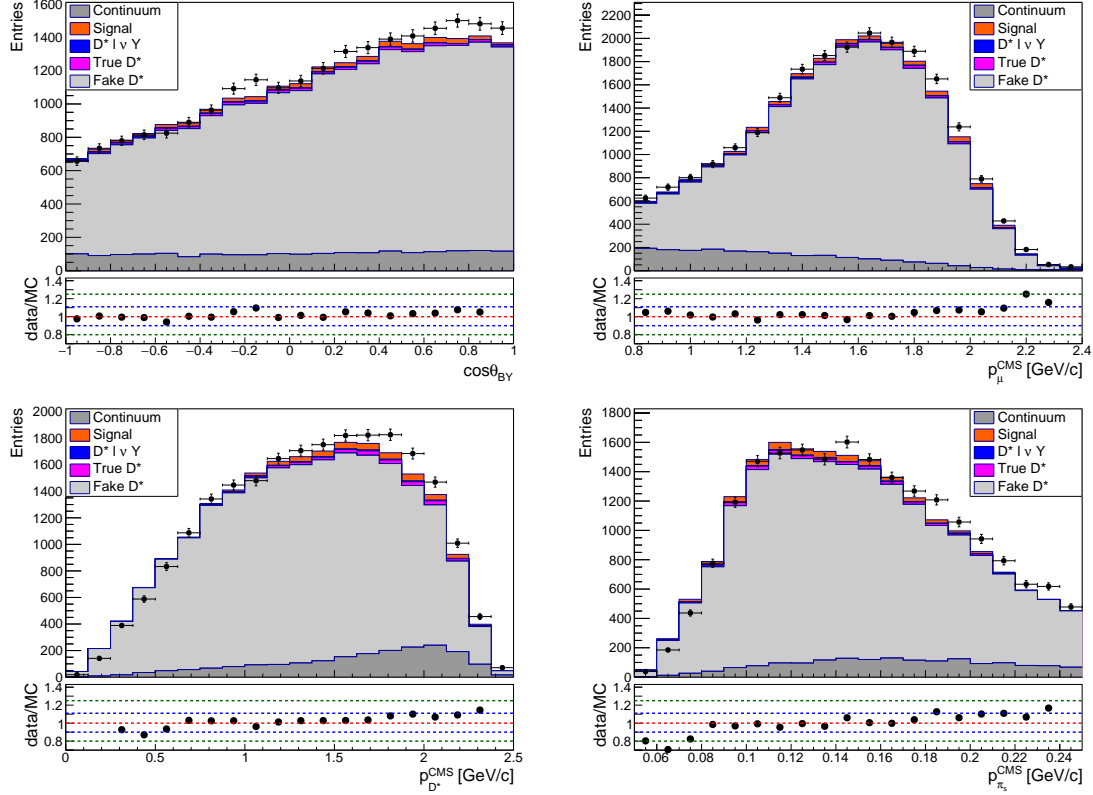


Figure B.4: Distributions of variables for events in the sidebands for the muon channel. The graphs show the distributions of $\cos \theta_{BY}$ (top-left), p_ℓ^{CMS} (top-right), $p_{D^*}^{\text{CMS}}$ (bottom-left) and $p_{\pi_s}^{\text{CMS}}$ (bottom-right). Ratio of data and MC distributions is also shown in the bottom part of each plot.

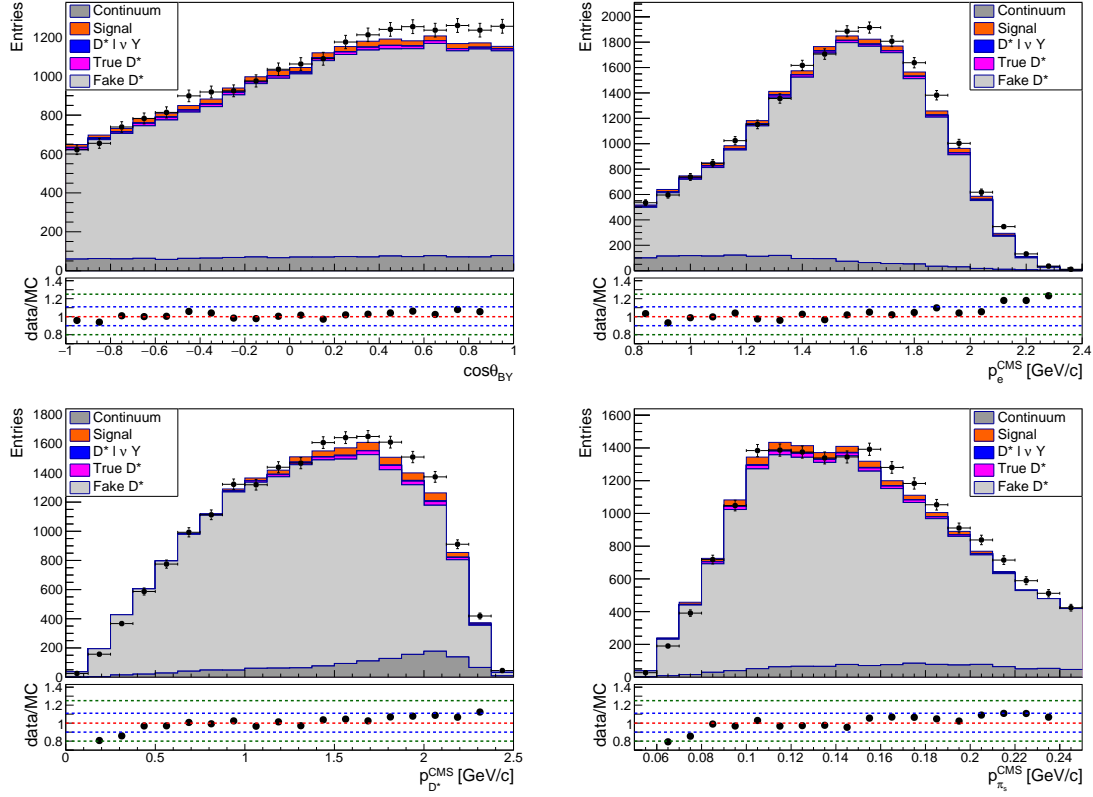


Figure B.5: Distributions of variables for events in the sidebands for the electron channel. The graphs show the distributions of $\cos\theta_{BY}$ (top-left), p_ℓ^{CMS} (top-right), $p_{D^*}^{\text{CMS}}$ (bottom-left) and $p_{\pi_s}^{\text{CMS}}$ (bottom-right). Ratio of data and MC distributions is also shown in the bottom part of each plot.

Appendix C

Fit of sample composition: pull distributions

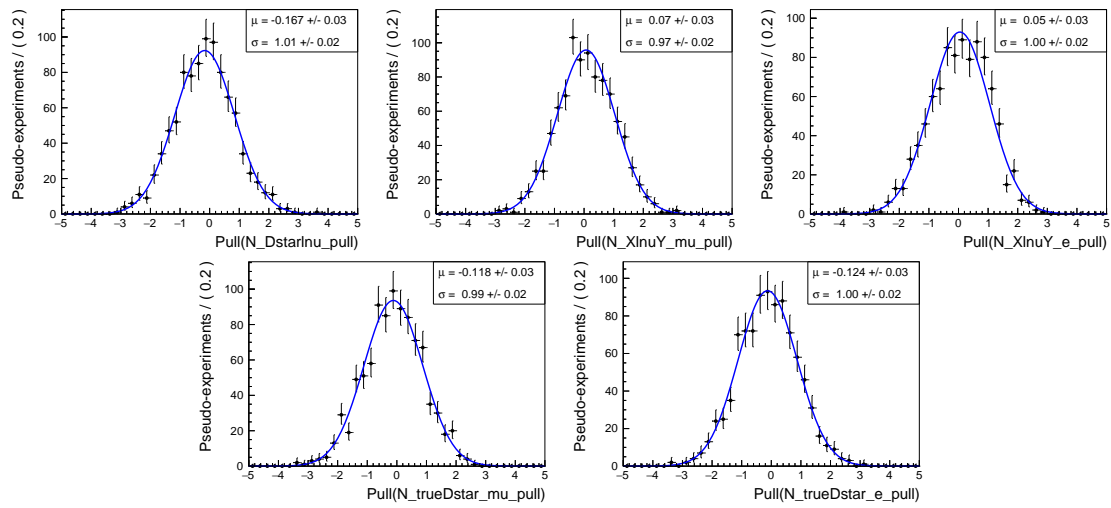


Figure C.1: Pull distributions of the five free parameters of the fit for the 360 fb^{-1} integrated luminosity pseudo-experiments.

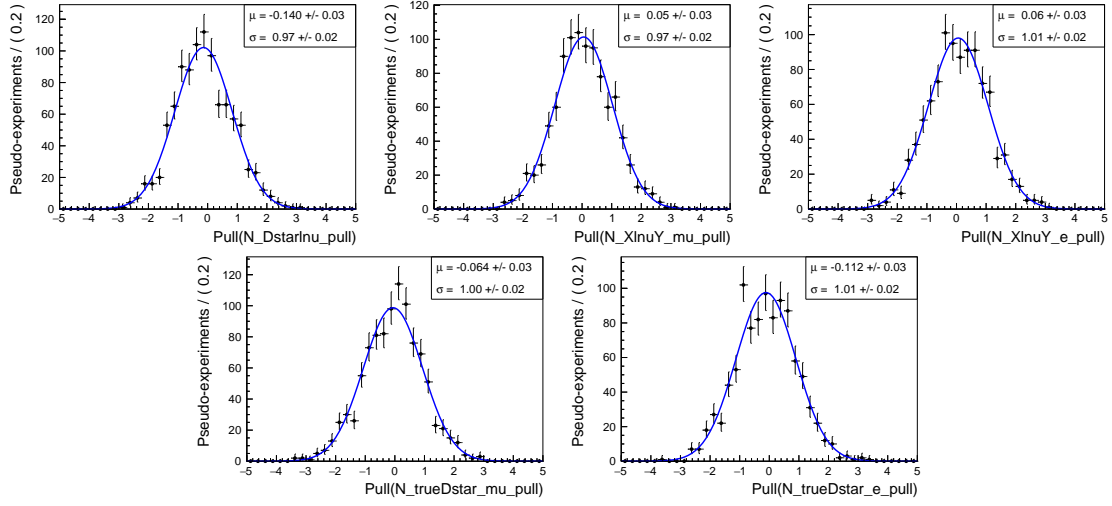


Figure C.2: Pull distributions of the five free parameters of the fit for the 700 fb^{-1} integrated luminosity pseudo-experiments.

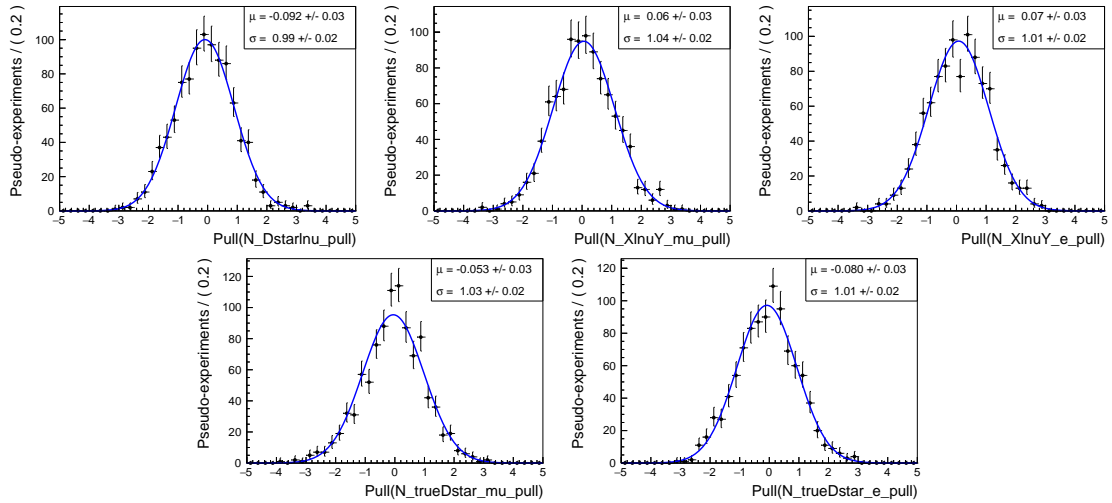


Figure C.3: Pull distributions of the five free parameters of the fit for the 3000 fb^{-1} integrated luminosity pseudo-experiments.

Appendix D

Model-independent fit: pull distributions

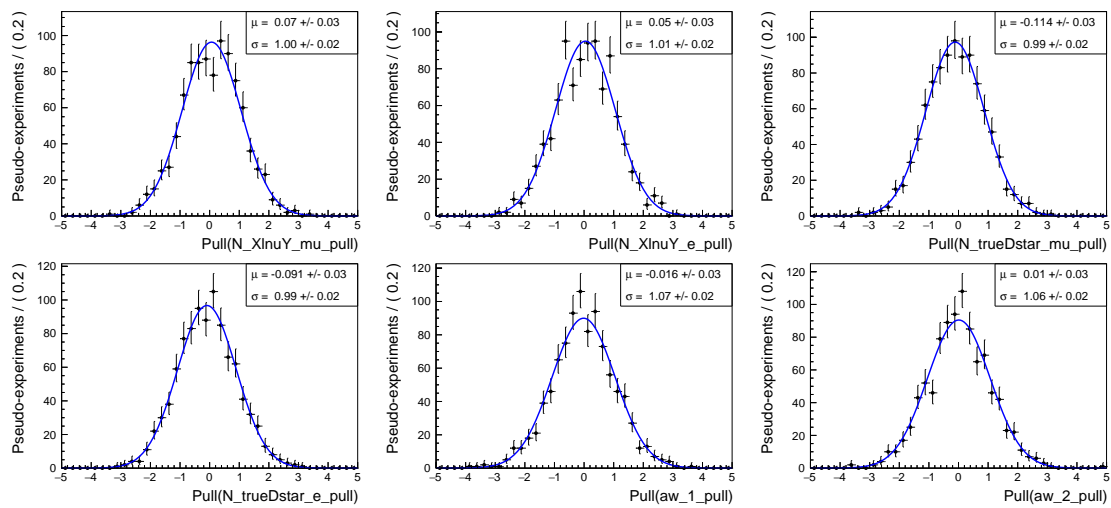


Figure D.1: Pull distributions of the free parameters of the model-independent fit for configuration A.

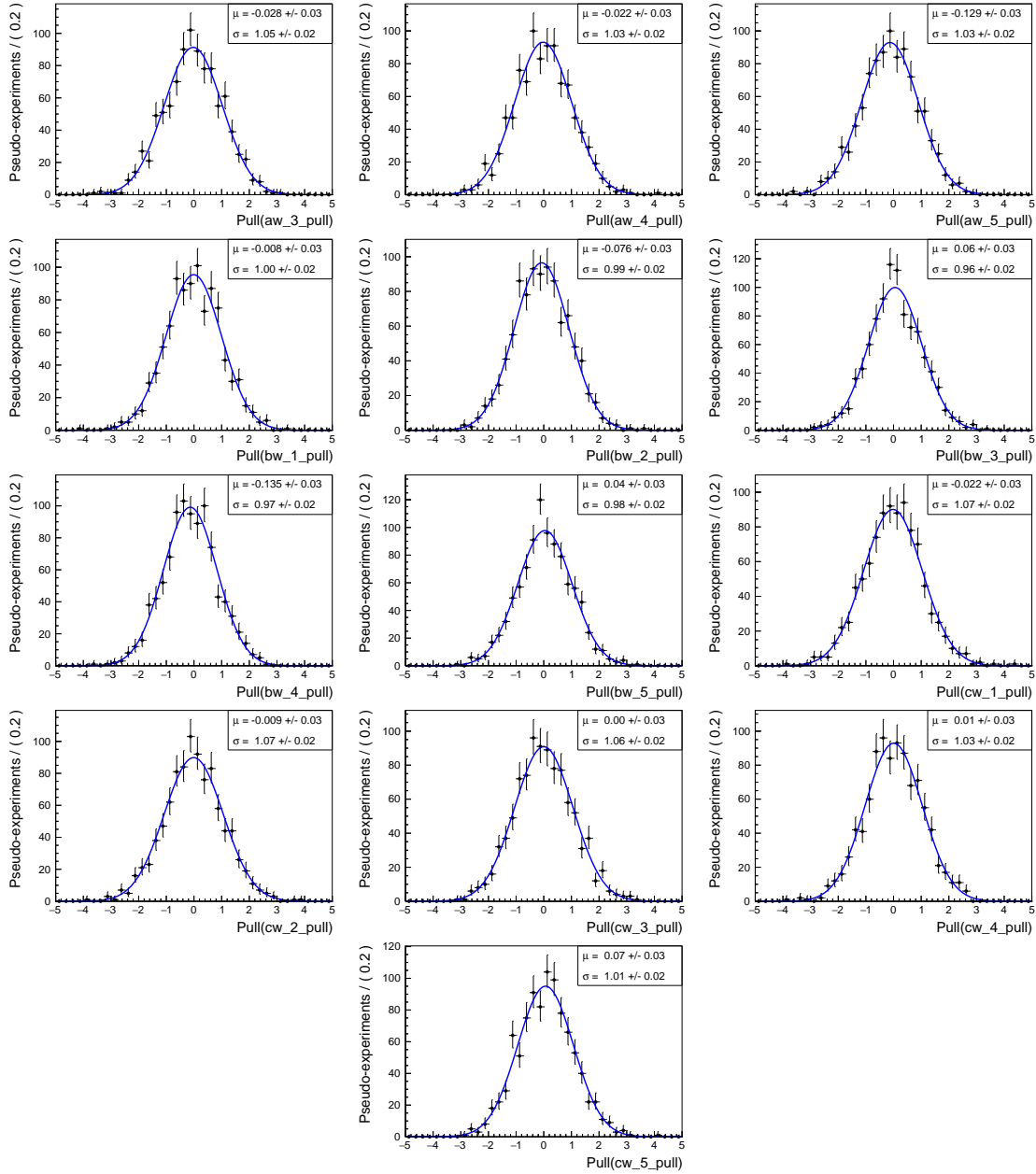


Figure D.2: Pull distributions of the free parameters of the model-independent fit for configuration A.

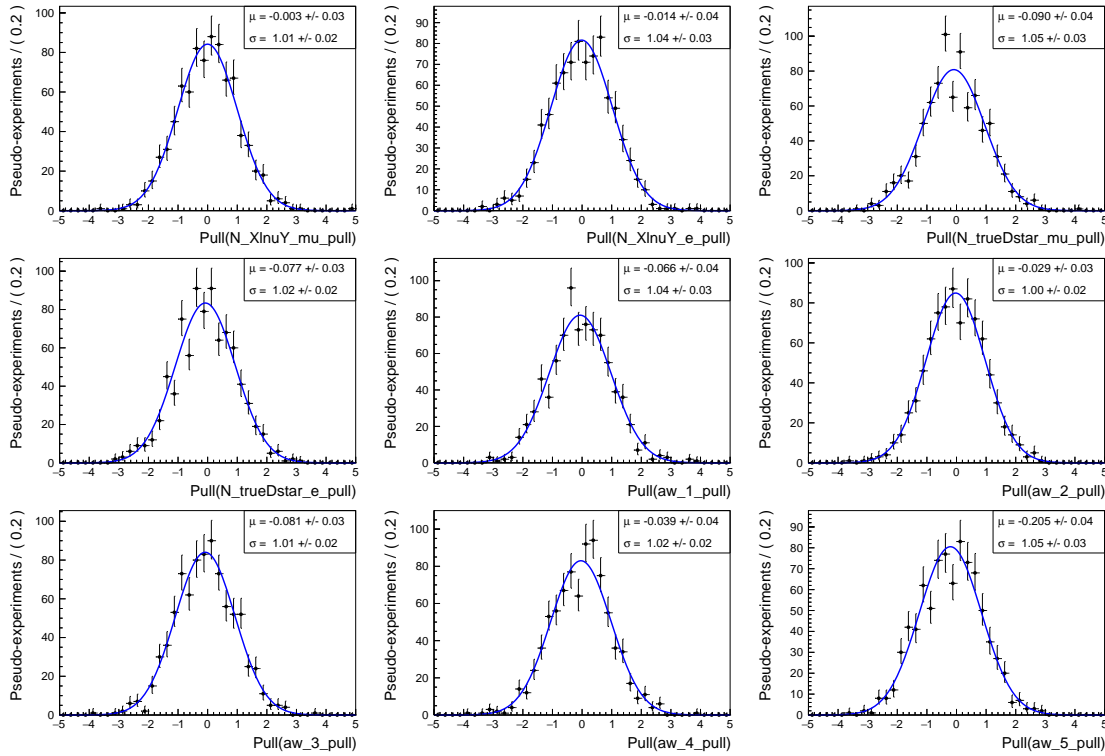


Figure D.3: Pull distributions of the free parameters of the model-independent fit for configuration B.

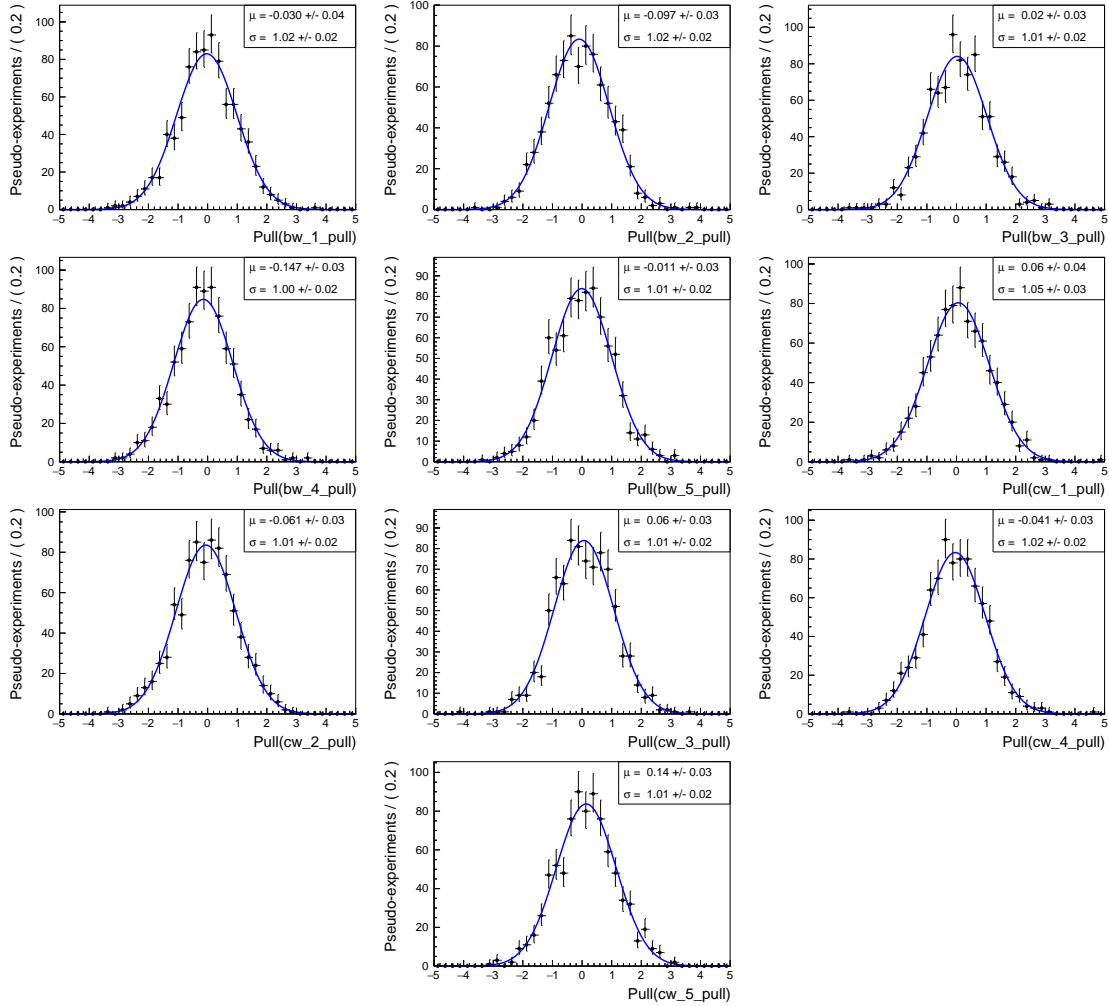


Figure D.4: Pull distributions of the free parameters of the model-independent fit for configuration B.

Appendix E

A-posteriori fit: pull distributions

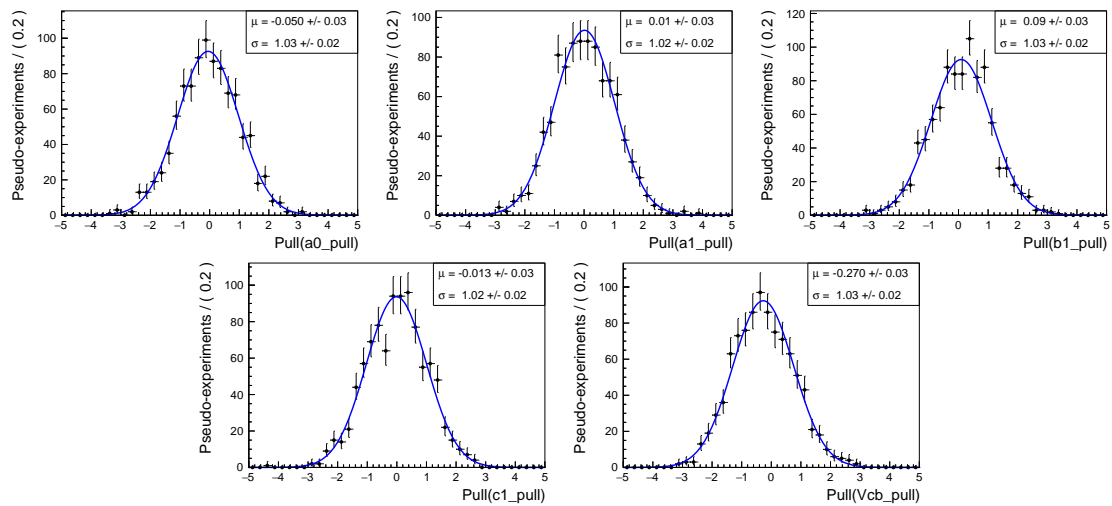


Figure E.1: Pull distributions of the free parameters of the *a-posteriori* fit for configuration A.

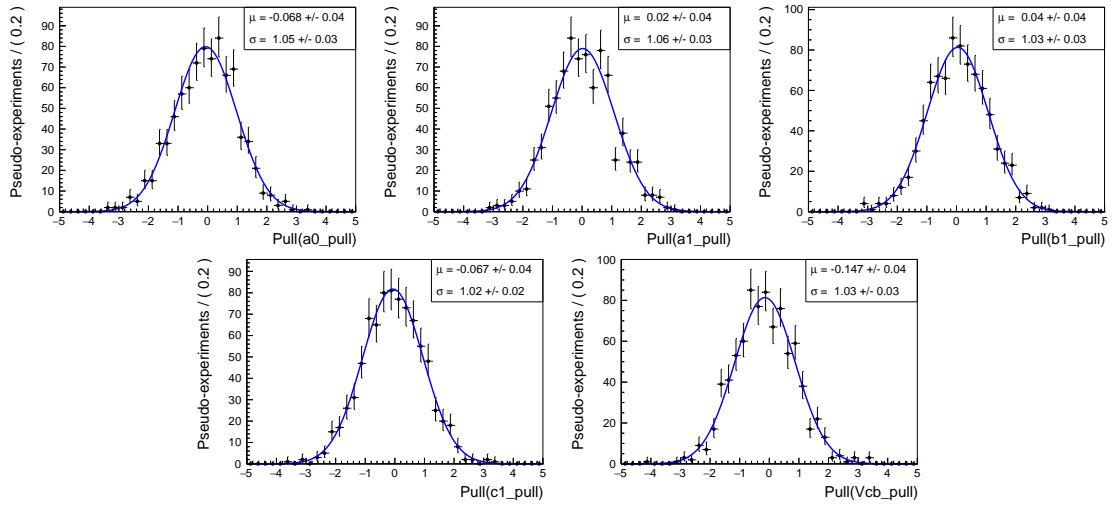


Figure E.2: Pull distributions of the free parameters of the *a-posteriori* fit for configuration B.